NOTICE

The quality of this microform is heavily dependent upon the quality of the original thesis submitted for microfilming. Every effort has been made to ensure the highest quality of reproduction possible.

If pages are missing, contact the university which granted the degree.

Some pages may have indistinct print especially if the original pages were typed with a poor typewriter ribbon or if the university sent us an inferior photocopy.

Reproduction in full or in part of this microform is governed by the Canadian Copyright Act, R.S.C. 1970, c. C-30, and subsequent amendments.

AVIS

La qualité de cette microforme dépend grandement de la qualité de la thèse soumise au microfilmage. Nous avons tout fait pour assurer une qualité supérieure de reproduction.

S'il manque des pages, veuillez communiquer avec l'université qui a conféré le grade.

La qualité d'impression de certaines pages peut laisser à désirer, surtout si les pages originales ont été dactylographiées à l'aide d'un ruban usé ou si l'université nous a fait parvenir une photocopie de qualité inférieure.

La reproduction, même partielle, de cette microforme est soumise à la Loi canadienne sur le droit d'auteur, SRC 1970, c. C-30, et ses amendements subséquents.

FLUX LINE INTERACTIONS IN CONVENTIONAL AND HIGH T_C SUPERCONDUCTORS

Thesis submitted to the School of Graduate Studies and Research
of the University of Ottawa in partial fulfillment
of the requirements for the degree
of Master of Science in Physics

Richard Lalonde
Department of Physics, University of Ottawa
Ottawa, Ontario, Canada

August 31, 1990

ISBN 0-315-68067-9

UNIVERSITÉ D'OTTAWA
UNIVERSITY OF OTTAWA

Abstract

We have developed a novel experimental approach for the study of the interaction of sheets of non parallel flux lines in hysteretic type II superconductors. First a saturation remanent magnetic flux is trapped in the plane of a disk specimen. Then sheets of flux lines, directed at an angle θ with respect to the orientation of the trapped flux lines, are made to enter through the broad faces of the disk by application of a magnetic field H_a.

We continuously monitor the evolution of the components of the magnetic flux density $\parallel$ and $\perp$ to H_a (i.e. $< B_z >$ and $< B_y >$) as H_a is raised to various intensities, ranging up to H_{c2} in the case of our Nb specimen, and then reduced to zero. In our investigation of a high T_c ($YBa_2Cu_3O_{7-x}$) ceramic, H_a exceeded H_*, the first full penetration field.

We applied the phenomenological Clem general critical state model to the analysis of our extensive observations. A computer program was developed to solve the four coupled differential equations of this theory with appropriate physical constraints for the situations prevailing in our experiment. This analysis provides detailed insight into the evolution of the intricate configurations of the magnetic flux density $\vec{B}(x)$, the critical current density, $\vec{J}(x)$, and electric field $\vec{E}(x)$ patterns as the injected and trapped flux lines are made to interact, unpin, migrate and undergo flux cutting processes.

The model is seen to generate the variety of complicated measured curves of $< B_y >$ and $< B_z >$ vs H_a very satisfactorily. We thus obtain information on the dependence of the critical current density for flux line cutting $J_{c\|}$ on the magnetic flux density B and on the ratio of $J_{c\|}$ to $J_{c\perp}$, the depinning critical current density for Nb, $PbBi$ and $YBa_2Cu_3O_{7-x}$.

Remerciements

J'aimerais tout d'abord remercier le Dr. M.A.R. LeBlanc pour son aide, ses nombreux conseils et son encouragement tout au long de ce projet. Les longues discussions sur une multitude de sujets en physique ont agrandi mes connaissances et m'ont incité à développer un plus grand intérêt. De plus, sa générosité et sa persévérance m'ont permis de compléter ce projet.

J'aimerais aussi remercier les professeurs du département de physique dont le dévouement cré un milieu propice à l'apprentissage et à la recherche ainsi que le personnel de soutien pour leurs contributions techniques à la réalisation de ce projet.

Finalement, je dédie cette thèse à mes parents. Sans leur support financier, leur appui moral ainsi que leur compréhension, mes études universitaires n'auraient pu se réaliser.

Contents

List of Figures

Chapter 1. INTRODUCTION

1.1 General Background

The liquefaction of Helium in 1908 by Kammerlingh Onnes led to the discovery of materials exhibiting new and mysterious properties. The resistivity of pure mercury was found to be immeasurably small when cooled to 4.2 K. Initially, this presented itself as no real surprise since it was already well established that the resistance of materials as they are cooled should gradually drop. Furthermore, the resistance of pure materials such as the mercury sample employed in the experiment directed by Onnes was expected to drop to zero at 0 K. In later experiments, the resistivity of mercury was continuously monitored as the temperature of the environment was reduced. Experimental observations showed that as the temperature was initially lowered, the resistivity gradually declined. However, at very low temperatures (comparable to the boiling point of helium), the resistivity was seen to abruptly fall to zero. This, occurring within an immeasurably small change in temperature.

This major discovery sparked a large number of workers to redirect their research toward this new phenomenon. Great efforts were spent in investigating the behaviour of the electrical resistivity for a vast array of materials. Within a relatively short period, the electrical resistivity at very low temperatures of many

metallic elements and alloys were shown to behave in a similar fashion as mercury. The temperature at which the resistivity suddenly dropped to zero was found to be different from one material to another. However, the various transition temperatures, which are often referred to as critical temperatures, were all found to be very low (below 10 K). An also noticeable difference was the range of temperature within which the resistivity dropped to zero. It was observed that this range was broader in cases where the material under investigation was impure. Because of the similarity between their electrical behaviour and the expected behaviour for a perfect conductor, these materials were labeled superconductors, thus giving birth to a new branch of physics.

1.2 Electromagnetic Properties of Superconductors

In the first twenty years after the discovery of superconductivity, it was believed that superconductors were merely perfect conductors. In 1933, Meissner and Oschenfeld measured the magnetic flux permeating tin and lead specimens while cooling from their transition temperatures in a magnetic field. A most extraordinary phenomenon was observed. The flux density in the specimens was expelled as the temperature traversed its critical temperature. This is in evident contrast with what is expected for a perfect conductor thus demonstrating that a superconductor is not merely a simple perfect conductor. The expulsion of flux from the specimen is explained in terms of persistent currents appearing at the surface of the specimen as the state of the metal changes from a normal resistivity state to a

superconducting state. These circulate in a direction so as to cancel the flux density inside the metal. This effect, known as the Meissner Effect, has been widely observed and investigated in an immense number of superconducting materials.

Further investigations on the magnetic properties of superconductors led researchers to classify these materials into two separate classes. The basis of this classification lies in the different magnetic behaviours observed in various materials. The first group, called type I superconductors, encompasses all the pure and homogeneous materials of ideal geometry which, in the presence of an external field, exhibits a complete Meisner effect when in the superconducting state. This occurs for any external field below a critical intensity. Field strengths greater than this critical field, denoted as H_c, are seen to quench superconductivity and return the normal resistivity state. Measurements of the critical field for various materials have shown that the strength of this field depends on both the superconducting material and the temperature of the specimen.

Some superconductors behave somewhat differently from those characterized as type I. These are labelled type II superconductors. Although the complete screening of magnetic flux from their bulk is observed at low fields, only partial screening occurs at higher fields. Two states are thus seen to exist in these superconductors, a pure superconducting state at low fields and a mixed state at higher fields. The field at which flux begins to penetrate the specimen is labelled as H_{c1} whereas the strength of field corresponding to total flux entry, thus the return of the normal resistivity state, is called H_{c2}.

We now examine in some detail the configurations of electric currents, magnetic fields and electric fields in type I and type II superconductors.

1.3 Type I Superconductors

It is well known that type I superconductors can support magnetic flux, electric currents and electric fields only in a thin penetration depth layer $\lambda \approx 1000$ Å along their surfaces. Consequently in bulk samples, i.e. where the dimensions are large compared to λ, the magnetic flux density $B(x)$, the current density $J(x)$ and the electric field $E(x)$ are zero everywhere both in the steady and dynamic state. Here x indicates the spatial coordinates. In the surface region, however, a persistent current density, $J_M(x)$ (the Meissner current density) is in thermodynamic equilibrium with $B(x)$. This equilibrium is expressed by London's equation,

$$\mu_o \lambda^2 \nabla \times \vec{J}_M = -\vec{B} \tag{1.1}$$

which states that the Meissner current density $J_M(x)$ is large where $B(x)$ is large and leads to exponential declines for $J_M(x)$ and $B(x)$ inside the penetration layer, thus

$$J_M(x) = J_M(0)e^{-x/\lambda} \tag{1.2}$$

$$B(x) = B(0)e^{-x/\lambda} \tag{1.3}$$

Here $x = 0$ indicates the surface and x the distance from the surface. It is important to note that $\vec{J}_M(x)$ always flows perpendicular to $\vec{B}(x)$ and in a diamagnetic sense. Thus,

$$\vec{F}_J = \vec{J}_M \times \vec{B} \tag{1.4}$$

the Lorentz force acting on $\vec{J}_M$ is always directed into the volume of the superconductor.

When changes of $B(x)$, hence $J_M(x)$ take place, because an externally applied magnetic field H_a is varied and/or a transport current I fed into the specimen is increased or reduced, an electric field $\vec{E}(x)$ appears in the penetration depth. The electric field $\vec{E}(x)$ is always perpendicular to $\vec{B}$ and directed along $\vec{J}_M$ if $\vec{B}$ is increasing but against $\vec{J}_M$ when $\vec{B}$ is decreasing. Consequently, the power $\vec{E} \cdot \vec{J}$ serves to increase (decrease) the kinetic energy of the Cooper pairs with no dissipation of energy when B, hence J increases (decreases). The electric field $\vec{E}(x)$ is largest where $\vec{B}$, hence $\vec{J}(x)$ are largest, i.e. at the surface. The energy entering the specimen, expressed by the Poynting vector,

$$\vec{S} = \frac{\vec{E} \times \vec{B}}{\mu_o} \tag{1.5}$$

is stored in the kinetic energy of the Cooper pairs and in magnetic energy $B^2/2\mu_o$ in the penetration when $\vec{B}$ has been made to increase. This energy is released (recovered) with no intervening losses when $\vec{B}$ is subsequently reduced to the initial value.

1.4 Ideal Type II Superconductors

For ideal, i.e. reversible hence pinning free, type II superconductors, the electromagnetic behaviour is somewhat more complex. The situation described above prevails over the range $0 < H_s < H_{c1}$, where H_s is the total field at the surface,

i.e. $\vec{H}_s$ is the superposition of any externally applied magnetic field $\vec{H}_a$ and the magnetic field generated by a transport current fed into the specimen. We stress that in all circumstances, the physical origin of H_s is immaterial and plays no role in the phenomena encountered and that the transport current is again confined to the penetration depth surface layer.

A fascinating and very different electromagnetic situation is encountered over the range $H_{c1} < H_s < H_{c2}$. Now a uniform distribution of quantized flux lines (vortices) all parallel to $\vec{H}_s$ permeate the specimen. The density of those flux lines, hence $B(x)$, is in equilibrium with H_s. Here $B(x)$ represents a quasi macroscopic average over the cross section of a flux line. Since the flux line distribution is homogeneous, $< B(x) >= B(x) = B_{eq}$.

We note that B_{eq} is always less than $\mu_o H_s$, hence M_{eq}, the magnetization of the ideal type II superconductor is always diamagnetic. Further $\mid M_{eq} \mid$ in the vortex state is always small compared to H_{c1}.

The vortex state is also referred to as the Shubnikov phase, Abrikosov state or mixed state. In this vortex state, the ideal type II superconductor cannot sustain a lossless electric current transverse to the flux lines, i.e. perpendicular to $\vec{B}(x)$. Consequently the critical transport current is zero in these materials when the total field at the surface exceeds H_{c1}. If a steady transport current I is fed into the specimen, an electric field $\vec{E} = \vec{B} \times \vec{v}$, appears perpendicular to $\vec{B}$ and leads to an energy dissipation $\vec{E} \cdot \vec{J}$. The voltage observed along the specimen is referred to as the flux flow voltage since here $\vec{v}$ denotes the velocity of migration of the flux lines. We note that $\vec{v}$ is always perpendicular to $\vec{B}(x)$. When the voltage driving

the current I through the specimen is removed, the gradients in $\vec{B}(x)$ generated by I collapse and the flux configuration returns to a uniform distribution.

It is less well known and understood that the ideal type II superconductor in the vortex state can sustain a lossless current density $\vec{J}$ provided that $\vec{J}$ flows exactly and only parallel to the flux lines, i.e. $J_\perp = 0$. These situations where the Lorentz force is zero are known as force free configurations since here, $\vec{F}_L = \vec{J} \times \vec{B} = 0$. The limit or critical value of $J_\parallel$ before the onset of dissipation, denoted $J_{c\parallel}$, has been investigated theoretically by Brandt et al [8] and Clem and Yeh [12]. These authors have calculated, $\Delta\theta_c$, the difference of orientation between two adjacent sheets of flux lines which leads to a disappearance of their mutual repulsion and to the onset of flux line cutting. The change of direction of adjacent sheets of flux lines in the flux line lattice requires, according to Maxwell's equation, that a current be flowing through the two adjacent sheets and parallel to $\vec{B}$, in order that this occur. Thus the critical angle $\Delta\theta_c$, where the mutual repulsion vanishes and flux line cutting takes place, corresponds to a critical current density. The theory however leads to values for $J_{c\parallel} \approx 10^{12}\ A/m^2$, immensely greater than any observed. We note however that $J_{c\parallel}$ in pinning free (ideal) type II superconductors has scarcely been studied experimentally.

1.5 Hard Type II Superconductors

The presence of pinning sites in the body or bulk of ideal type II superconductors transforms these materials into substances referred to as irreversible or hysteretic or hard superconductors.

Pinning sites consist of physical defects (dislocations, grain boundaries, voids and cavities) and/or chemical imperfections (eg. segregation of impurities, separate phases etc.). These can impede the movement of flux lines and freeze these into place. As a consequence, steady state gradients can be established in the distribution of the flux line density. By Maxwell's equation, $\nabla \times \vec{B} = \mu_o \vec{J}$, these gradients of $B(x)$ correspond to a macroscopic conduction (true) current (the persistent currents circulating around the axis of a vortex are "localized" currents). When the Lorentz driving force density $\vec{F}_L = \vec{J} \times \vec{B}$ is exactly balanced by the pinning force density $\vec{F}_p$, a critical state is said to exist where $J = J_c$. It is useful to write the Lorentz force in scalar form, thus $F_L = J_\perp B$, which emphasizes the important feature that it is only the component of $\vec{J}$ perpendicular to $\vec{B}$ which leads to flux line depinning and flux line migration. The critical value $J_\perp = J_{c\perp}$ depends on temperature, magnetic flux density and the pinning parameters of the material.

Phonons are generated and produce heat when flux lines unpin and the stresses caused by the Lorentz force on the metallic lattice in the pinning site are released. Further, the migration of a flux line from one set of pinning sites to another set is dissipative since this drives Cooper pair currents through the normal core. Consequently, an electric field $\vec{E}$ perpendicular to the axis of the flux line, hence

$\perp$ to $\vec{B}$ and $\parallel$ to the depinning critical current density $J_{c\perp}$ appears and energy is dissipated both when $J_\perp$ is increasing and decreasing.

The evolution of the spatial average of the magnetic flux density, $< B >$, when H_s is varied and cycled by changing H_a and/or the transport current I is irreversible (hysteretic) and the accompanying losses (termed A.C. or hysteretic losses) have been extensively studied in hard superconductors, particularly in low T_c materials. The dependence of $J_{c\perp}$ on temperature, on magnetic flux density B and on the density, distribution and nature of pinning sites has also been extensively investigated.

The flux line cutting critical current density $J_{c\parallel}$ in these materials has received very little attention possibly because this quantity is less important for applications, but also perhaps because this phenomenon is more difficult to study.

Indeed most of the experimental work on the electromagnetic phenomena arising from flux line cutting and on the determination of the dependence of $J_{c\parallel}$ on B and its relationship to pinning hence to $J_{c\perp}$, has been pursued in our laboratory.

At first glance measurements of $J_{c\parallel}$ appear straightforward. Many workers monitor the onset of resistance using a four probe arrangement as a transport current is fed into a wire or ribbon immersed in a static magnetic field H_a directed along the length of the specimen. This procedure is valid when H_I, the magnetic field generated by the current I is small compared to H_a. It is however inappropriate for a bulk sample when $H_a \leq H_I$. Here, the pattern of current flow in the specimen is extremely intricate. The evolution of the magnetic flux threading the specimen along H_a, hence along I, as well as the voltage appearing along the

specimen as I is impressed and varied, must also be monitored in order that a complete picture of the intricate configurations of $\vec{B}(x)$ and $\vec{J}(x)$ be obtained.

In this thesis we develop a new approach for the study of flux line cutting phenomena, the determination of $J_{c\|}$, its dependence on B and its link with $J_{c\perp}$. We apply this technique, valid for all H_a from zero to H_{c2}, to investigate the behaviour of both a conventional low T_c hard superconductor (Niobium) and a high T_c material. We apply the only model existing to date to account for these phenomena, the Clem model. From this analysis we extract a detailed picture of the sequences of magnetic flux density configurations, current density patterns and electric field structures which arise in the situation under study. We show that the model reproduces our numerous observations very satisfactorily. We also obtain information on the ratio of $J_{c\|}$ to $J_{c\perp}$ for these samples and their dependence on B from this analysis.

Chapter 2. EXPERIMENTAL ARRANGEMENT

2.1 Introduction

A hard superconductor in the form of a thin disk is mounted to permit free rotation about an axis through its center and perpendicular to its faces. Magnetic flux is trapped inside the specimen through the application and removal of an external field applied parallel to the faces of the disk and of intensity well above H_{c1}. The disk and therefore the trapped flux is then rotated in zero field through some selected θ where $0 < \theta < 180°$. The external field is then cycled between $H_a = 0$ and $H_{c1} < H_a < H_{c2}$ allowing new flux to permeate the disk and interact with the flux initially trapped inside the specimen. Two sets of orthogonal pick-up coils embrace the sample and are used to monitor the magnetization of the specimen both along and perpendicular to the direction of the applied field. The *emfs*,denoted v_{in}, induced in each coil are independently fed to an electronic amplifier-integrator which produces an output voltage proportional to $\int v_{in}\, dt$. An X—Y recorder is connected to each amplifier-integrator and each displays the variation of a component of the magnetization of the sample (Y–axis) versus the change in the applied field (X–axis). A heater covering the disk completely is formed by winding non-inductively an enameled manganin wire tightly around the sample such that good

thermal contact between the heater wire and the disk is achieved. This allows us to drive the specimen, whenever desired, from the superconducting state to the normal state and thus erase all previous magnetic history acquired by the disk. Furthermore, heating the specimen in any given field yields an absolute measure of the magnetization acquired by the disk. This feature is employed to extract valuable information throughout the measurements and also serves a purpose in calibrating the magnetization curves (see §2.4).

The external applied field was produced by a solenoid which was long enough to provide an acceptably uniform field over the volume of the sample. Measurements were done on both a low and a high T_c superconductor. Since the former required liquid helium to attain the superconducting state, the experimental set-up was different from the one used for the high T_c specimen for which liquid nitrogen was employed as the coolant. In this thesis, the experimental arrangement for the high T_c superconductor is described. We refer the reader to the thesis of Boyer [5] or Sekerka [26] for a complete description of the low temperature system.

The results obtained for both specimens are then compared and their similarities and differences are discussed. In order to gain more insight in the behavior of flux interaction, computer simulations of the experimental results were carried out based on Clem's model. Results of these calculations are presented and compared with those obtained experimentally.

Details on the samples used, the experimental arrangement (for the high T_c) and procedures are now described.

2.2 Experimental Arrangement

2.2.1 Samples Employed

The superconducting specimens used were in the form of thin disks whose diameters were much larger than their thickness. This geometry was chosen mainly for two reasons.

- The demagnetization effects are negligible for this type of geometry, as it is for a long slab or a long thin rod, if the field is applied along the flat surfaces of the disk.
- Since our measurements involved the rotation of the specimen, symmetry about its axis of rotation was imperative.

The magnetic properties of two superconducting materials were studied.

- Niobium which is a conventional low critical temperature superconductor.
- $YBa_2Cu_3O_{(7-x)}$ which is a high critical temperature superconductor.

Unlike $YBa_2Cu_3O_{(7-x)}$, Niobium has a relatively low B_{c2} ($\sim 375mT$). This allowed us to make measurements in the vicinity of its upper critical field.

Both samples employed showed moderate pinning and were therefore convenient specimens for the purpose of our study. Futhermore, auxiliary measurements on these samples showed that they are isotropic, thus convenient for rotation purposes.

The following table details the relevant parameters of the samples used.

Sample	Diameter (mm)	Thickness (mm)	T_c (K)	$\mu_o H_*$ (mT)
Niobium	19.0	0.55	9.2	190
$YBa_2Cu_3O_{(7-x)}$	22.0	2.7	94	11

Table 2.1: Physical properties and geometrical dimensions of the specimens

2.2.2 Disk Assembly

The disk was fitted in a delryn support to permit the winding of the heater (see Fig 2.1(a)). An enameled manganin wire, gauge no.38, was wound tightly around the disk allowing good thermal contact between the sample and the wire. This permits the destruction of previous magnetic history of the sample by heating it above T_c, thereby ensuring that every measurement in any chosen field H_a is started with a 'clean slate'. Manganin was used mainly because of its non-magnetic properties and its high resistivity. The latter is of importance since it allows us to reach the critical power necessary for driving the superconductor in the normal state using fairly low currents (a few hundred milliamps). The heater was wound noninductively to eliminate the magnetic field and magnetic moment produced by the heater current. This was achieved by wrapping two equally long wires of manganin side by side around the disk. The ends of the wires were then

connected together so that the currents flowed in opposite directions in the two segments thereby producing fields which cancelled each other out.

Two thin brass cups with diameters slightly larger than the delryn disk support and thickness of approximately 0.3 mm were rigidly attached to each side of the disk. The heater wires were soldered to each cup. Thin rods, 1.5 mm in diameter and 19.0 mm long protrude from the outer surfaces of the brass cups. A small gear firmly attached to one of the rods serves to rotate the disk (see Figs 2.1(b), (c)).

Thin rectangular strips of phosphor bronze were placed in physical and therefore electrical contact with these rods. Wires were soldered to the strips and connected to a power supply which controlled the heating of the sample.

The power needed to heat the superconductor from the ambient temperature up to the normal state was very dependent on the thermal contact between the sample and the cryogenic liquid. For instance, it was observed that for two different disk-coil systems with the same heater resistance, the power required to drive the $YBa_2Cu_3O_{(7-x)}$ disk in the normal state varied from 1 watt to approximately 25 watts. In the former case, the disk was very well insulated from the liquid nitrogen therefore requiring very little heating. A disadvantage in this former case is the long time required for the superconductor to cool down below its transition temperature after the heating procedure.

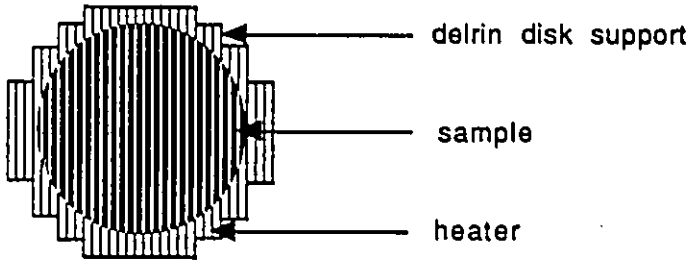

(a)

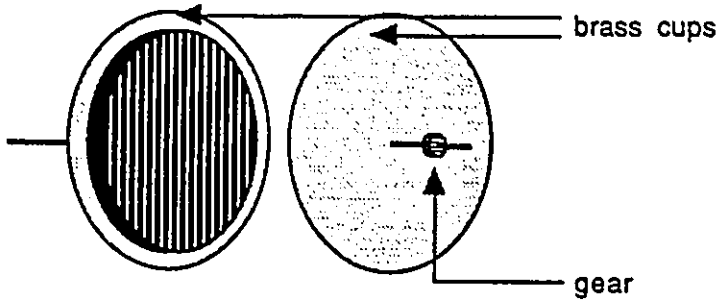

(b)

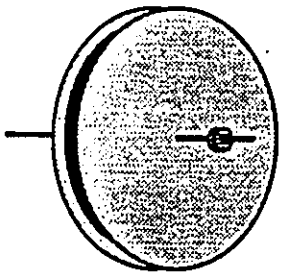

(c)

Figure 2.1: Disk assembly.

2.2.3 Pick-up Coils Assembly

Two rectangular pick-up coils with 40,000 turns each of copper wire gauge no.46 were constructed and employed to monitor the magnetization of the sample. Each pick-up coil consisting of two halves electrically connected in series with each other encompassed the disk. The inner coil monitored the variation in the magnetization of the superconductor perpendicular to the field whereas the outer coil placed perpendicular to the inner coil monitored the variation of the magnetization of the sample parallel to the field (see Fig 2.2).

The *emf* induced in the outer coil is caused by the variation in the magnetization of the sample and also by the change in the applied field. The information obtained from the signal received by the X—Y recorder would therefore represent the magnitude of the magnetic density $\vec{B}$. Although the information about the magnetization of the sample could very well be extracted from curves of B vs H_a, it was found more convenient for our purposes to place a bucking coil connected in series opposition with the outer coil. The purpose of this coil was to cancel out the contribution of the applied field from the signal sent to the integrator-amplifier. The balancing of this coil was done at liquid nitrogen temperature with the disk in the normal state where its magnetization is zero.

Once balanced, a net signal proportional to the component of the magnetization parallel to the field was obtained. A first approximation for the number of turns required by the bucking coil was calculated as follows.

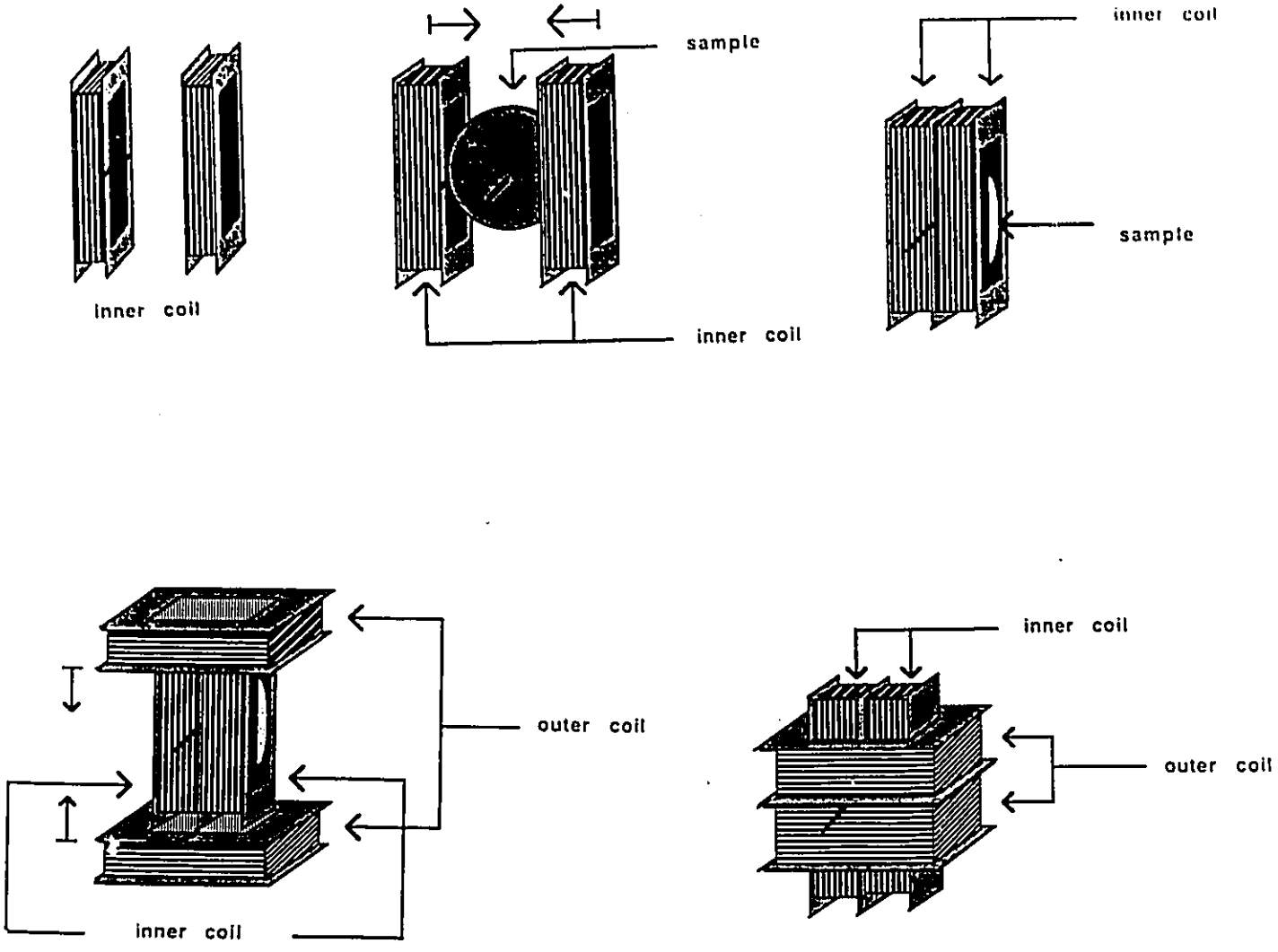

Figure 2.2: Pick-up coils assembly.

From Faraday's law of magnetic induction, the *emf* induced in the pick-up coil is:

$$\varepsilon_p = -N_p \frac{d < \phi_p >}{dt} \tag{2.1}$$

The magnetic flux threading this coil is simply :

$$< \phi_p >= \mu_0 \ < A_p > \ H_a + \mu_0 \ < A_s > < M > \tag{2.2}$$

where the first term represents the contribution of the external field to the total flux and the second term is the contribution of the specimen's magnetization.

Substituting equation (2.2) in (2.1) leads to,

$$\varepsilon_p = -\mu_0 \, N_p \left(< A_p > \frac{dH_a}{dt} + < A_s > \frac{d < M >}{dt} \right) \tag{2.3}$$

where :

N_p	represents the number of turns in the pick-up coil.
A_p	is the cross section of the coil.
A_s	is the cross section of the specimen.
H_a	is the applied field.
$< M >$	is the spatial average of the magnetization acquired by the specimen.

Similarly, for the bucking coil,

$$\varepsilon_b = -N_b \frac{d < \phi_b >}{dt} \tag{2.4}$$

$$< \phi_b >= \mu_0 H_a < A_b > \tag{2.5}$$

$$\varepsilon_b = -N_b < A_b > \mu_0 \left(\frac{dH_a}{dt}\right) \tag{2.6}$$

Since the coils are connected in series opposition, the net *emf* is simply the difference between the *emfs* induced in each coil,

$$\varepsilon_{net} = \varepsilon_p - \varepsilon_b \tag{2.7}$$

substituting the expressions (2.3) and (2.6) into (2.7),

$$\varepsilon_{net} = -\mu_0 \left[\frac{dH_a}{dt}(N_p < A_p > -N_b < A_b >) + N_p < A_s > \frac{d < M >}{dt}\right] \tag{2.8}$$

Now in the normal state the specimen is non magnetic, therefore :

$$M = 0 \qquad \Rightarrow \qquad \frac{dM}{dt} = 0 \tag{2.9}$$

expression (2.8) reduces to :

$$(\varepsilon_0)_{net} = -\mu_0 \frac{dH_a}{dt}(N_p < A_p > -N_b < A_b >) \tag{2.10}$$

To eliminate the dependence of H_a on the monitored signal, the bucking coil was constructed such that :

$$(\varepsilon_0)_{net} = 0 \tag{2.11}$$

this occurs if :

$$N_p < A_p >= N_b < A_b > \tag{2.12}$$

Since the left-hand side of the last equation can easily be estimated, the number of turns required by the bucking coil for balancing can be roughly calculated. Extra turns were wound before the final experimental adjustments since it is easier to remove than add turns to the bucking coil.

For the final adjustments, the pick-up coil was placed a few centimeters above the bucking coil inside a delryn support system (see Fig 2.3). The latter was then placed inside a long copper solenoid whose purpose was to produce the external magnetic field. The *emfs* induced in each coil as the applied field varied in intensity was generated only by the variation in the intensity of the external field since the specimens employed were non-magnetic in the normal state. The net signal was monitored by the X—Y recorders and turns were removed from the bucking coil until a null signal was received by the recorders. After balancing, the bucking coil possessed approximately 58,000 turns of copper wire gauge no.46.

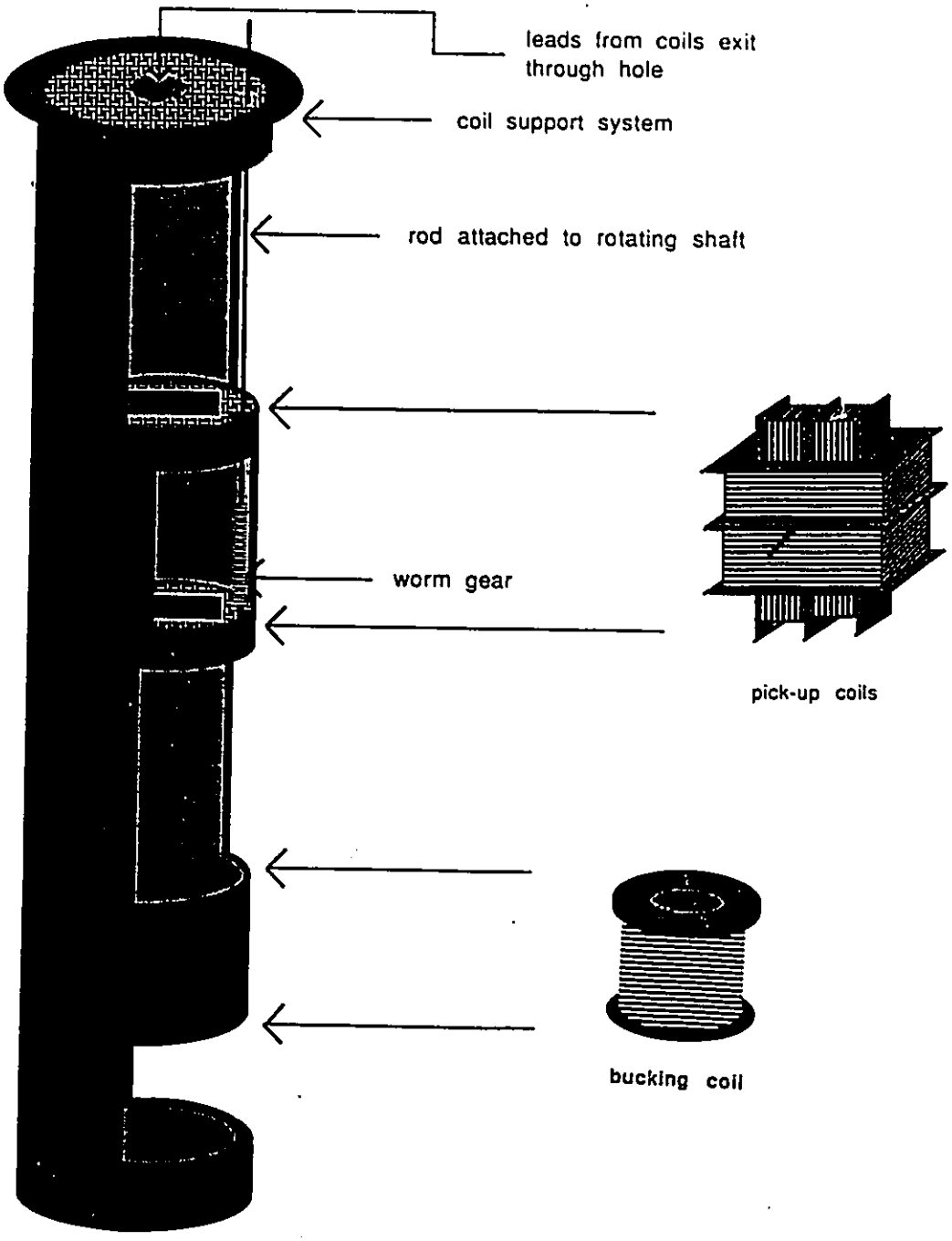

Figure 2.3: Support system for disk sample and pick-up coils.

2.3 Copper Solenoid

A copper solenoid consisting of 4,160 turns of copper wire gauge no.18 was constructed and used to produce the required external magnetic field. Its length, external diameter and inner diameter were 22.0 cm, 12.0 cm and 5.0 cm respectively. The end wires were connected, via a shunt resistor, to a power supply capable of generating a steady current of approximately 3 amps. The corresponding field is of the order of 70 mT which was large enough for the purpose of our measurements.

The system consisting of the sample, the coils and the heater was placed inside the solenoid and near its center such that the system bathes in a uniform field (see Fig 2.4). Leads were connected from the shunt resistor to the X-axes of the two X—Y recorders. In this manner, the evolution of the Y and Z components of the magnetization as a function of the external field could be measured. The solenoid including the sample and the coils was placed in a large liquid nitrogen bath to cool the disk below its transition temperature. A schematic of the electric circuit for the entire system is shown in Fig 2.5.

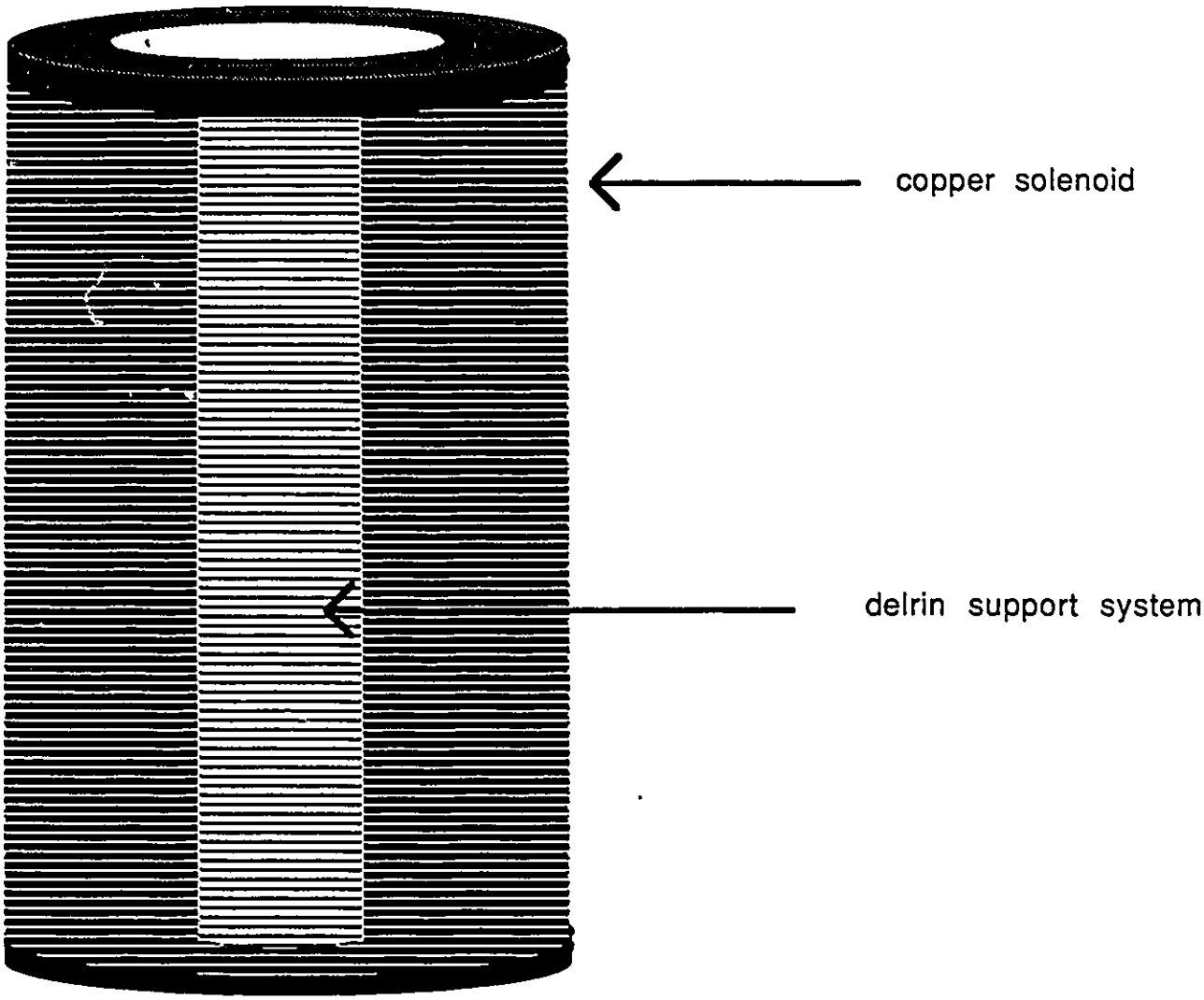

Figure 2.4: Copper solenoid.

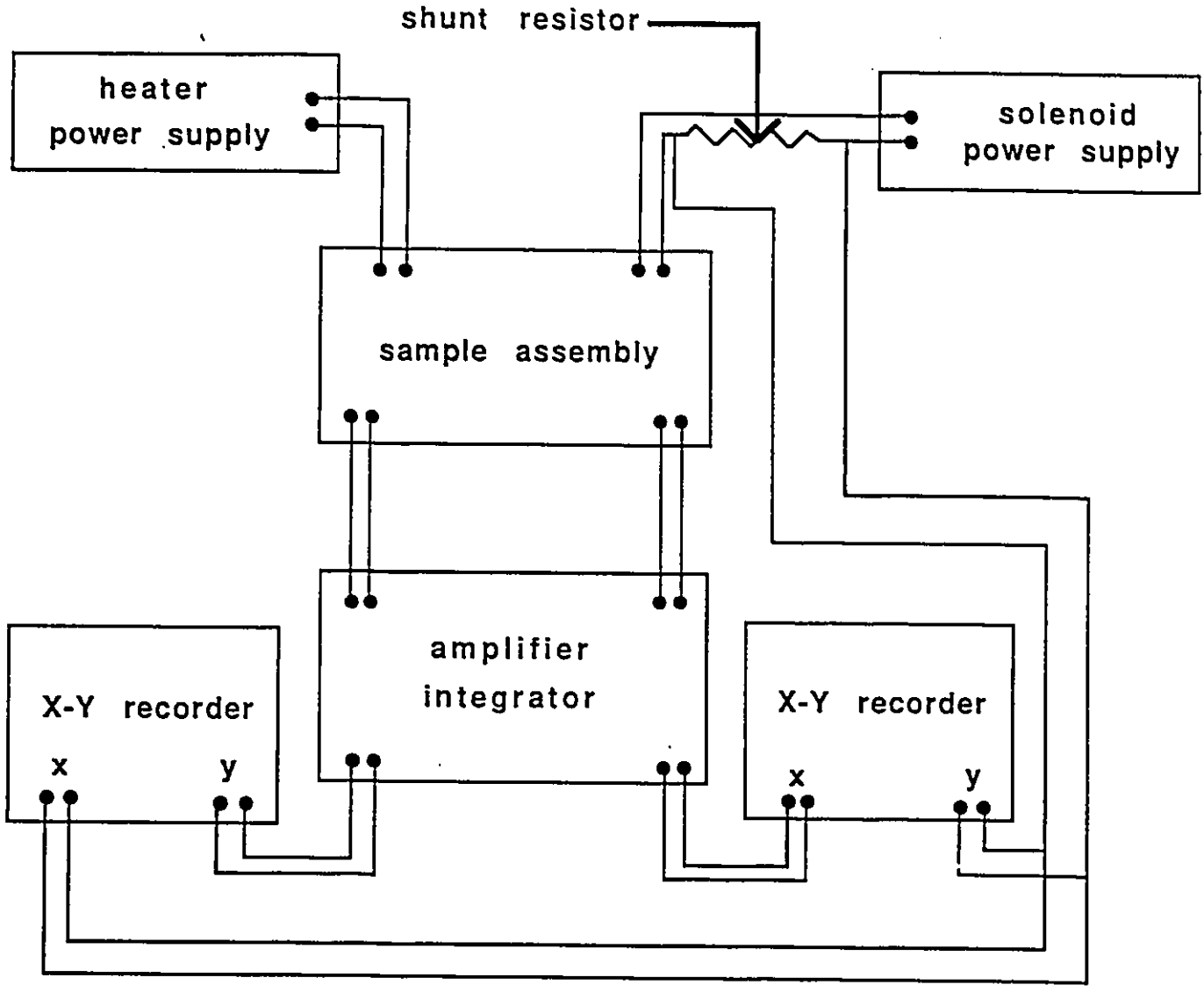

Figure 2.5: Electrical circuit for experimental set-up.

2.4 Calibration

In order to extract quantitative information from the experimental magnetization curves, an initial set of measurements was done to calibrate the signals $< M_z >$ and $< M_y >$ perceived by the pick-up coils and to determine the background signal which may arise due to an imperfect balancing by the bucking coil.

Fig 2.6 shows a standard magnetization curve for a weak pinning superconductor ($< M_z >$ vs H_a). A linear region bounded by the limits $H_a = 0$ and $H_a = H_{c1}$ appears due the near-perfect screening against the entry of the applied magnetic field. Here we choose to neglect the flux entry within the penetration depth since it is minute compared to the thickness of the specimens employed.

The $< M_z >$ signals from the pick-up coils are calibrated on the assumption that perfect shielding against the entry of H_a occurs under application of magnetic flux to the virgin state in the range $H_a < H_{c1}$. Virgin is defined as the state of the sample when it has become superconducting by cooling in the absence of a magnetic field from $T \geq T_c$ to some $T < T_c$. In this work, and in many investigations, the presence of the earth's magnetic field is negligible.

The $< B_y >= \mu_0 < M_y >$ data is calibrated against $< M_z >$ by rotating an arbitrary residual magnetic moment (remanent trapped flux) of the superconducting disk from the z to the y direction. Magnetic flux is trapped in the superconductor by either, *(i)* subjecting it to a sweep of magnetic field H_a of magnitude well above H_{c1} or, *(ii)* letting the disk become superconducting in a static field H_a (which may be greater or less than H_{c1}). In both procedures, it is imperative that H_a be reduced to zero, before the disk is rotated since, as shall be seen later, flux cutting

that is generated by rotation when $H_a \neq 0$ will lead to the release of some of the trapped flux and also affect the alignment and distribution of flux inside the disk Sinusoidal curves of $\mu_0 < M_y >=< B_y >$ and $\mu_0 < M_z >=< B_z >$ are mapped out as the superconducting disk (with trapped flux) is rotated. The $< M_z >$ signal maps out a cosine curve while the $< M_y >$ signal generates a sine curve as the rotation of the trapped magnetic moment proceeds from the z axis through the y axis, then toward the negative z direction and so on. The amplitudes of the two resulting sinusoidal curves display the same magnetic moment. Since $< M_z >$ is known from the standard calibration indicated previously, the calibration of $< M_y >$ follows.

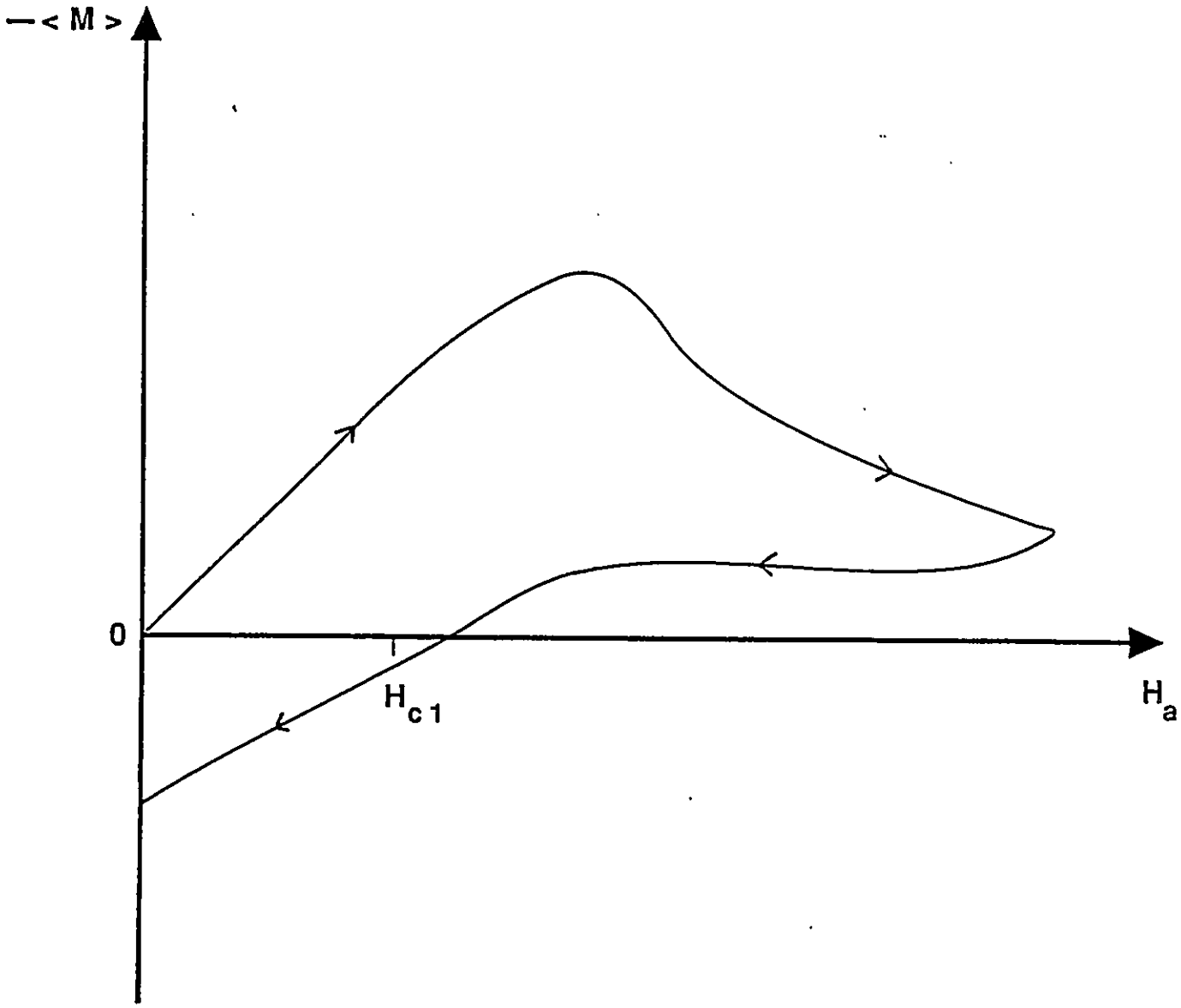

Figure 2.6: Standard magnetization curve for a weak pinning superconductor.

Chapter 3. TILTED FLUX LINES (EXPERIMENTAL)

3.1 Framework of the Investigation

In this chapter, the behaviour of flux line interaction is studied when new vortices are forced to permeate the disk and interact with parallel sheets of pinned flux lines directed at some chosen angle θ with respect to the invaders.

These sheets may be trapped in a type II superconductor through various methods. The procedure employed consisted of subjecting the disk to a sweep of a magnetic field $\vec{H}_a$ which is then removed. To ensure that this cycle induces persistent currents to circulate in the same sense over the entire cross-section of the disk, hence trap a maximum amount of flux, the excursion of $\vec{H}_a$ must exceed a threshold field which we will denote as H_{sat}. Alternatively, the specimen may be cooled from T_c to the ambient temperature in a magnetic field of strength greater than H_* which is then removed. The physical sense of H_* and H_{sat} and their field strengths will be examined in the next section.

The procedures just described magnetizes the disk with a saturation residual moment whose intensity depends mainly on the pinning strength of the material. The disk is then rotated through a selected angle ($0 < \theta < \pi$) in zero field. Once the disk has been rotated through the desired angle, a magnetic field of

intensity H_a directed parallel to its flat surfaces is impressed. The application of this field causes flux lines directed along $\vec{H}_a$ ($\theta = 0$) to migrate in the disk which is already filled by a lattice of parallel flux lines all oriented at some angle θ. The disk and its content of magnetic flux were rotated to achieve this objective. The magnetization of the disk both along and perpendicular to the external applied field is continuously monitored as the new flux lines encroach upon an array of pinned flux lines, the two populations subtending an angle θ relative to each other.

The behaviour for this type of interaction was extensively studied for various angles. In section 3.3, some of the experimental results are presented for $\theta = 45°, 90°$ and $135°$. In the next section a brief description of the physical sense of H_* and H_{**} is presented.

3.2 Determination of H_* and H_{**}

To fully understand the significance of H_* and appreciate its usefulness in characterizing and comparing non ideal type II superconductors, it is perhaps best to examine the succession of magnetic profiles as the external field is cycled between $H_a = -H_{c2}$ and $H_a = H_{c2}$. These are depicted in Fig 3.1 and should prove useful in providing a descriptive picture of H_*.

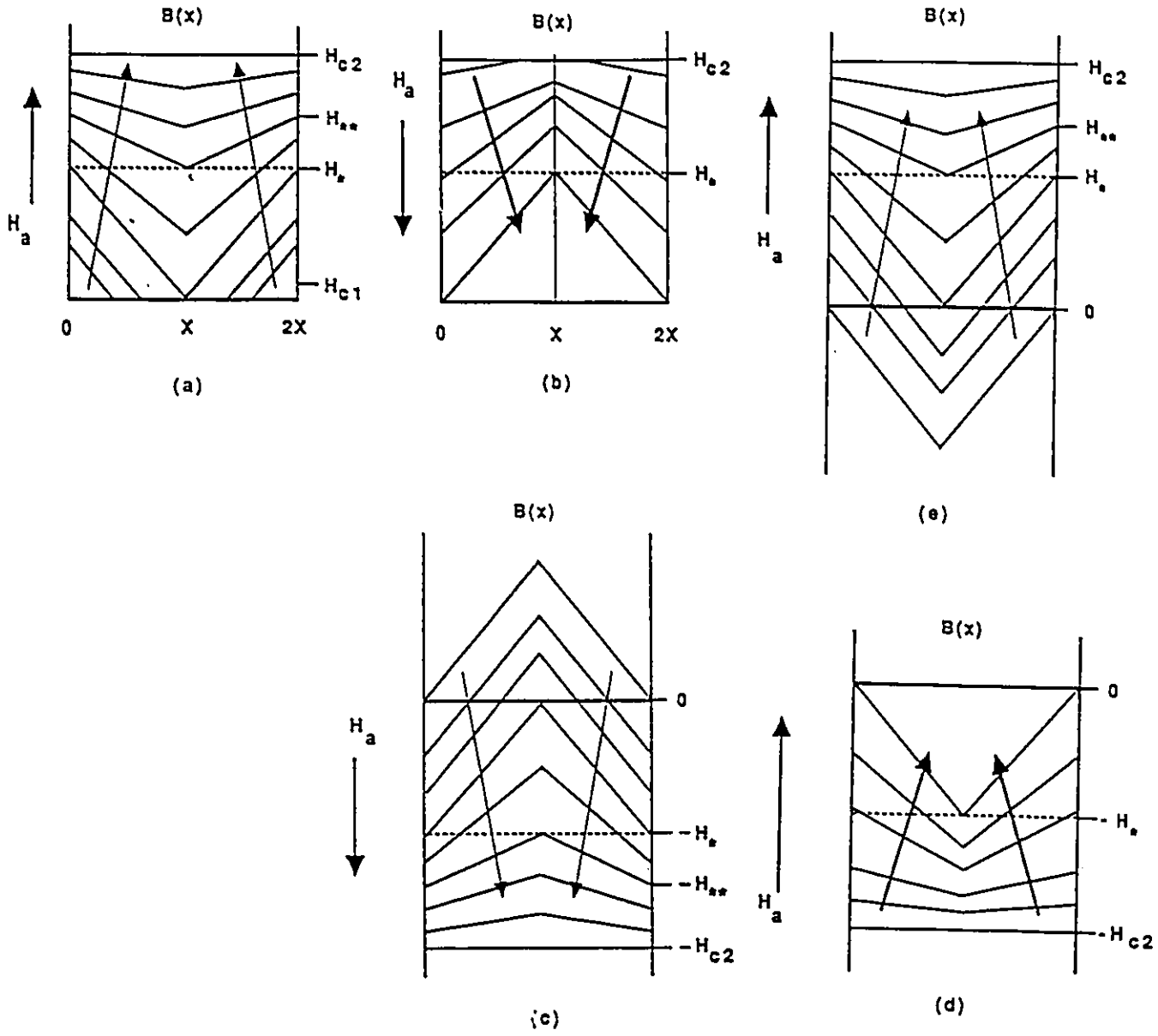

Figure 3.1: Profiles of flux line density as H_a is cycled between $-H_{c2}$ and H_{c2}. The midplane of the disk is situated at X and the width of the sample is 2X.

The reader is first referred to figure 3.1(a) where the evolution of the profiles is depicted as H_a is first increased from 0 to H_{c2}. Starting with $H_a = 0$ and the specimen in the virgin state, the initial application of H_a induces a persistent current shielding the disk from any flux encroachement.

As H_a is increased above H_{c1}, magnetic flux lines gradually permeate the disk, initially invading the region near the surface and slowly moving inward toward the center of the specimen. Due to flux pinning, the density of the flux lines decrease with depth from the surface. When $H_{c1} < H_a < H_*$, the front of the advancing flux configuration (B profile) falls to zero between the surface and the center of the specimen. In these situations a virgin region, i.e. a region clean of any flux lines, exists near the midplane.

As H_a is further increased, the flux lines, being pressed further inward, finally reach the midplane. The strength of the external field required for the flux lines to just reach the midplane is denoted as H_*. At this juncture persistent currents are seen to circulate in the same sense throughout the disk. As H_a approaches H_{c2}, the field gradient inside the specimen becomes shallower and becomes zero when H_{c2} is reached. The flux density is then uniform throughout the disk.

We now turn our attention to figure 3.1(b). As the intensity of the external field is lowered from H_{c2} to zero, the flux lines inside the disk gradually leave the specimen as their mutual repulsion causes depinning from the pinning sites. Initially only the flux density near the surface of the disk is seen to diminish. As H_a is further decreased, the number of flux lines depinned and pushed out of the disk by the outward directed Lorentz force is seen to increase. Consequently the unaffected region near the center of the disk becomes narrower. When H_a finally

reaches zero, some of the flux initially threading the specimen remains pinned and is referred to as trapped flux. In this case the Lorentz force, which tends to push the flux lines outward, is in equilibrium with the pinning force holding the flux lines inside the disk. The local flux density is determined by the pinning strength of the material.

Figs 3.1(c) and 3.1(d) displays sequences of flux density profiles in the superconducting disk as the external field is now cycled from $H_a = 0$ to $H_a = -H_{c2}$ and back again to $H_a = 0$. Flux line annihilation as well as flux migration plays a role in the variation in the flux density profiles as H_a varies from 0 to $-H_*$.

Fig 3.1(e) represents the evolution of the flux density as H_a is again increased from 0 to H_{c2}. Thus a full cycle of H_a is completed. In this final sequence, the profile corresponding to an external field of H_* and all subsequent profiles are found to be identical to those produced by the first application of H_a (Fig 3.1(a)).

Ideally we could place a probe at the center of the specimen to determine when the flux lines just reach the midplane. We circumvent the difficulties and problems associated with this procedure by exploiting a simple method for determining the intensity of H_*. This can easily be achieved by monitoring the magnetization as the field is cycled between $-H_{c2}$ and H_{c2}. H_* is then determined to be the field strength corresponding to the onset of overlap of the various segments in the magnetization curve (Fig 3.2).

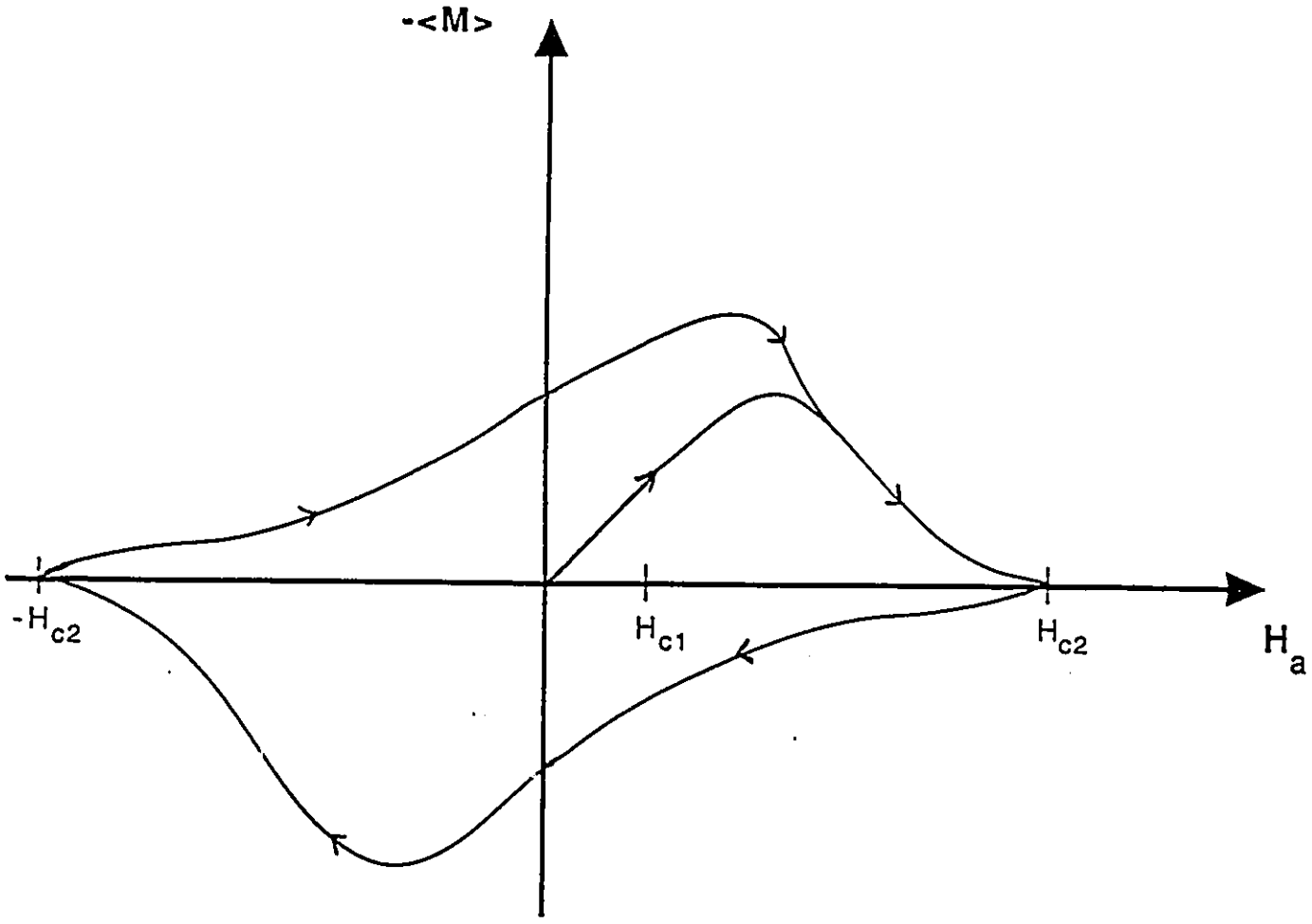

Figure 3.2: Magnetization curve as H_a is cycled between $H_a = -H_{c2}$ and $H_a = H_{c2}$.

To determine the intensity of H_{**}, we proceed in a manner similar to that used for H_{*}. In this case half-cycles are produced instead of full cycles. The former consist of cycling the external field between $H_a = 0$ and $H_a = H_{c2}$ (see Fig 3.3). The intensity of H_{**} is then determined by the point where the hysteresis loop intersects the initial magnetization curve. The sequence of profiles as H_a is cycled between $H_a = 0$ and $H_a = H_{c2}$ is schematically depicted in Fig 3.4.

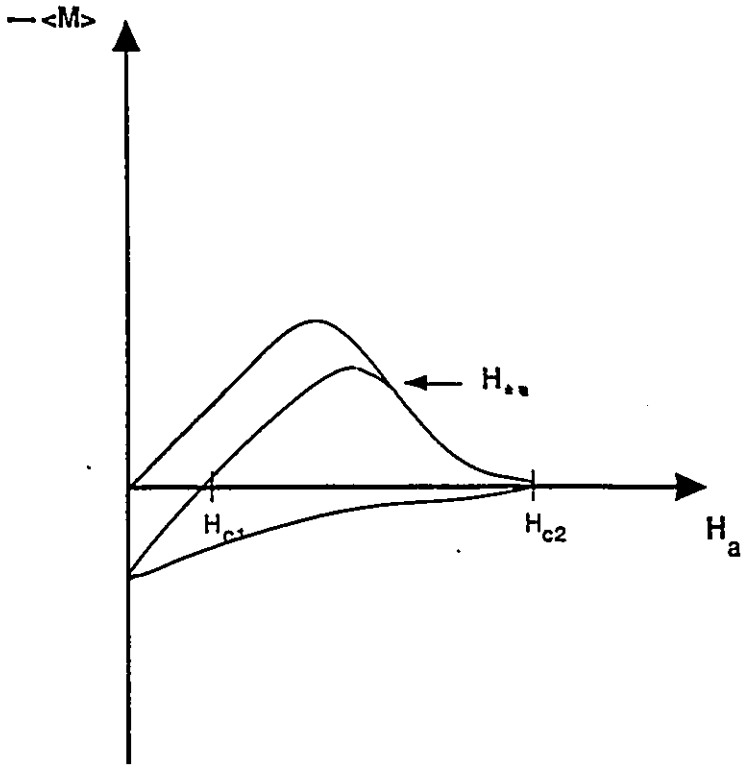

Figure 3.3: Magnetization curve as H_a is cycled between $H_a = 0$ and $H_a = H_{c2}$.

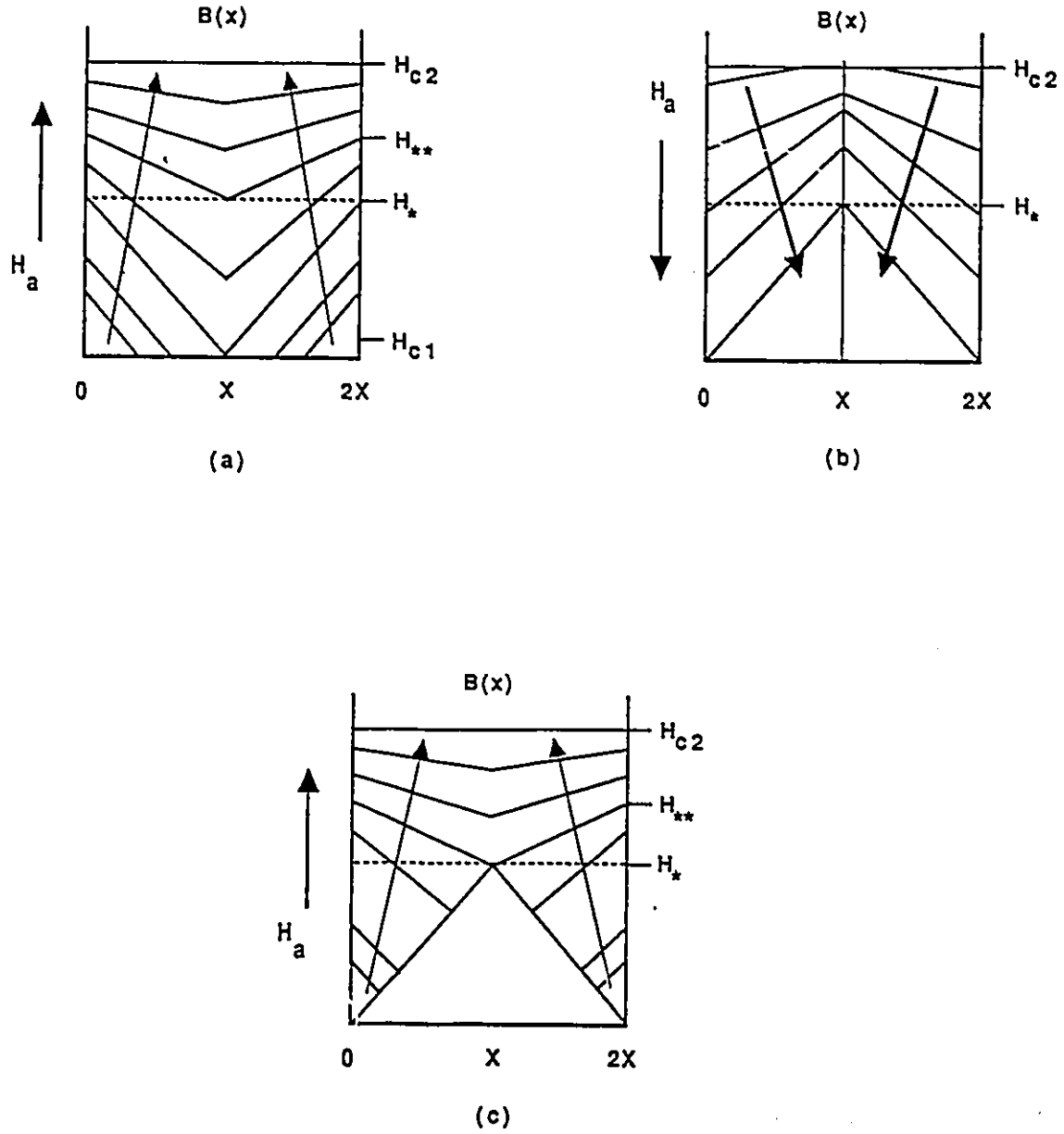

Figure 3.4: Sketches of B profiles as H_a is cycled between 0 and H_{c2}.

3.3 Experimental Results

An illustrative selection of our extensive observations on the behaviour of the trapped flux in a conventional low T_c type II superconductor (Niobium) and a high T_c specimen ($YBa_2Cu_3O_{7-x}$), as new flux lines, directed at some angle θ with respect to the trapped flux, are made to enter the disk, is displayed in Figs 3.5 through 3.17.

The first group of figures (3.5 through 3.11) pertain to the Niobium sample where the measurements were carried out at 4.2 K. The second group (Figs 3.12 through 3.17) correspond to the high T_c material where the data was obtained at 77 K.

For each specimen we present results for three θ directions, namely $\theta = 45°, 90°$, 135°. Also for each material and each direction θ, we examine the evolution of the trapped flux not only when H_a is impressed but also during the subsequent reduction of H_a from some selected value. Further, for each specimen and each direction θ, we have investigated the effect of repeated applications of H_a, i.e. the accumulated influence of a sequence of half cycle sweeps of H_a on the trapped flux. Since the magnitude of a swing of H_a plays an important role in altering the status of the trapped flux, we have performed measurements for various series of half cycles differing in the amplitudes selected for each series.

Our measurements reveal that the evolution of $< M_z >$, the magnetization of the specimen along the direction of the applied magnetic field H_a, is insensitive to the direction of the trapped flux. The projection along the z-axis of the magnetic moment associated with the trapped flux will of course, displace the starting

point for these curves. Thus $< M_z >_i$, the initial magnetization along the z direction is given by $< M_z >_i = < M >_{trapped} \cos\theta$. The subsequent evolution of $< M_z >$, however, as H_a is impressed, removed and cycled, displays no significant differences with data obtained by the standard procedure of previously inducing a magnetization along the z direction of corresponding magnitude and sign by an appropriate sweep of H_a. Consequently, we have not burdened this thesis with a display of the curves of $< M_z >$ vs H_a corresponding to the array of observations presented in Figs 3.5 through 3.17.

The reader will readily notice however from an inspection of these figures that the component of the magnetic moment orthogonal to H_a undergoes dramatic changes as H_a is impressed, removed and subsequently cycled.

For the Niobium specimen our range of observations extends not only beyond H_* and H_{**} but attains H_{c2} since these magnetic fields were easily accessed with our superconducting solenoid. For the high T_c material however, H_{c2} exceeds the capacity of our modest copper solenoid immersed in liquid nitrogen. Nevertheless our measurements span a large enough range to witness a dramatic alteration of the trapped flux by the entry of new flux lines directed at various chosen angles θ. It will emerge from the theoretical modeling of these phenomena that the relevant benchmarks or parameters are H_* and H_{**}. These important "boundary" magnetic fields are radically smaller in the high T_c specimen than H_{c2} and are easily reached by our apparatus.

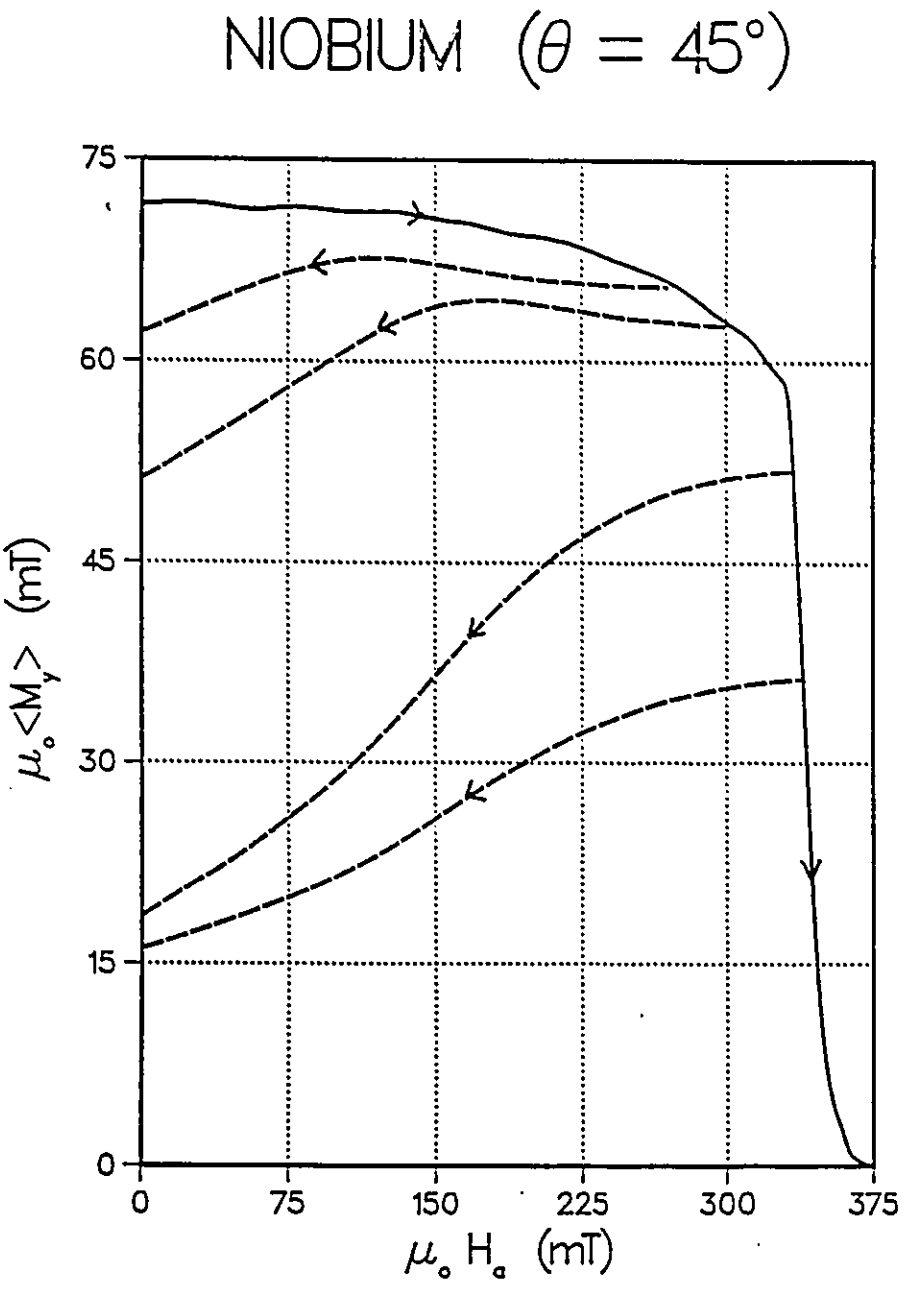

Figure 3.5: Evolution of $< B_y >$ vs H_a after rotation of the trapped flux through 45°. The solid curve is observed as H_a is increased to H_{c2}. The dashed curves are traced upon reducing H_a to 0 when H_a reaches an arbitrary value. This value is indicated by the intersection of the solid and dashed curves. Here $< B_y > \equiv \mu_o < M_y >$ since $\vec{H}_a$ has no component along the y-axis.

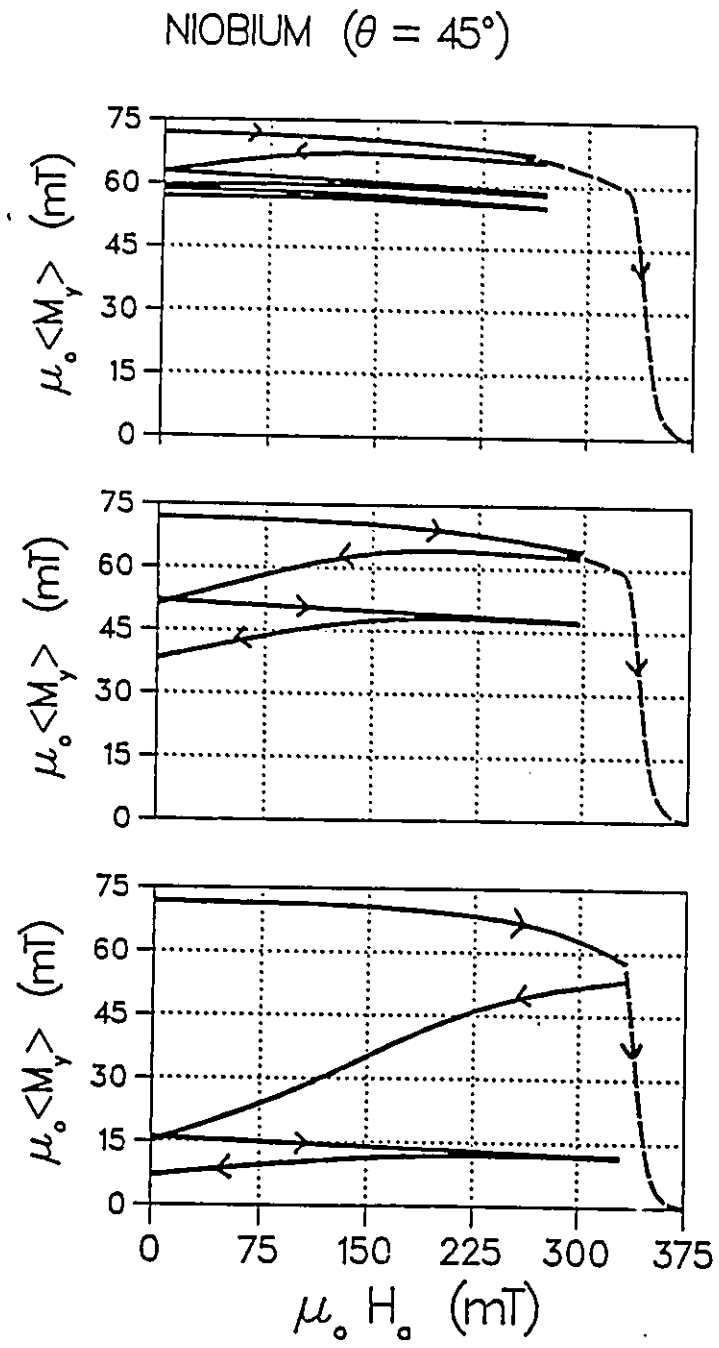

Figure 3.6: Complements the previous figure and shows the effect of successive half cycles of H_a on $< B_y >$. The effect of different amplitudes of the swing of H_a is displayed by the set of figures. The "master" curve obtained when H_a is increased to H_{c2} is reproduced for reference in each case.

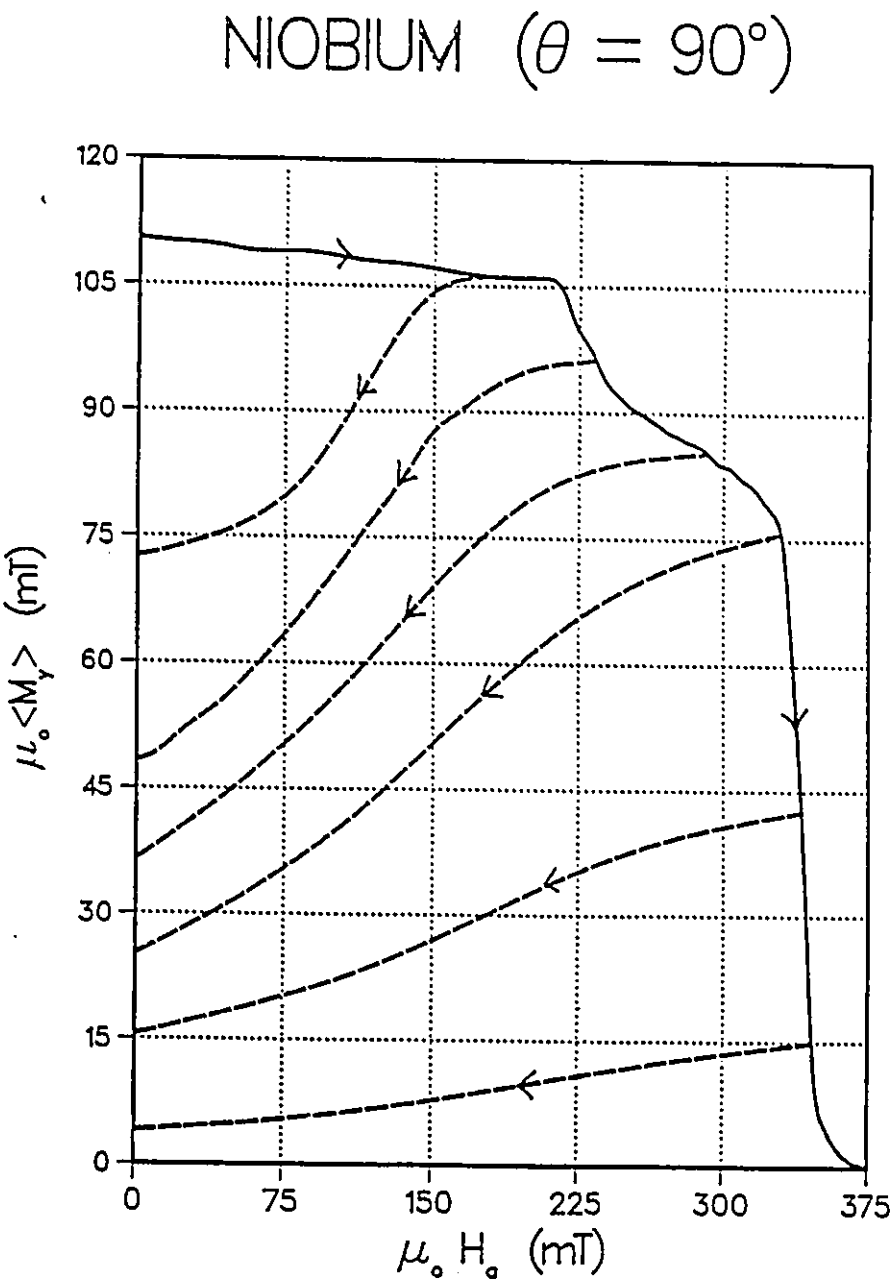

Figure 3.7: Evolution of $< B_y > \equiv \mu_o < M_y >$ vs H_a increasing and decreasing after rotation of the trapped flux through 90°. See figure caption to Fig 3.5 for further details.

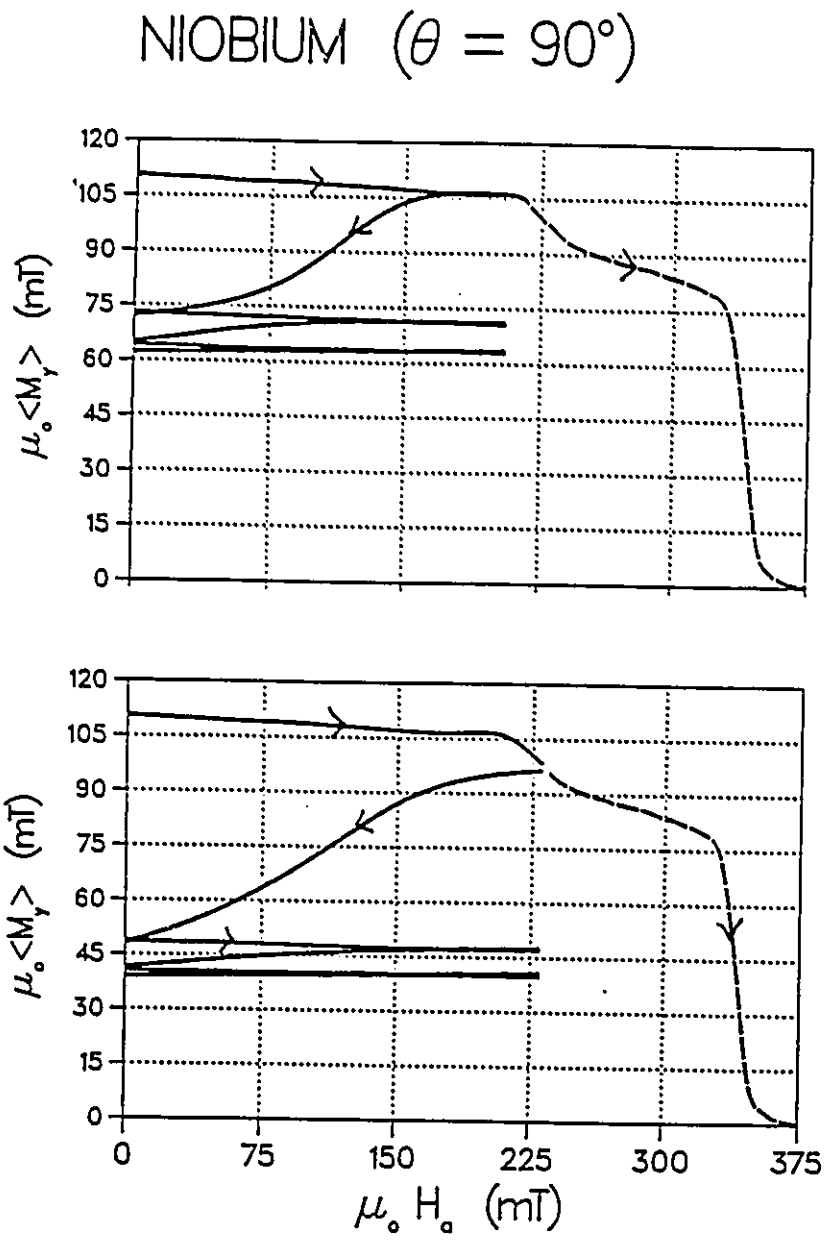

Figure 3.8: Complements the previous figure. See figure caption to Fig 3.6 for further details.

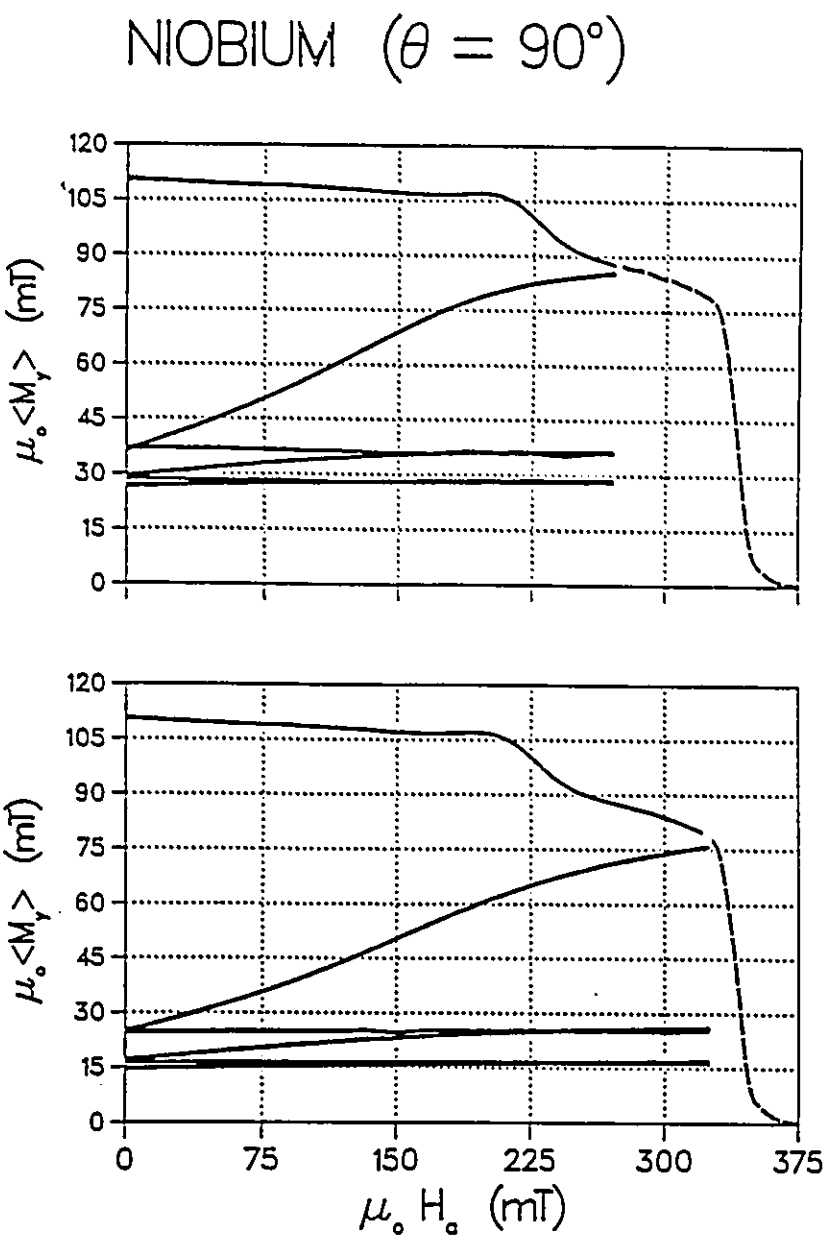

Figure 3.9: Continuation of Fig 3.8.

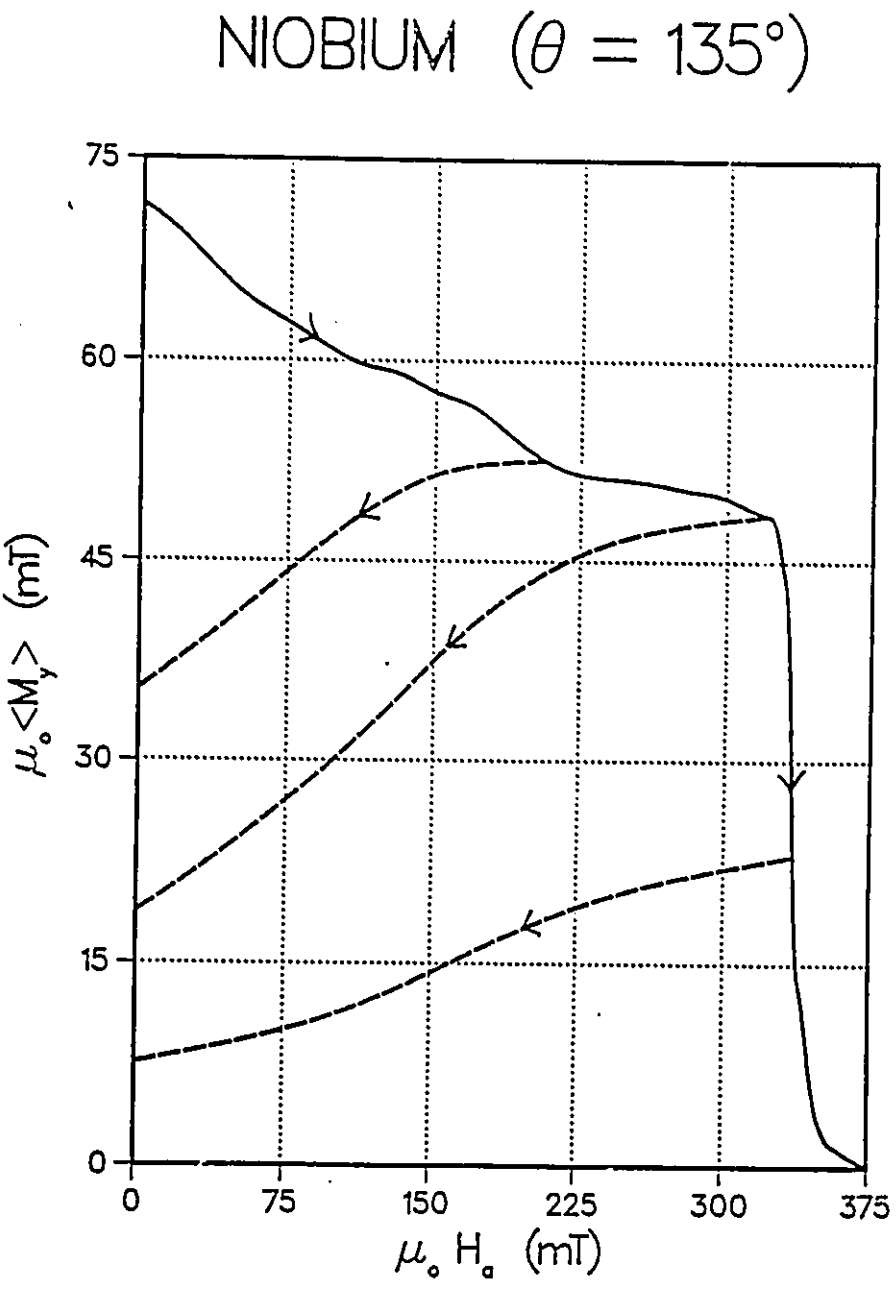

Figure 3.10: Evolution of $< B_y > \equiv \mu_o < M_y >$ vs H_a increasing and decreasing after rotation of the trapped flux through 135°. See figure caption to Fig 3.5 for further details.

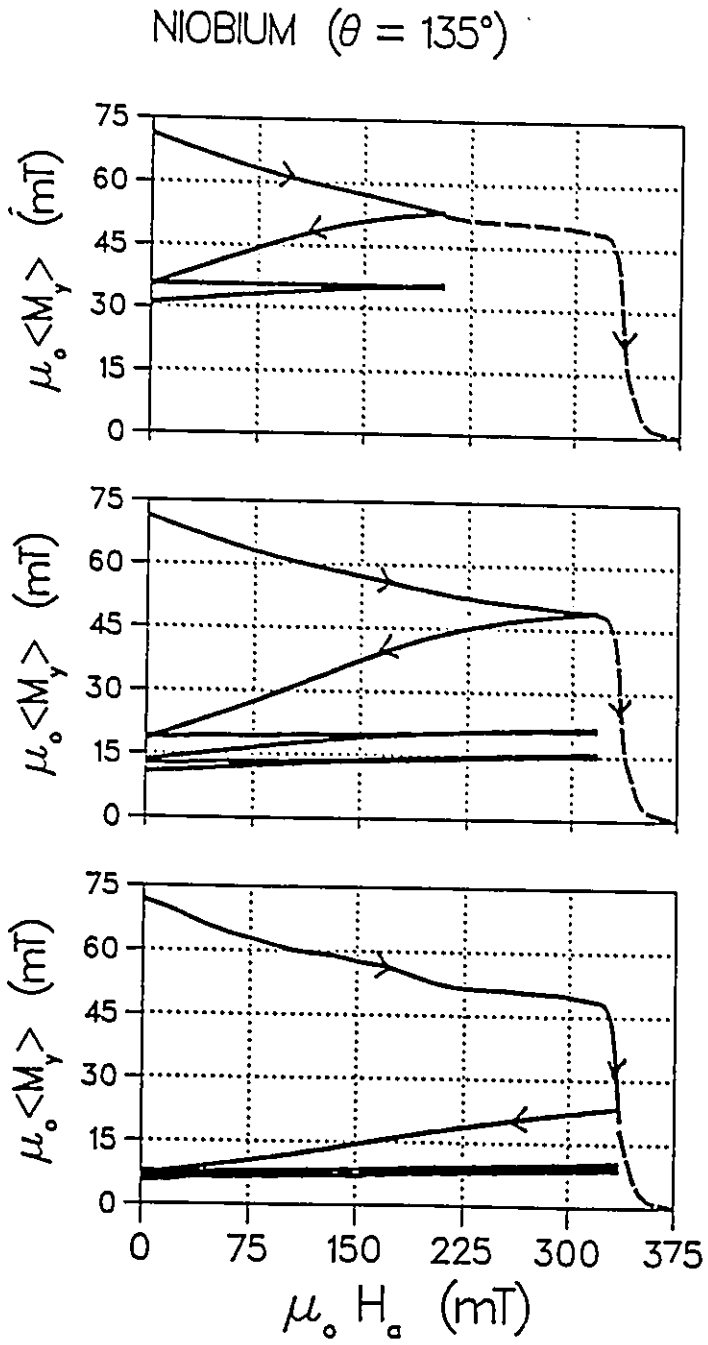

Figure 3.11: Complements the previous figure. See figure caption to Fig 3.6 for further details.

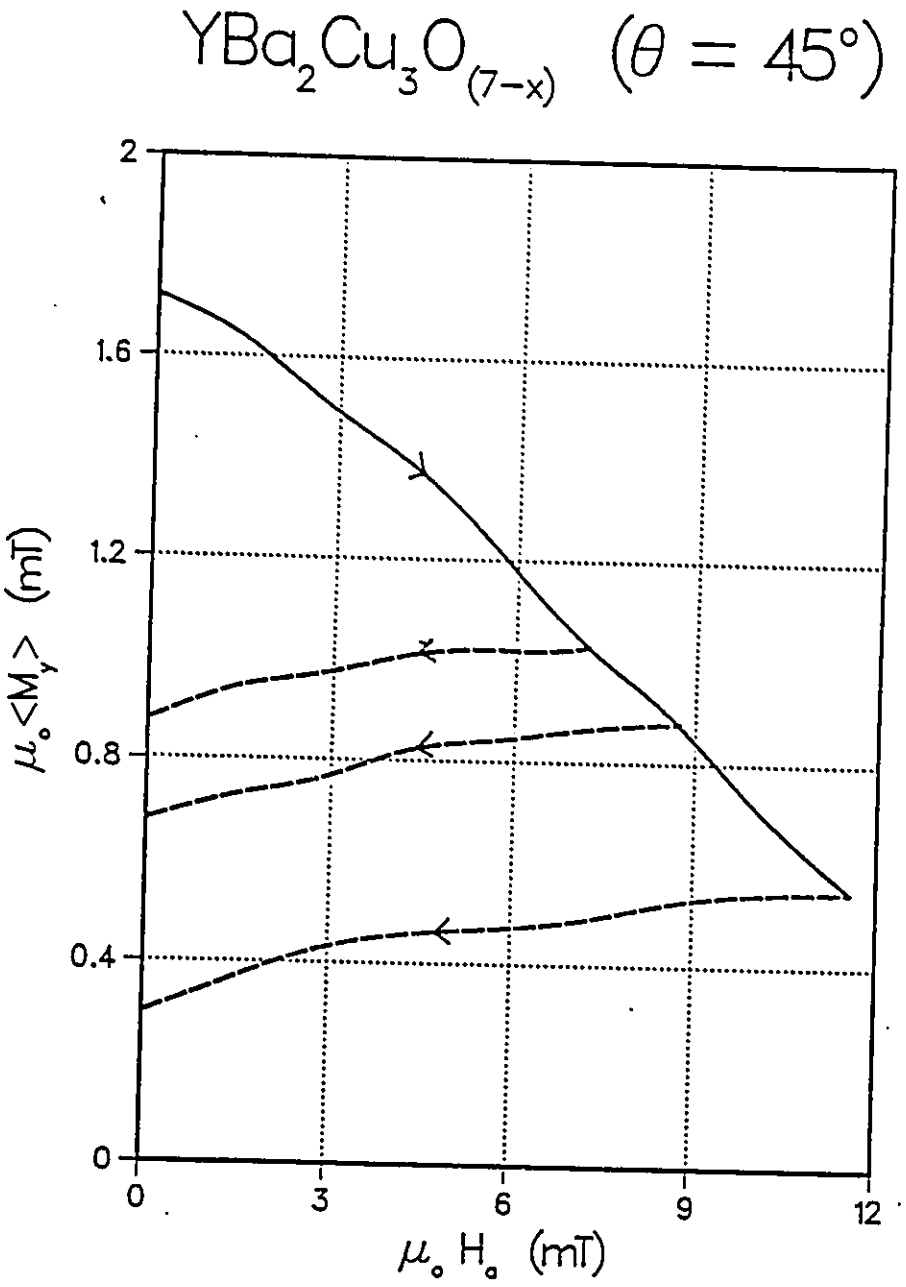

Figure 3.12: Evolution of $< B_y > \equiv \mu_o < M_y >$ vs H_a after rotation of the trapped flux through 45°. See figure caption to Fig 3.5 for further details.

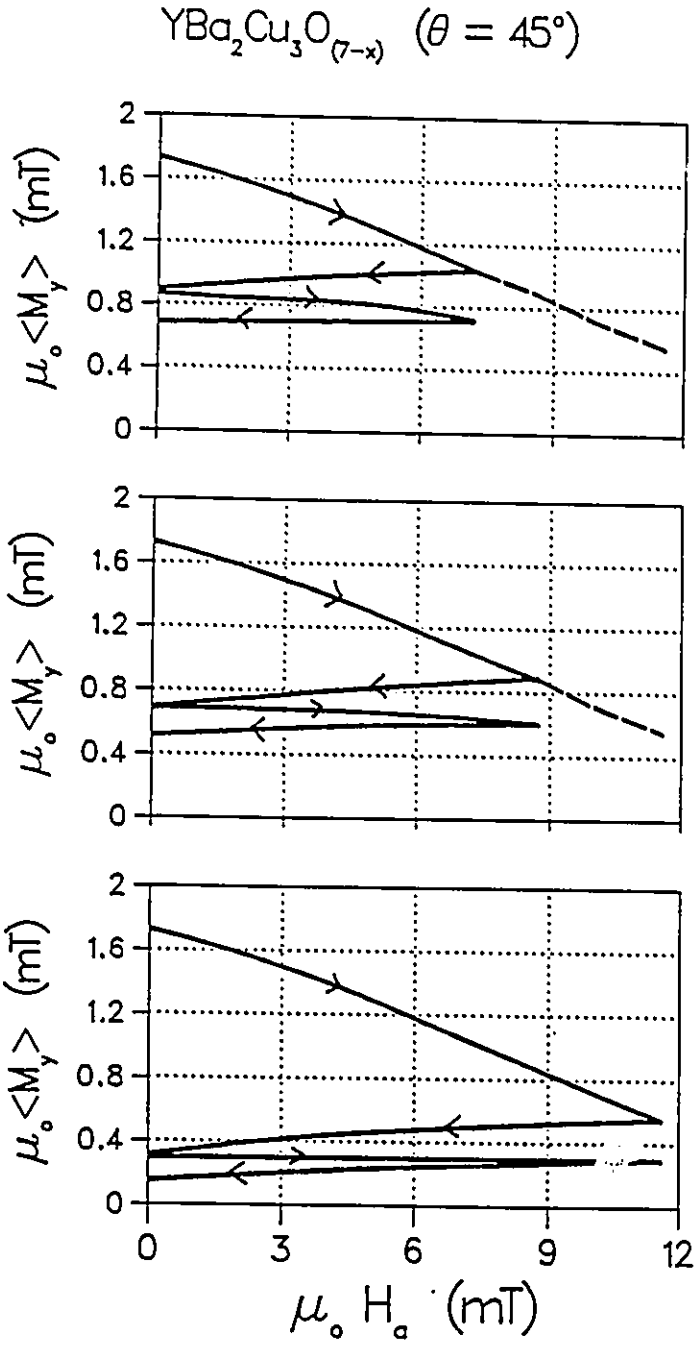

Figure 3.13: Complements previous figure. See caption to Fig 3.6 for further details.

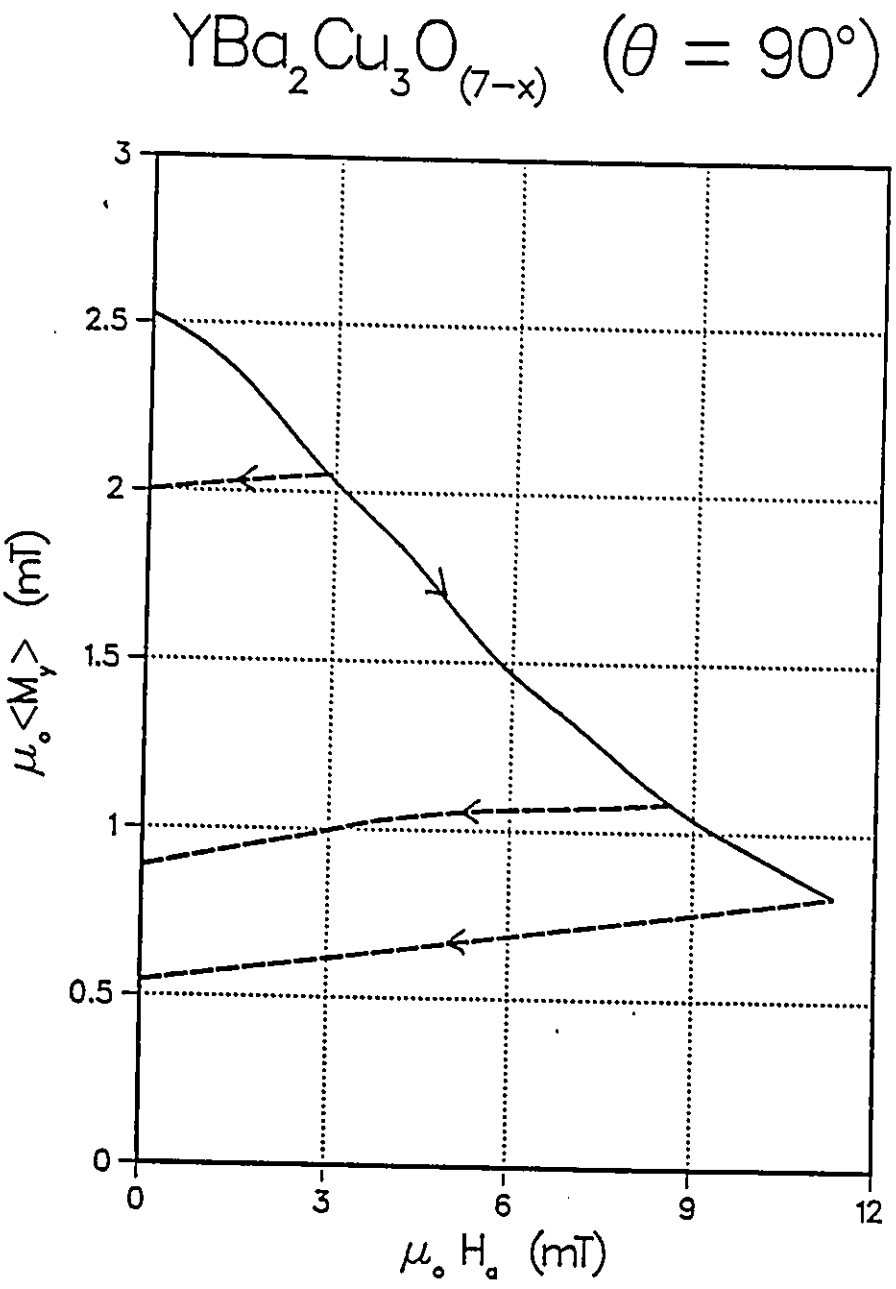

Figure 3.14: Evolution of $< B_y > \equiv \mu_o < M_y >$ vs H_a after rotation of the trapped flux through 90°. See figure caption to Fig 3.5 for further details.

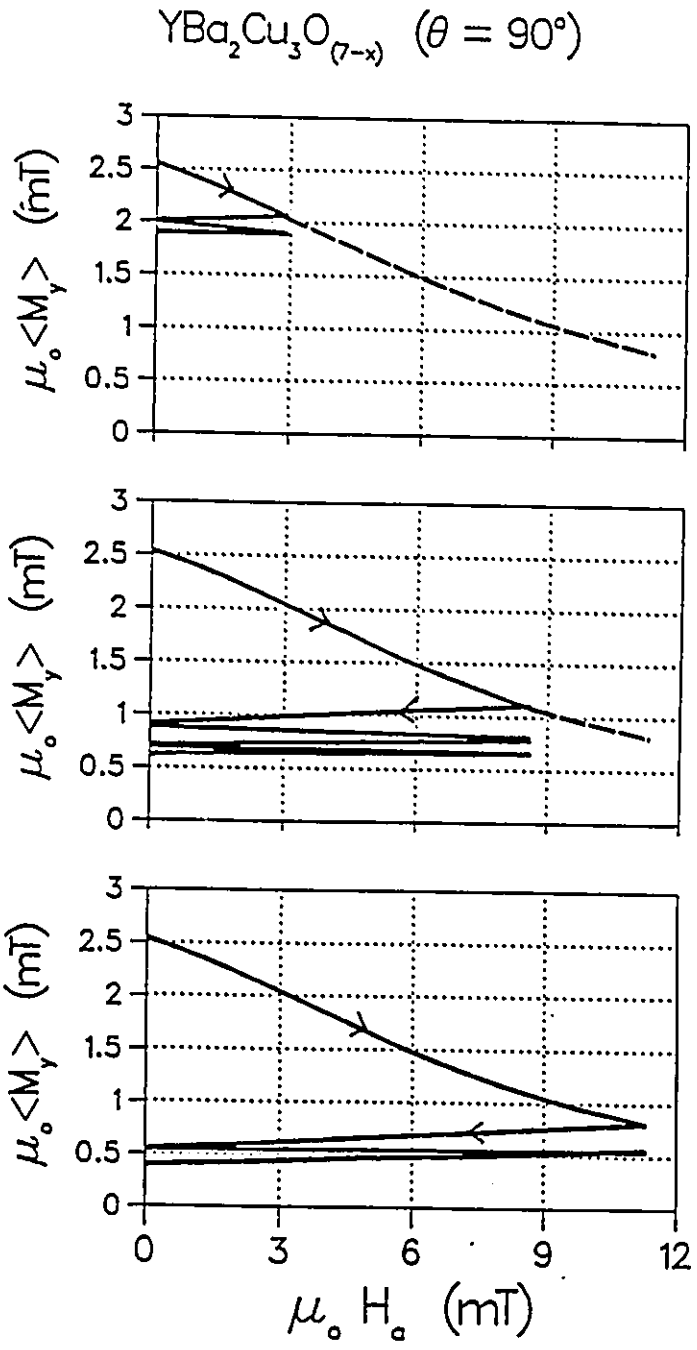

Figure 3.15: Complements previous figure. See caption to Fig 3.6 for further details.

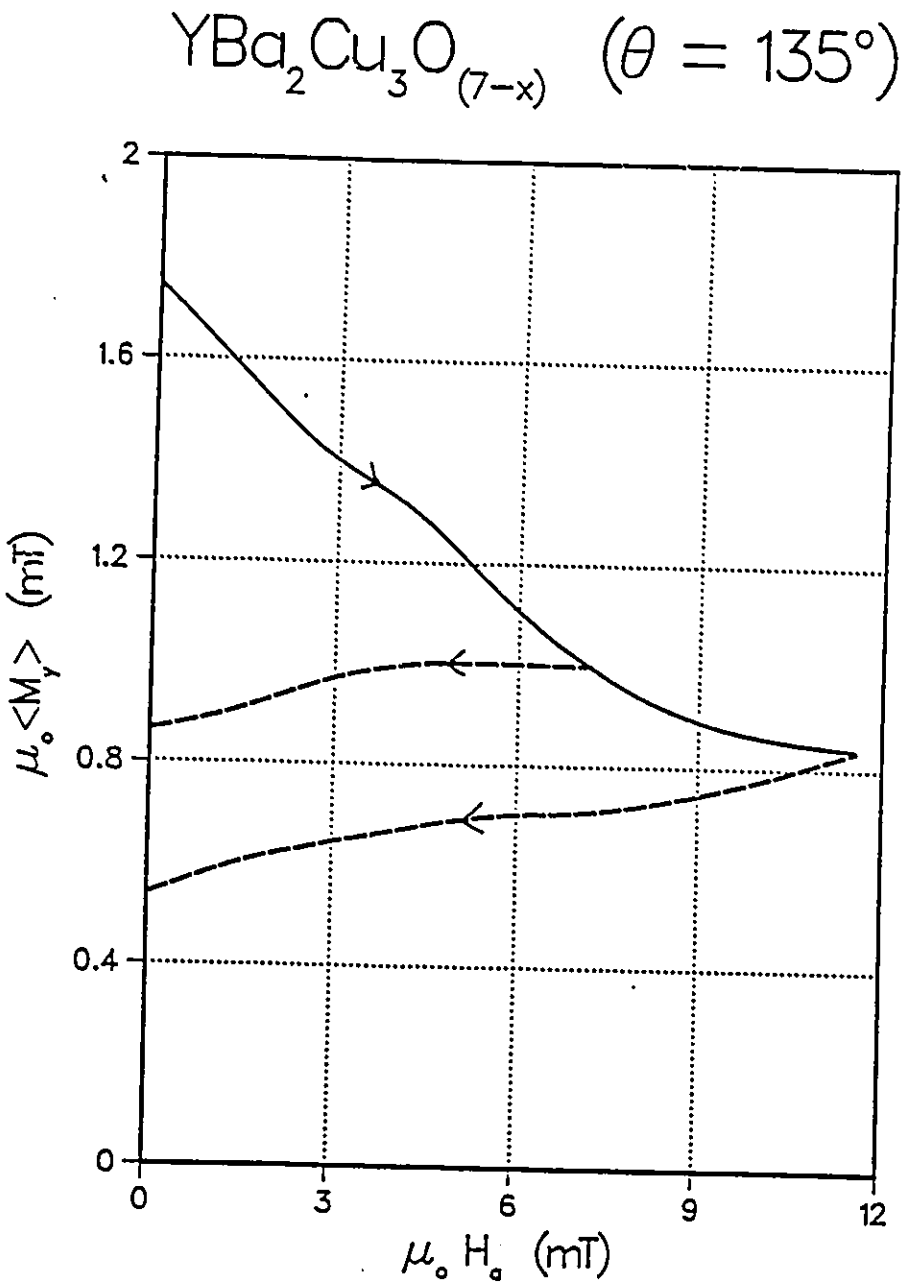

Figure 3.16: Evolution of $< B_y > \equiv \mu_o < M_y >$ vs H_a after rotation of the trapped flux through 135°. See figure caption to Fig 3.5 for further details.

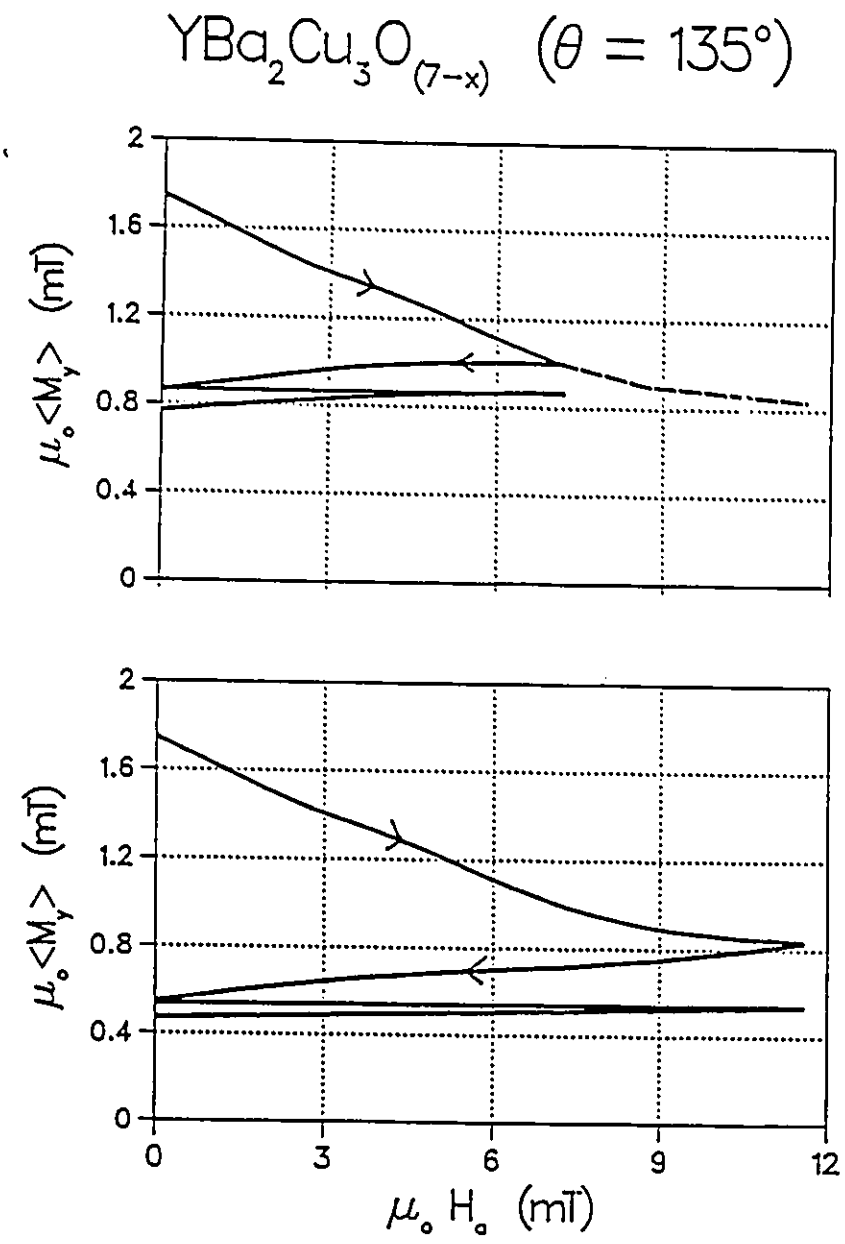

Figure 3.17: Complements previous figure. See caption to Fig 3.6 for further details.

3.4 Comments on the Observations

Because of the fairly large display of curves, we divide this section in two parts. In the first segment, we will comment on the results presented for the Niobium sample and in the second part we will discuss the observations made on the $YBa_2Cu_3O_{7-x}$ specimen.

3.4.1 Evolution of $< B_y >$ vs H_a for Niobium

The evolution of the trapped flux for the Niobium specimen versus H_a increasing and decreasing is displayed in Figs 3.5 through 3.11. We note that $\mu_o < M_y > \equiv < B_y >$ since $\vec{H}_a$ has no component along the y-axis. H_{c2} for this material is readily attained by our superconducting solenoid, hence the behaviour was investigated over the entire range $0 < H_a \leq H_{c2}$. The standard magnetization curves for this specimen indicate $H_{c1} \approx 0.3H_{c2}$ ($\mu_o H_{c1} \approx 0.12$ Tesla), $H_* \approx 0.5H_{c2}$ ($\mu_o H_* \approx 0.18$ T) and $H_{**} \approx 0.6H_{c2}$, ($\mu_o H_{**} \approx 0.21T$).

First we turn our attention to Figs 3.5, 3.7 and 3.10. The solid curves in these three figures allow us to compare the evolution of $< B_y > \equiv \mu_o < M_y >$ as H_a is impressed after a rotation of the trapped flux through 45°, 90° and 135°.

In each case we note that $< B_y >$ is altered, although only slightly in the first two instances, as H_a is raised through the range from 0 to H_{c1} (i.e. 0 to $\approx 0.12\ T$). Indeed with the trapped flux rotated through 135°, the decline of $< B_y >$ over this range is not insignificant. It is well established but not well understood, that trapped flux seems to weaken and even quench the perfect shielding property of

type II superconductors, hence reduce and even suppress H_{c1}. This is attributed to the fact that some of the trapped flux pierces the broad surfaces of the specimen, thereby perturbing and even destroying the diamagnetic (Meissner) current in equilibrium with H_a. At any rate, this feature will lead us to ignore H_{c1} in the analysis of the data.

Another salient feature common to the three figures under scrutiny is the rapid descent of $< M_y >$ near H_{c2}. This is clearly associated with a rapid decline of the magnetic moment near H_{c2} in the standard magnetization curve of this material. This indicates that the depinning critical current density $J_{c\perp}$ exhibits a rapid diminution in this range. This feature will have to be taken into account in our analysis.

We also note the differences in the structure of the "plateau" preceding the abrupt descent. Clearly this plateau is being gouged and tilted as θ is varied from 45° through 90° to 135°. A satisfactory model will have to reproduce such a trend.

Once H_a has been raised from zero to some arbitrary intensity between 0 and H_{c2}, it is of special interest to view the effect on $< B_y >$ caused by its removal. Such a procedure will of course allow flux lines parallel to H_a to exit from the specimen. It is particularly fascinating to observe that a significant fraction of the component of the trapped flux orthogonal to H_a is also thereby released. This can be seen by inspection of the dashed curves in Figs 3.5, 3.7 and 3.10. The magnitude of the release of "orthogonal" flux is particularly evident and dramatic for all ranges of H_a where $\theta = 90°$ and 135° and for H_a having been raised to near H_{c2} when $\theta = 45°$. Again this phenomenon will have to be reproduced and provide a test of a successful model.

The effect of successive sweeps of H_a (periodic half cycles) of fixed amplitude and the role of the magnitude of such a series of swings of H_a on the "orthogonal" flux $< B_y >$, is displayed in the remainder of this group of figures. The major feature which emerges from these measurements is that after the first swing, subsequent sweeps of H_a cause only minor changes in $< B_y >$, i.e. in the spatial average of this component of the magnetic flux configurations although the detailed distributions of the orientation and density of the flux lines may undergo dramatic modifications.

The effect of periodic swings is not examined theoretically in this thesis and remains as a challenge for other researchers.

3.4.2 Evolution of $< B_y >$ vs H_a for $YBa_2Cu_3O_{7-x}$

In this section we display a selection of our observations on the high T_c disk at 77 K. Even at 77 K, the upper critical field for this material is extremely large ($\approx 6T$) and far beyond the range of our copper solenoid immersed in liquid nitrogren. This limit however is relatively unimportant in the present case since most of the trapped flux has been released when $\mu_o H_a$ attains 12 mT as can be seen from a glance at Figs 3.12, 3.14 and 3.16. These three figures compare the behaviour after rotations of the trapped flux through 45°, 90° and 135°. We note that for this specimen, the initial orientation of the trapped flux does not significantly influence the slopes of the curves, whether H_a is increasing or is being removed.

For all three orientations of the trapped flux, as H_a progresses beyond 12 mT,

which corresponds approximately to H_{**} for this specimen, the slope of $< B_y >$ becomes shallower and gradually, the detected signal for $< B_y >$ disappears in the background "noise".

It is clear from comparison of Figs 3.5, 3.7 and 3.10 with Figs 3.12, 3.14 and 3.16 that over the range displayed, i.e. $0 < H_a \leq H_{**}$, the slopes $d < B_y > /dH_a$, (i) are steep as H_a is ascending compared with that observed in the corresponding range for the Nb specimen and (ii) are shallow compared with the corresponding data curves for Nb when H_a is descending. Further it is noted that for the high T_c material, the slopes do not vary significantly with H_a over the range $0 < H_a < H_{**}$.

The remainder of the figures in this group display the effect of periodic cycles of H_a of different amplitudes on the evolution of $< B_y >$. Examination of the figures shows that these half cycles of H_a, gradually perturb $< B_y >$ although not appreciably. This behaviour is identical to that encountered with the Nb specimen.

In our analysis of these observations we have addressed only the phenomena during the first application and removal of H_a. The variety and differences in behaviour exhibited by the Nb and high T_c specimens present a formidable challenge for theoretical description. In the next chapter we outline the framework of the only model in the literature which pertains to these phenomena and proceed in the following chapter to apply this model to the specific circumstances of our experiment.

Chapter 4. TILTED FLUX LINES (THEORETICAL I)

4.1 Introduction

To gain a better understanding of the observations reported in the previous chapter, it is useful to first consider the interaction of tilted flux lines. In this discussion, we choose to focus our attention on the flux lines instead of the induced persistent currents since it is easier to visualize the evolution of the former than to follow the sequence of patterns of the latter. Using Maxwell-Ampere's equation, $\nabla \times \vec{B} = \mu_o \vec{J}$, an understanding of the induced persistent currents can readily be attained once a detailed picture of the magnetic flux configurations has been established.

Clem's phenomenological model is also presented. This model is exploited computationally in detail in the next chapter. Computer simulations of the phenomena were pursued based on this model. The theoretical magnetization curves obtained are presented and compared with those observed experimentally (presented in chapter 3).The similarities and differences will be discussed.

4.2 Theoretical Background

4.2.1 Flux Flow and Flux Pinning Mechanisms in Hard Superconductors

We begin this analysis by qualitatively examining the mechanism responsible for flux flow motion inside hard superconductors i.e. magnetically hysteretic (irreversible) type II superconductors. To simplify the discussion we choose a hard superconductor in the form of an infinite slab. This geometry enables us to concentrate on the physics of flux motion and eliminate any magnetic effects caused by geometric features.

Let the superconducting slab initially be in a virgin state. Virgin is defined as the state of the sample when it has become superconducting by cooling in the absence of a magnetic field. As an external magnetic field is applied parallel to the surfaces of the specimen, persistent currents are induced at the surface of the superconductor such as to prevent flux entry. For simplicity we focus on only one half of the slab and its adjacent surface. When H_a is increased just above H_{c1}, magnetic flux is seen to slowly enter the slab near the surface. This flux can be visualized as existing in the form of discrete flux lines. Each flux line is an infinitely long cylindrical tube with a non superconductive core. Persistent currents circulate around each core . Numerous experiments have now confirmed in some detail this picture first proposed by Abrikosov [1].

These fluxons or vortices, as they are called, are formed at the surface of

the slab. As H_a is continuously increased, more vortices nucleate at the surface thereby increasing the local flux density. Adjacent parallel fluxons are known to repel each other through a Lorentz like force. A net force of this nature, directed toward the center of the slab, acts on all the vortices and presses them further inward. As the vortices are driven away from the surface by the Lorentz force they encounter imperfections and impurities in the lattice. These act as pinning sites for the vortices. The strength of the pinning force depends on several factors, such as the type, size and number of imperfections and dislocations, the strength of the magnetic field and also the ambient temperature [9],[21],[20].

The effect of temperature on pinning strength can be understood in terms of thermal vibration of the lattice. The higher the temperature, the stronger the lattice vibrations. It is therefore expected that at high enough temperature, vibrations of the lattice may be strong enough to 'shake loose' the vortices. Very large flux creep attributed to thermal activation has been observed in some high T_c superconductors and is of primary concern at the moment [23],[28],[27].

4.2.2 The Critical State Model

If the force exerted on the vortices by the pinning sites is strong enough to counter the driving Lorentz force, flux flow is stopped. This situation is characterized as the critical state. To push the lines further inward, the intensity of the external field must be raised. In doing so, additional fluxons nucleate at the surface thereby increasing the local flux density. In turn this augments the strength of the Lorentz force driving the vortices further inward. The critical state concept, proposed

initially by Bean [3] and further investigated by Anderson [2], stipulates that flux line displacement will take place when the equilibrium condition $\vec{F}_L + \vec{F}_p = 0$ is exceeded. Kim et al, [18],[19], showed that the above condition is satisfied when the current density reaches a critical value which is referred to as the critical current density, J_c.

As the rise of H_a progresses, one can readily picture a profile of the flux density advancing into the bulk of the slab from the surface (as shown in Fig 3.1(a)).

For slow changes of H_a, the profiles or configurations of the flux density evolve through a succession of quasi-static near equilibrium critical states. Since this is the situation which applies in our work we will confine our discussion to these circumstances. We note simply that under rapid changes of H_a, non equilibrium or dynamic critical states will arise where viscous retarding forces proportional to the velocity of the flux lines, as well as the pinning forces, come into play.

4.3 The Clem Phenomenological Model

As mentioned previously, our experimental work consisted in monitoring the evolution of the magnetization, both parallel and perpendicular to an applied field as new vortices were caused to nucleate at the surface of a disk and encroach on tilted sheets of flux lines previously trapped inside the specimen. The data presented in chapter 3 provide some insight into the general patterns of the persistent currents.

The situation we confront in our work is somewhat more complex than that encountered in the simple case discussed in the previous section where the magnetic field lines were all aligned parallel to each other. Therefore, it becomes necessary

to extend the critical state model to encompass situations where the direction of the flux lines varies with position hence are not parallel to one another.

Clem and his collaborators [11], [24], [13] have developed such a model and we present some of its main features in this section. An important initial step in the development of this model is to establish appropriate relations between the components of the critical current density and those of the flux density. First, the coordinates of the laboratory frame of reference are defined as follows. Let the z-axis lie along the externally applied field H_a which is directed parallel to the surfaces of the specimen. The x-axis is perpendicular to the broad surfaces of the disk, hence along the thickness of the sample. The y-axis also parallel to the surfaces, is perpendicular to H_a. Consequently, neglecting edge effects, the sheets of flux lines permeating the disk specimen are directed parallel to its flat surfaces and lie along the y-z plane. Their density and direction, however, can vary with depth, i.e. distance from the surfaces, hence versus x.

Writing Maxwell's equation,

$$\nabla \times \vec{B} = \mu_0 \vec{J} \tag{4.1}$$

for infinite slab geometry and our choice of coordinates leads to:

$$-\frac{dB_z}{dx} = \mu_o J_y \tag{4.2}$$

$$\frac{dB_y}{dx} = \mu_o J_z \tag{4.3}$$

From Fig 4.1, the components of $\vec{B}$ in the laboratory reference frame are:

$$B_z = B \sin\theta \tag{4.4}$$

$$B_y = B \cos\theta \tag{4.5}$$

Differentiating the above two equations with respect to x yields:

$$\frac{dB_z}{dx} = \frac{dB}{dx} \sin\theta + B \cos\theta \frac{d\theta}{dx} \tag{4.6}$$

$$\frac{dB_y}{dx} = \frac{dB}{dx} \cos\theta - B \sin\theta \frac{d\theta}{dx} \tag{4.7}$$

Substituting these last two expressions in 4.2 and 4.3 yields:

$$-\frac{dB}{dx} \sin\theta - B \cos\theta \frac{d\theta}{dx} = \mu_o J_y \tag{4.8}$$

$$\frac{dB}{dx} \cos\theta - B \sin\theta \frac{d\theta}{dx} = \mu_o J_z \tag{4.9}$$

For reasons which will become obvious later, we choose to decompose the current density vector $\vec{J}$ into its parallel and perpendicular components to the local flux density rather than its components along y and z (i.e. the laboratory frame of reference). The realization that Maxwell's equations should be expressed in the local coordinates defined by $\vec{B}$ constitutes a crucial step in the theory developed by Clem.

Referring to figure 4.2, the transformations relating the coordinates of the laboratory reference frame to those of the reference frame defined by $\vec{B}$ are :

$$\hat{y} = \cos\theta\ \hat{\alpha}\ + \sin\theta\ \hat{\beta} \tag{4.10}$$

$$\hat{z} = \sin\theta\ \hat{\alpha}\ - \cos\theta\ \hat{\beta} \tag{4.11}$$

Where :

$\hat{y}$ is a unit vector along the y-axis.

$\hat{z}$ is a unit vector along the z-axis.

$\hat{\alpha}$ is a unit vector parallel to $\vec{B}$.

$\hat{\beta}$ is a unit vector perpendicular to $\vec{B}$.

Applying these transformations to the y and z components of the current density yields :

$$J_y = J_{\|}\ \cos\theta + J_{\perp}\ \sin\theta \tag{4.12}$$

$$J_z = J_{\|}\ \sin\theta - J_{\perp}\ \cos\theta \tag{4.13}$$

Finally, introducing 4.12 in 4.8 and comparing terms on both sides of the equation with common factors (sines and cosines), we get the following two important relations:

$$\mu_o\ J_{\|} = -B\ \frac{d\theta}{dx} \tag{4.14}$$

$$\mu_o\ J_{\perp} = -\frac{dB}{dx} \tag{4.15}$$

These equations can also be obtained through similar algebraic manipulations of equations 4.9 and 4.13.

We stress that equations 4.14 and 4.15 are simply a formulation of Maxwell's equation in the framework of infinite slab geometry where $\vec{B}$ and $\vec{J}$ are directed in the y-z plane and vary spatially with the coordinate x. The crucial feature is that $\vec{J}$ is projected with respect to $\vec{B}$ instead of with respect to the laboratory or specimen coordinates. The spatial variation of $\vec{B}$ however will be scrutinized in the laboratory (specimen) coordinates.

It is now stipulated that in the steady state, $J_{\parallel}$ and $J_{\perp}$ cannot exceed critical values denoted $J_{c\parallel}$ and $J_{c\perp}$.

Various approximations for the dependence of $J_{c\parallel}$ and $J_{c\perp}$ on the magnetic flux density have been exploited in the literature. An accepted general form when $B \ll B_{c2}$ can be written,

$$J_{c\parallel} = \frac{k}{B^n} \tag{4.16}$$

$$J_{c\perp} = \frac{\alpha}{B^n} \tag{4.17}$$

Where:

α is a constant characterizing the pinning strength of the material.

k is a constant related to the flux cutting phenomena and will be discussed in the next section.

n defines the degree of dependence of both components of J on B.

For the Bean approximation $n = 0$.

For the Yasukochi approximation $n = \frac{1}{2}$.

For the Kim approximation $n = 1$.

α and k are temperature dependent parameters.

Another important aspect which needs to be considered in the analysis is the generation of an electric field when $\vec{B}$ changes magnitude and/or direction. This is accomplished by turning to the Maxwell-Faraday equation,

$$\nabla \times \vec{E} = -\frac{\partial \vec{B}}{\partial t} \tag{4.18}$$

For planar geometry and our choice of coordinates this reads,

$$\frac{\partial E_y}{\partial x} = -\frac{\partial B_z}{\partial t} \tag{4.19}$$

$$\frac{\partial E_z}{\partial x} = \frac{\partial B_y}{\partial t} \tag{4.20}$$

Proceeding with the vector $\vec{E}$ in the same manner as with the vector $\vec{J}$, the components of the electric field in the reference frame defined by $\vec{B}$ are,

$$\frac{\partial E_{\parallel}}{\partial x} = -B\,\frac{\partial \theta}{\partial t} - E_{\perp}\frac{\partial \theta}{\partial x} \tag{4.21}$$

$$\frac{\partial E_{\perp}}{\partial x} = E_{\parallel}\,\frac{\partial \theta}{\partial x} - \frac{\partial B}{\partial t} \tag{4.22}$$

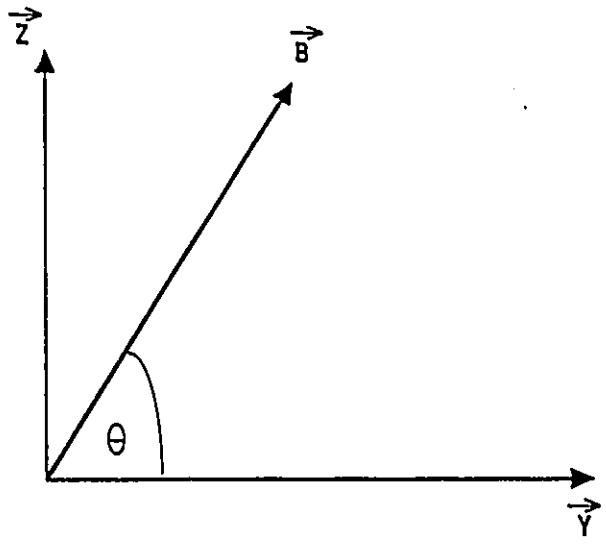

Figure 4.1: $\vec{B}$ in the laboratory frame of reference.

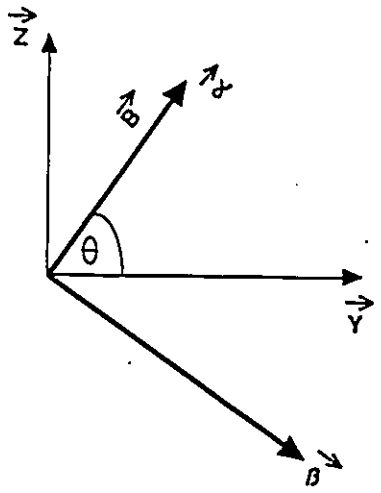

Figure 4.2: Relation between the laboratory frame of reference and the reference frame defined by $\vec{B}$.

By symmetry, the electric field must vanish at the midplane of the disk. This boundary condition stated mathematically reads :

$$E_{\|}(x = X) = 0 \qquad \text{and} \qquad E_{\perp}(x = X) = 0$$

For a dissipative system, classical physics requires that $\vec{E}$ and $\vec{J}$ subtend an angle less than 90°. In using the reference frame defined by $\vec{B}$, Clem placed a more stringent requirement, that is, wherever there is an electric field,

$$E_{\|} \cdot J_{\|} > 0 \qquad \text{and} \qquad E_{\perp} \cdot J_{\perp} > 0$$

In other words, flux line depinning and flux line cutting both dissipate energy. As a consequence of the above, this phenomenological model envisages three types of active regions.

- **Pure Flux Transport Zones (T zones), where :**

$$J_{\perp} \geq J_{c\perp}, \qquad 0 \leq J_{\|} \leq J_{c\|}, \qquad E_{\perp} \cdot J_{\perp} > 0 \qquad \text{and} \qquad E_{\|} = 0.$$

  The above conditions clarify the type of activity expected in these regions. Since $J_{\perp}$ is greater than $J_{c\perp}$, flux lines experience depinning and are allowed to move in this regime. This results in a compression of flux lines in the case of an increasing external field and a decompression of the vortices if the external field is decreasing. A current density $J_{\|}$ can exist in this type of zone but must be less than the critical current density, $J_{c\|}$, so that flux cutting is prevented.

- **Pure Flux Cutting Zones (C zones), where :**

$$J_{\parallel} \geq J_{c\parallel}, \qquad 0 \leq J_{\perp} \leq J_{c\perp}, \qquad E_{\parallel} \cdot J_{\parallel} > 0 \qquad \text{and} \qquad E_{\perp} = 0.$$

In a pure flux cutting zone, the flux lines, on a macroscopic scale, remain pinned at their respective sites since the Lorentz force is not strong enough to free the trapped vortices. Since $J_{\parallel}$ is greater than $J_{c\parallel}$, flux cutting occurs between adjacent planes of vortices. Through this process, magnetic flux is consumed thereby reducing the local flux density and producing subcritical gradients of magnetic flux density. The mechanism through which flux cutting occurs is presented in the next section. Suffice it to say for now that this is an important and novel element in the perspective on these materials and constitutes a radical departure from the previously accepted framework. Prior to the work of Clem, it was generally believed that $J_{\perp}$ had to equal or exceed $J_{c\perp}$ whenever the flux configuration was undergoing any changes.

- **Flux Cutting and Flux Transport Zones (CT zones), where :**

$$J_{\parallel} \geq J_{c\parallel}, \qquad J_{\perp} \geq J_{c\perp}, \qquad E_{\perp} \cdot J_{\perp} > 0\ , \qquad \text{and} \qquad E_{\parallel} \cdot J_{\parallel} > 0$$

In this type of region both processes occur simultaneously. This type of zone had been postulated by LeBlanc and his collaborators and constituted a pillar of the empirical double critical state model which they proposed and explored [5], [17], [22].

For completeness, inactive or inert regions can exist where neither flux migration nor flux cutting occurs. In these zones, persistent currents from previous activity may be present but these remain constant independent of any activity occurring in adjacent regions. Thus here :

$$0 < J_{\perp} < J_{c\perp}, \qquad 0 < J_{\parallel} < J_{c\parallel}, \qquad E_{\perp} = 0 \qquad \text{and} \qquad E_{\parallel} = 0$$

4.4 Flux Cutting Mechanism

We now describe the mechanism responsible for flux line cutting and the attendant consumption of magnetic flux inside hard superconductors. The reader is referred to figure 4.3 which outlines the sequence of events developed in the process of flux cutting.

We start this analysis with an infinite slab permeated with parallel sheets of flux lines. The process of flux cutting can be best described if we consider small incremental rotation of the slab while it is bathing in a uniform magnetic field $\vec{H}_a$ which is kept constant both in direction and magnitude. Again we focus on one surface only. As the slab is slowly rotated, the laws of electromagnetic induction and the continuity of $\vec{B}$ and $\vec{H}$ require that a persistent current appears along the surface with a component parallel to the sheet of flux lines. Of special interest is the sheet of flux lines adjacent to the surface and initially parallel to $\vec{H}_a$.

Eventually, at some critical angle θ_c, hence at a critical current density $J_{c\parallel}$, a new sheet of flux lines of density $B = \mu_o H_a$, will nucleate at the surface of the slab. The new and the 'old' sheet of flux lines are sketched side by side in figure

4.3(b). The new sheet should be visualized as existing a distance Δx above the old one. The former is aligned along $\vec{H}_a$, and the angle subtended by the two sheets is θ_c.

Brandt et al [8], Clem et al [12],[13] have shown that at a critical angle θ_c, the mutual repulsion between parallel sheets of flux lines has vanished. These sheets now experience an attractive interaction which is illustrated in Fig 4.3(c). The two sheets move towards each other under the influence of their mutual attraction, making contact at points of intersection. At these points, the flux lines temporarily fuse and form doubly quantized regions (see Fig 4.3(d)). The resulting regions are energetically expensive and this state of affairs cannot persist. Consequently the union breaks up with a segment from the new sheet now attached to a segment from the old sheet as shown schematically in Fig 4.3(e). This process where two lattices of flux lines intersect and cross join is called flux line cutting, or vortex reconnection.

The immediate result of this process is a dense sheet of zig zag flux lines as depicted in Fig 4.3(f). This zig zag configuration is energetically unfavorable and the patterns straightens out to reduce the line tension energy. The ensuing densely packed sheet of lines shown in Fig 4.3(g), separates into two adjacent sheets due to mutual repulsion. These occupy the same volume initially taken up by the two sheets in figure 4.3(b). These sheets are displayed again side by side in figure 4.3 (h), but in three dimensions, one should be visualized as adjacent to the surface and the other existing deeper inside the material.

It is important to note that D_f, the final separation between the flux lines in the resulting two sheets is larger than the original separation D_i, although the

total number of flux lines is conserved. The situation just described leads to :

$$D_f = \frac{D_i}{\cos(\theta/2)} \tag{4.23}$$

Now the sheet of flux lines closer to the surface is oriented at an angle $\theta = \theta_c/2$ with respect to $\vec{H}_a$. Thus $J_{||} < J_{c||}$, and mutual repulsion expels this sheet from the slab. The magnetic flux density $B = B_a$ existing initially has been reduced by the sequence of events just described, to $B_a \cos(\theta/2)$ along the surface. The sheet of flux lines which remains adjacent to the surface also subtends an angle $\theta = \theta_c/2$ with respect to $\vec{H}_a$, but exists in equilibrium since it also subtends an angle $\theta_c/2$ with respect to the lattice of flux lines in the interior of the disk. As a consequence, the repulsive force which they exert is diminished.

After a subsequent incremental rotation $\Delta\theta = \theta_c/2$, the process just described will repeat. Further, the process will incrementally propagate inwards since after the second full flux cutting sequence, the next nearest neighbour sheet of flux lines subtends an angle $\theta = \theta_c/2$ relative to that existing along the surface. A 'valley 'will thus be gouged into the lattice of flux lines by the process of flux line cutting.

According to Clem et al, flux cutting consumes magnetic flux but conserves the total number of flux lines. The straightening or shortening of the flux lines (see Fig 4.3(f)) is the mechanism responsible for this disappearance of magnetic flux. In another perspective one can visualize that the transverse components of the flux lines have undergone mutual annihilation as the configuration evolved from that depicted in Fig 4.3(d) to that depicted in 4.3(g).

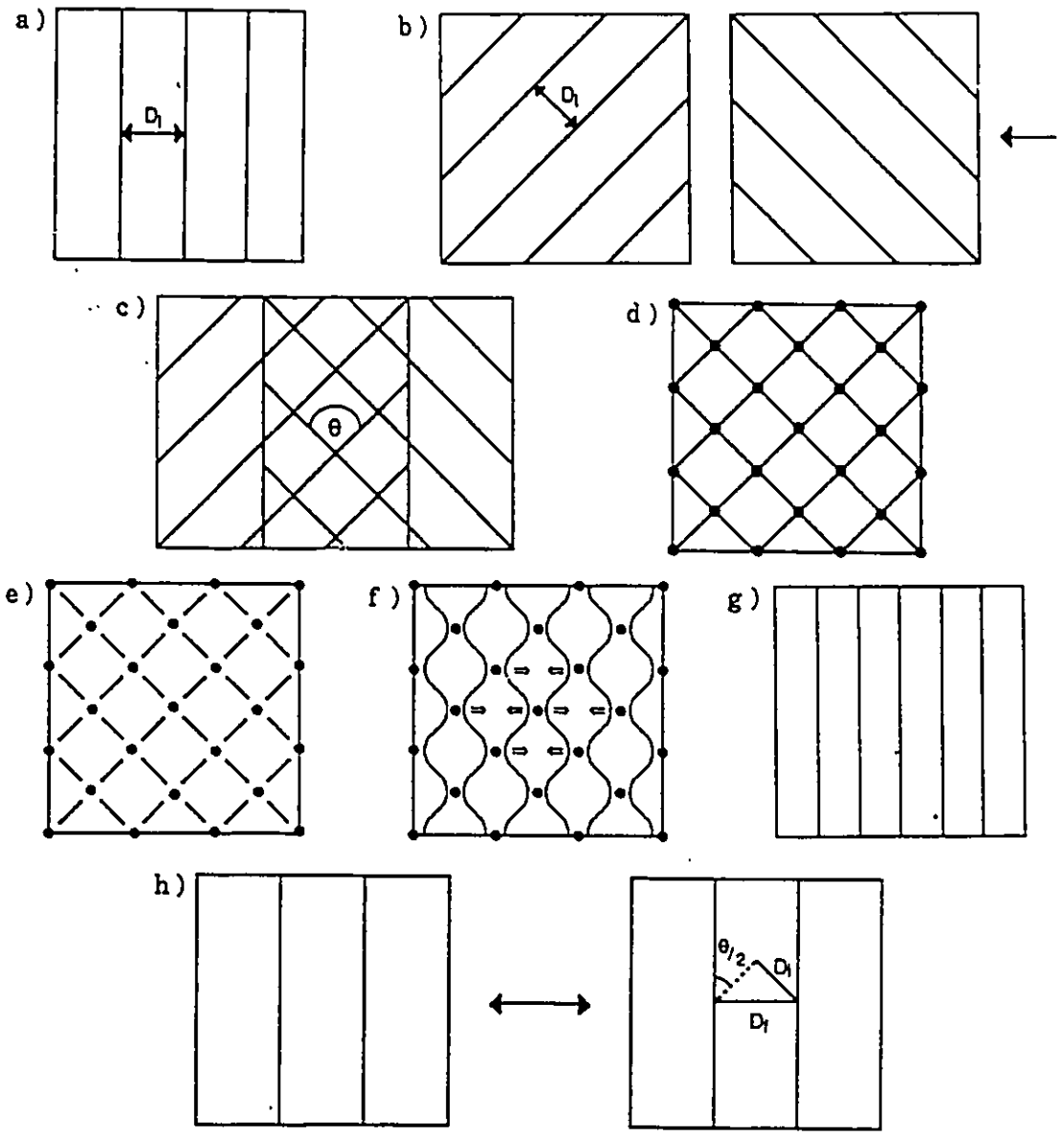

Figure 4.3: Flux line cutting mechanism.

Chapter 5. TILTED FLUX LINES (THEORETICAL II)

5.1 Introduction

Clem's model will now be applied to the specific situation studied in this thesis. We stress once again that our initial configuration consists of a lattice of unidirectional remanent flux trapped in a disk. Sheets of parallel flux lines at a different orientation relative to the remanent flux are then forced to penetrate the specimen and interact with the previously trapped flux.

To fix ideas, let the angle between the incoming flux and the previously trapped flux be 90°. Due to physical constraints, no discontinuities in the magnitude and direction of $\vec{B}$ can occur. Therefore, the variation in the flux density resulting from the interaction of the sheets of vortices must be smooth both in magnitude and direction throughout the disk. This can be schematically represented by a 'snow-fence picture' as depicted in figure 5.1. A display of the evolution of the sequences of the configurations of the lattices of the flux lines as a function of time is shown in fig 5.2.

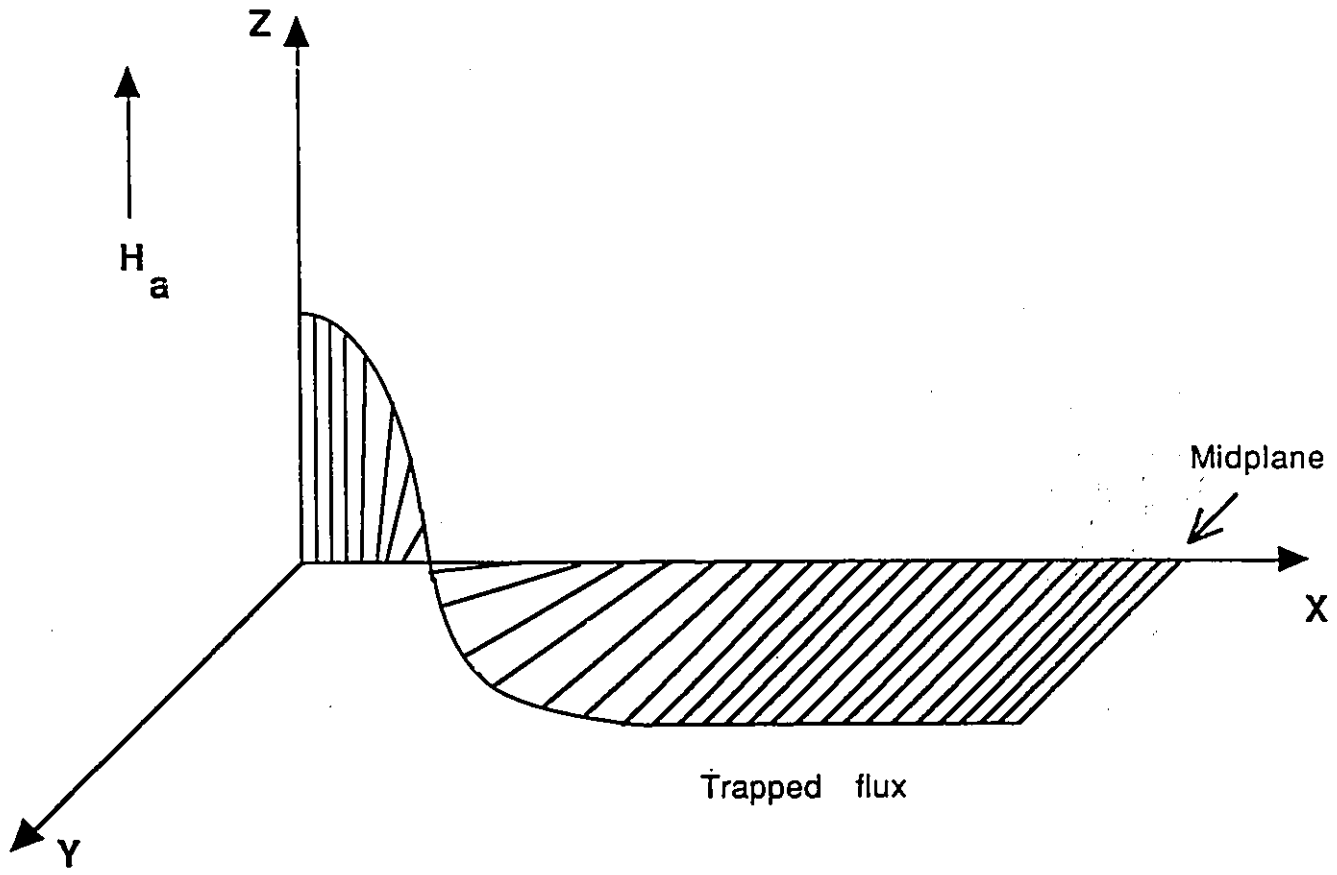

Figure 5.1: Three dimensional display of tilted flux lines in a hard superconductor. Flux is entering from the left and "deforming" the configuration of horizontal trapped flux.

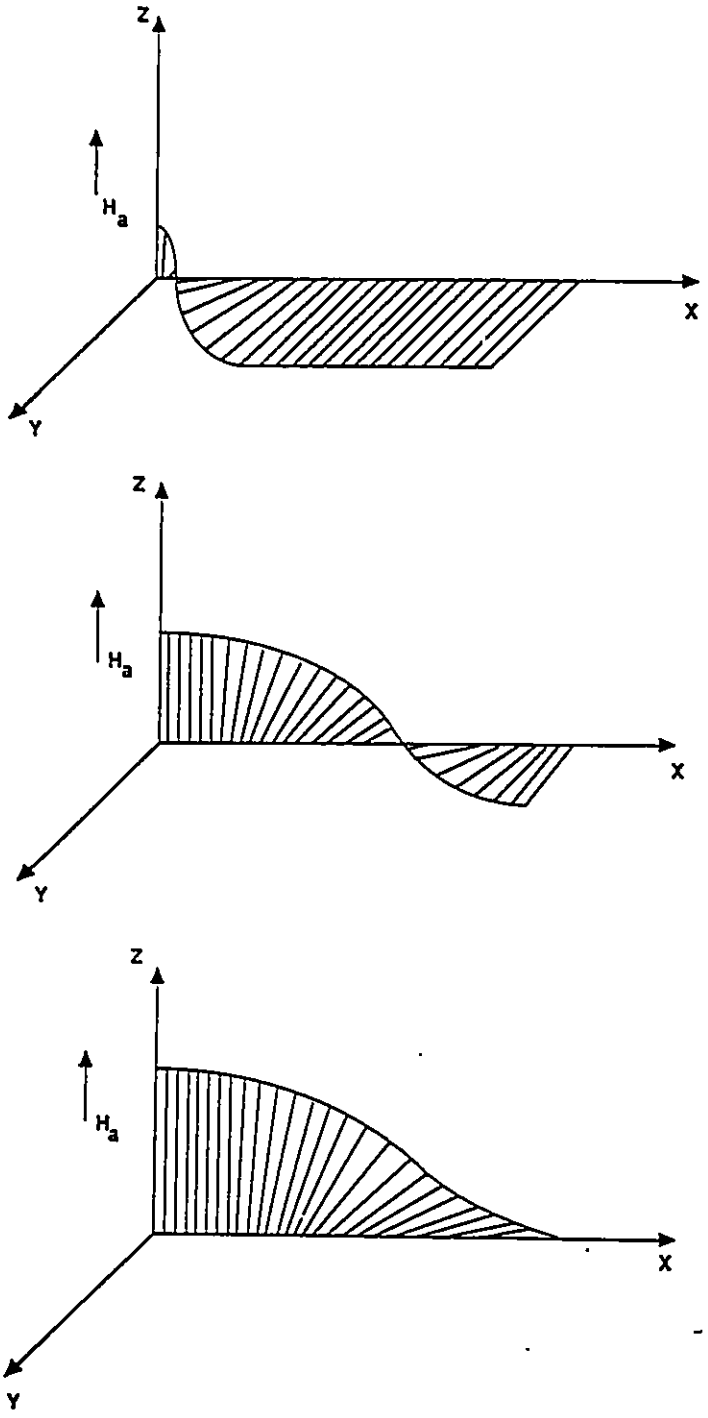

Figure 5.2: Time sequence of snow-fence picture as H_a is incremented.

Alternatively, the sequences of configurations of magnetic flux density profiles can be displayed more easily by using a combination of two sketches. The first set depicts the magnitude of the flux density and the second its orientation. Both are drawn with respect to position in the specimen. This type of display will henceforth be employed in this thesis.

Figure 5.3(a) schematically illustrates the initial configuration of the trapped flux regardless of its orientation. The magnitude of the flux density is drawn as a function of position in the sample. Here $x = 0$ denotes the surface and $x = X$ the midplane. Because of symmetry with respect to the midplane, only half of the specimen needs to be represented. The flux density profile (B profile) is in a critical state throughout the entire volume of the sample. The procedure followed to trap the flux ensures that this state is established when H_a has been reduced to zero.

Possible orientations of the flux density are shown as a function of position in the sample in figure 5.3(b). θ denotes the angle of the tilted flux with respect to the y-axis. We stress that initially and after rotation all the flux lines are parallel to each other. The flux lines will be directed along the y-axis after a rotation of the trapped flux by 90° and a straight horizontal line overlapping with the y-axis is obtained. The upper line in Fig 5.3(b) corresponds to a rotation through 45° and the lowest line to a rotation of 135°.

Now, when H_a is applied and slowly increased, the evolving configurations of the profiles of B and θ must satisfy all the following physical requirements :

- continuity of B, θ, $E_{\parallel}$ and $E_{\perp}$

- $J_{\parallel} \cdot E_{\parallel} \geq 0$
- $J_{\perp} \cdot E_{\perp} \geq 0$

It is therefore imperative that the components of the electric field and of the current density be calculated throughout the disk as H_a is slowly increased.

In order to perform these tasks, we tailor Clem's equations for the components of the electric field from a time dependent to a time independent framework.

5.2 Application of Clem's Equations

In this section we exploit Clem's general critical state theory to describe our observations. We analyze the electromagnetic behaviour of the specimen in the context where the spatial and temporal variations of the magnetic flux density ($B(x)$ and $\theta(x)$ profiles) consist of sequences of metastable configurations. Consequently, we write :

$$\frac{\partial B}{\partial t} = \frac{\partial B}{\partial B_s} \frac{dB_s}{dt} \tag{5.1}$$

$$\frac{\partial \theta}{\partial t} = \frac{\partial \theta}{\partial B_s} \frac{dB_s}{dt} \tag{5.2}$$

where B_s is the magnetic flux density parallel to the surface(s) of the disk regarded as an infinite slab. We stress that at the surface(s) B_s is changing in magnitude only and is directed along the z-axis.

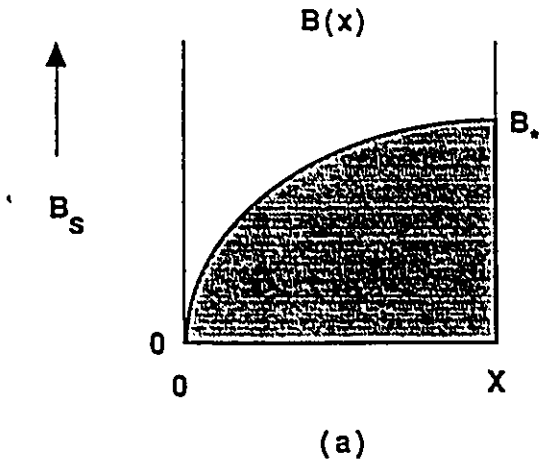

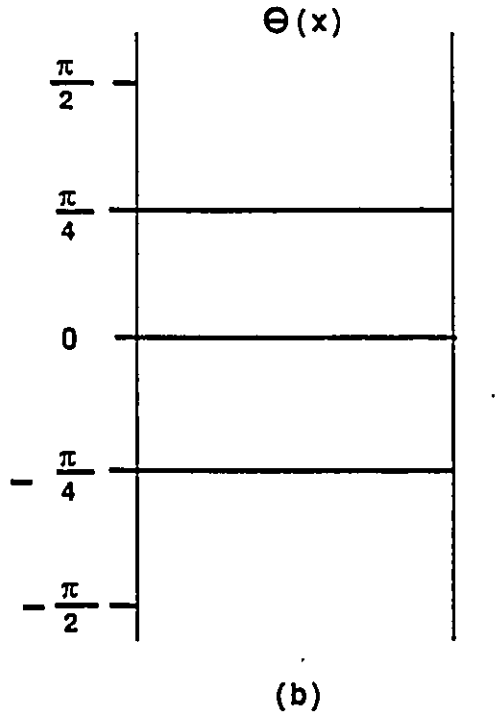

Figure 5.3: Initial profiles of the magnetic flux density $B(x)$ and its orientation $\theta(x)$.

Since the electric field is also dependent on time, we may write :

$$\vec{E}(x,t) = \vec{E}(x)\,\frac{dB_s}{dt} \tag{5.3}$$

With the last three relations, the time dependence in Clem's equations for the components of the electric field can be eliminated since all the terms carry the same time dependence.

Clem's equations now read :

$$\frac{\partial E_{\|}}{\partial x} = -B\,\frac{\partial \theta}{\partial B_s} - E_{\perp}\,\frac{\partial \theta}{\partial x} \tag{5.4}$$

$$\frac{\partial E_{\perp}}{\partial x} = E_{\|}\,\frac{\partial \theta}{\partial x} - \frac{\partial B}{\partial B_s} \tag{5.5}$$

The above coupled equations and Maxwell's equation for the components of the current density,

$$\mu_o\, J_{\|} = -B\,\frac{d\theta}{dx} \tag{5.6}$$

$$\mu_o\, J_{\perp} = -\frac{dB}{dx} \tag{5.7}$$

were solved computationally.

We solve this set of 4 coupled differential equations subject to the several specified constraints and the known boundary conditions as follows. Initially the trapped flux lines are all parallel to each other, are directed at a known angle with respect to $\vec{H}_a$ and exist in a critical state configuration throughout the volume of the specimen. Later, however, after H_a has been increased from 0 to any

arbitrary value (but always along the z-axis), the configuration of the magnetic flux has been transformed in magnitude, or in direction or both throughout the volume of the specimen. The pattern will now consist of a spatial juxtaposition of different zones (i.e. cutting-transport, pure transport, pure cutting and inert regions existing side by side). Let us assume for the sake of discussion that the specific arrangement existing at a given stage is known. An increment ΔH_a will lead to a new metastable (stationary) configuration. How do we determine this new configuration ?

First, we stress that the various zones that are encountered do not suddenly appear and disappear but gradually grow or shrink. In other words, the boundaries of the different regions migrate smoothly, advancing or receding as H_a is incremented. Consequently once the topography has been established, hence the nature, location and breadth of the various zones has been mapped out, the search for a solution consists in computationally identifying the new positions of the zone interfaces which ensue from an increment in H_a.

At the outset of the calculation, we assume, for computational convenience, that the initial application of H_a has generated critical state profiles for $B(x)$ and $\theta(x)$ in the volume adjacent to the surface where the disturbance in the arrangement of the flux lines has penetrated. This is achieved using equations 5.6 and 5.7 where $J_{\|}$ and $J_{\perp}$ are taken to be critical. Introducing these variations in the configuration of $\theta(x)$ and $B(x)$ into equations 5.4 and 5.5 we explore whether these changes generate a pattern of electric fields which satisfy the requirement that $E_{\|} \cdot J_{\|} > 0$ and $E_{\perp} \cdot J_{\perp} > 0$.

In the event that either or both of these conditions are not satisfied in some

region of the specimen, the computer program we have developed proceeds to test the various alternatives guided by the location of the boundaries of the domain where the sign of $E_\perp$ and/or $E_\parallel$ has emerged as incorrect. As a consequence, the initial exploratory calculation indicates the way towards a correct solution, hence, the true $\theta(x)$ and $B(x)$ profiles.

The sequences of correct $\theta(x)$ and $B(x)$ profiles are then utilized to calculate sequences of $< B_z >$ and $< B_y >$, spatial averages of the magnetic flux density in the laboratory frame since these are two quantities which are continuously observed in our experimental set-up.

In order to obtain a complete and detailed picture of the physical events which occur as the applied field H_a disturbs the flux trapped in the disk it is also of great interest to follow the evolution of the configuration of the components of the electric field and of the current density. We will consequently display sketches of the sequences of $B(x)$, $\theta(x)$, $E_\parallel(x)$, $E_\perp(x)$, $J_\parallel(x)$ and $J_\perp(x)$ profiles which are believed to arise as the phenomema we observe take place.

5.3 Outline of our Theoretical Survey

5.3.1 General Approach

The magnitude of the depinning critical current density $J_{c\perp}$ and its dependence on B can be fairly readily extracted from measurements of the "standard" magnetization curves. It is important that the demagnetization factor be negligible. This is accomplished by fabricating a specimen in the form of a long ribbon, long

cylinder or thin disk and directing H_a along the length of the sample or $\parallel$ to the flat surfaces of the disk. In these "standard" magnetization measurements, the flux lines entering or leaving the specimen are parallel to each other and to the surfaces of the sample. The critical state picture we have outlined earlier in this thesis provides a simple framework and uncomplicated formulae for obtaining $J_{c\perp}$ vs B from the saturation magnetization data vs H_a increasing and decreasing. This avenue has been extensively travelled by many workers and an extensive literature has already accumulated on these efforts. In these endeavours it is frequently convenient to choose a simple analytic expression for $J_{c\perp}$ vs B and test its validity by comparing the ensuing computed magnetization curves with the observations. This is the approach we have followed in our work. This approach is particularly useful since it also enables the researcher to investigate the effect on the magnetic behaviour of varying the functional dependence of $J_{c\perp}$ on B.

The determination of the magnitude of the flux cutting critical current density $J_{c\parallel}$ and its dependence on B is a complicated exercise. Here no simple formulae have been developed which directly relate $J_{c\parallel}$ to the magnetization data in a straight forward way. Indeed, it is perhaps a dream to hope that simple relationships will be found. Given the present state of affairs in this area we have followed the expedient of postulating simple analytic forms for $J_{c\parallel}$. Our chief guide in this guessing game has been physical and conceptual simplicity. Consequently we have assumed in our work that $J_{c\parallel}$ and $J_{c\perp}$ will obey the same functional dependence on B and presumably also on the temperature T. Thus once a simple B dependence for $J_{c\perp}$ has been identified on a semi empirical basis, the sole adjustable parameter in our exploration is the ratio of $J_{c\parallel}$ to $J_{c\perp}$. The merits of this straight forward

approach will of course emerge from its failure or success in reproducing a vast assortment of intricate observations.

5.3.2 Choice of Specific Expressions for $J_{c\|}$ and $J_{c\perp}$

For the range of weak fields far below H_{c2}, it has been well established that the standard magnetic behaviour (flux lattices of parallel flux lines) can be satisfactorily described by simple B dependence for $J_{c\perp}$ of the form,

$$J_{c\perp} = \pm\frac{\alpha}{B^n} \tag{5.8}$$

where $0 \leq n \leq 1$. The limit where n=0, hence $J_{c\perp} = \pm\alpha$ and is independent of B, is known as the Bean approximation. The limit where n=1, hence $J_{c\perp} = \pm\alpha/B$ is called the simple Kim approximation. Originally Kim et al introduced an additional parameter B_o in this expression, and wrote $J_{c\perp} = \pm\alpha/(B_o + B)$. An intermediate form of eqn 5.8, where n=1/2, is referred to as the Yasukochi approximation and generally provides a better fit to most data. The limits n=0 and n=1 are particularly useful because they appear to bracket the range dictated by the physics of pinning.

In view of our basic simplification that $J_{c\|}$ and $J_{c\perp}$ are related by a coefficient characteristic of the specimen, we write

$$J_{c\|} = \pm\frac{k}{B^n} \tag{5.9}$$

and always choose the same value of n in eqns 5.8 and 5.9 to describe the behaviour of a specimen when flux cutting enters into the picture.

For investigations pertaining to the remanent trapped flux, the important physical quantities are H_* and H_{**}. It can be seen that these two quantities are related and the maximum ratio for H_{**}/H_* is two (Bean approximation) and $\sqrt{2}$ (Kim approximation). When these parameters are small relative to H_{c2}, the simple expressions just given are quite adequate. This is the state of affairs which prevails for the measurements on the high T_c specimen and the $PbBi$ samples studied by Sekerka. In some important situations however H_{**} is not negligible compared to H_{c2}. This is the situation encountered in Niobium. Consequently here the effect of H_{c2} on $J_{c\perp}$ and $J_{c\parallel}$ must be taken into account.

Indeed for the Nb specimens, the magnitude of the magnetization decreases precipitously near H_{c2}. The rapid decline in this region is a "smeared out" step function. This behaviour can be taken into account by introducing a variety of more or less simple analytic expressions. To achieve the desired result we have chosen to introduce a factor of the form $(1-(B/B_{c2})^m)$ where $m \gg 1$ in eqns 5.8 and 5.9. Thus,

$$J_{c\perp} = \pm\frac{\alpha}{B^n}\,(1-(\frac{B}{B_{c2}})^m) \tag{5.10}$$

and,

$$J_{c\parallel} = \pm\frac{k}{B^n}\,(1-(\frac{B}{B_{c2}})^m) \tag{5.11}$$

Besides its simplicity, this approach has the advantage of relating directly to various physical features, such as the condensation energy, when $1 \leq m \leq 2$. To describe the rapid descent observed near H_{c2} in Niobium, however, m needs to be chosen an order of magnitude larger.

5.3.3 Extent of our Survey

Exploiting the computer program we developed to solve the four coupled Clem equations subject to the various physical constraints enumerated earlier we have investigated the evolution of $< M_y >$ and $< M_z >$ as H_a is impressed and removed with,

- the trapped flux rotated through 45°, or 90° or 135° and
- sweeps of H_a extending up to 2 H_* when $H_{c2} \gg H_{**}$ and
- sweeps of H_a extending up to H_{c2} when H_{**} approaches this quantity.

For the cases where H_{c2} can be ignored, we have carried out these calculations with $n = 0, 1/2$ and 1, hence for the three basic approximations enshrined in the literature.

In every case, we have examined the effect of different ratios for $J_{c\|}/J_{c\perp}$, usually letting $J_{c\|}/J_{c\perp} = 1, 2, 3$ or 4.

The scrutiny of this rich assortment of behaviour has been very instructive for us and could be most useful to workers focusing on this area of research. In the next pages we display a small selection from this vast catalogue of calculated curves for illustrative purposes and for direct comparison with a representative portion of experimental observations.

5.4 Theoretical Results

From the extremely large catalogue of theoretical curves we concentrate on one scenario for display. The choices made for this study are summarized as folllows:

- **Kim approximations for $J_{c\|}$ and $J_{c\perp}$.**
- **Trapped flux initially oriented at 90° with respect to the incoming flux.**
- **A ratio of $J_{c\|}$ to $J_{c\perp}$ corresponding to 3.**
- **$B_{c2} \gg B_s$ for all H_a.**

We choose the notation B_s to denote the magnetic flux density just inside the surface and H_a to indicate the magnetic field outside. For simplicity we take $B_s = \mu_o H_a$, hence we ignore the presence of an equilibrium diamagnetic (Meissner) current.

The profiles of the various physical quantities and their evolutions as H_a is increased are presented in figures 5.4 through 5.12 for the above choice of parameters and approximations.

5.4.1 Evolution of $B(x)$ and $\theta(x)$ for H_a Increasing

The initial B and θ profiles are depicted in Fig 5.3. We now focus on the case where the trapped flux has been rotated through 90°, hence flux lines are made to enter the specimen at an angle $\theta = \pi/2$ with respect to the initial configuration.

In Figs 5.4 through 5.12, flux is entering from the left, the surface is located at $x = 0$ and the midplane is at the extreme right of the drawings.

The initial sequence of B profiles is shown in Fig 5.4. The sand pile analogy, first introduced by de Gennes [16], is useful for visualizing a major feature of these curves. "Sand" (flux) is being poured through the surface into the specimen where a "critical" mound of sand (trapped flux) has already been stored.

The formation of a valley, with a downward slope on its left and an upward incline on its right, is easy to see as sand pouring in through the surface piles up on top of the initial "sand dune". The slope of the advancing sand formation is critical and its height at the surface rises as H_a, the source of the "sand" rises. The front of the encroaching sand dune moves up higher and further along the positive slope of the mound of stored sand. Thus the bottom of the valley formed by the invading sand dune and the stored sand dune, moves inwards and upwards until it reaches the center (middle) of the sand box. At this juncture and subsequently, the progress of the sand pile (B profile) is displayed in Fig 5.5.

Indeed, the analogy we have exploited describes the sequence of events quite closely for the case where the invading flux lines are all parallel to the trapped flux lines, i.e. if no initial rotation of the trapped flux had occurred. A novel and important feature appears under the conditions of our experiment where the orientation of the invading flux lines is different from that of the trapped flux lines. Under these circumstances, the sand pile analogy, although quite fertile, predates the concept of flux line cutting and does not take this process into account.

The reader will note that the B profiles on the right hand side of the minima in Fig 5.4 are not stationary as would be the case in the context of the sand

pile analogy. Here the B profiles are seen to diminish in height as the left hand side rises. Let us denote the left and right hand sides of the valleys as regions 1 and 2 respectively for brevity. The density and the total population of flux lines permeating region 2 is dropping.

This drop occurs in part because some of the trapped flux lines are migrating leftwards towards the advancing front or boundary of region 1, i.e. the valley bottom (minimum in the $B(x)$ profiles). This leftward displacement leads to a decompression (lower packing density) of the flux lines adjacent to the midplane. Several related questions arise and need to be answered. (i) Why is this leftward migration of flux lines in zone 2 taking place ? (ii) What happens to these migrating flux lines ? (iii) Why is the declining population of flux lines in zone 2 not filling up the valley ? These events are all direct consequences of the operation of Clem's equations (i.e. Maxwell's equations), basic physical constraints and, specifically the Clem conditions that $E_\perp \cdot J_\perp > 0$ and $E_\parallel \cdot J_\parallel > 0$, i.e. flux line depinning and flux line cutting dissipate energy. We will endeavour to describe and explain the main features of the phenomena which ensue from the application of this framework.

The main feature encountered in the present situation is that the entry of flux at the surface causes a disturbance which is not confined to the volume adjacent to the surface (region 1) as in the classical case of an interaction of parallel flux lines. Here, the penetration of flux lines tilted with respect to the existing population, perturbs the entire landscape and generates much activity over the entire cross section of the specimen. As a result, region 2 actually comprises two zones. Adjacent to the minimum in the $B(x)$ profile, there exists a subzone of region 2

where flux line cutting and leftwards migration of flux lines are occurring. This is denoted a CT_- zone, the minus sign indicating flux line transport to the left. At the interface or boundary of region 1 and this subzone, invading flux lines interact and undergo flux cutting with flux lines arriving from the CT_- subzone. This counter or cross flow takes place at the minimum in $B(x)$ which constitutes a sink where flux is being consumed.

Since dB/dx, the gradient of $B(x)$, changes sign across this minimum in the B profile and $J_{c\perp} = -dB/dx$, then $J_{c\perp}$ must also change sign across this interface. Further, in order that $E_\perp \cdot J_\perp > 0$, it follows that $E_\perp(x)$ must also change sign across this boundary. The spatial variation of $E(x)$ however must be continuous. These two conditions control the rate of decline of the B profiles in zone 2.

Flux in the CT_- zone is being replenished by migration of flux lines out of the adjoining subzone of region 2. The latter is consequently a pure transport (T_-) zone. The boundary or interface between the two subzones of region 2 (i.e. the CT_- and T_- zones) is defined by the front of the advancing $\theta(x)$ profiles (see Fig 5.6).

Region 1, the region to the left of the minimum in B, is a CT_+ zone, the + sign indicating that the invading flux lines are advancing towards the right. Both flux line displacement and flux line cutting are taking place throughout this region since here both the gradient of B and the gradient of θ are critical. (Recall that $\mu_o J_{c\perp} = -dB/dx$ and $\mu_o J_{c\parallel} = B\ d\theta/dx$).

Examining Figs 5.4 and 5.6 together, we can identify the boundaries of the various zones and observe the movement of these frontiers as H_a is made to increase.

First considering the curves labeled 1 in these two figures, we note that, region 2 is initially entirely a T_- zone since the bottom of the valley and the front of the θ profile coincide. As the rise of H_a progresses, a narrow CT_- subzone of region 2 appears between the expanding CT_+ zone (region 1) and the T_- subzone of region 2. This narrow CT_- zone extends from the valley minimum to the front of the θ profile (see curves labeled 2 in Figs 5.4 and 5.6). This narrow CT_- zone is observed to have expanded from consideration of the position of these two features for the curves labeled 3. Evidently, throughout all this expansion of the invading CT_+ region 1 and the growth of the adjacent CT_- subzone, the available space occupied by the T_- subzone is being reduced. Eventually, as region 2 continues to diminish, the CT_- subzone also undergoes shrinkage and both the CT_- and T_- zones are doomed to disappear. The T_- vanishes when the front of the $\theta(x)$ profile attains the midplane and soon thereafter, the CT_- subzone is also wiped out when the valley bottom touches the midplane.

At this last juncture, H_a must lie between H_* and H_{**}. Since the $B(x)$ profile does not drop to zero at the midplane, it follows that H_a must be greater than H_*. However H_a must be less than H_{**} since the flux line density at the midplane has been falling throughout the events we have just described.

We now refer the reader to Fig 5.5 which again displays the B profiles shown in Fig 5.4 and two typical B profiles labeled 4 and 5. Examining the latter together with the corresponding θ profiles of Fig 5.6 we note that henceforth the entire sample is filled by the left hand side of a "valley" (region 1) and is hence occupied by a CT_+ zone. This simple state of affairs persists until H_a attains H_{c2} provided that the ratio $J_{c\|}/J_{c\perp}$ does not exceed a threshold value ≈ 5.

We stress that the profiles displayed in Figs 5.4 through 5.12 are not schematics but exact tracings of theoretical curves chosen from the vast family of sequences of calculated curves. It is also important to note that, prior to the disappearance of region 2, each profile in the sequence of configurations requires for its computation knowledge of the previous pair of B and θ profiles as input for their determination. The fact that a single CT_+ zone fills the entire specimen when the valley has vanished considerably simplifies the computation of the $B(x)$ and $\theta(x)$ profiles in the latter regime. Now the calculation is no longer "sequential", i.e. dependent on knowledge of the previous configurations. In this regime, the two equations $\mu_o\ J_{c\perp} = -dB/dx$ and $\mu_o\ J_{c\|} = B\ d\theta/dx$ together completely determine the configurations.

We now continue to exploit the equations containing $E_\perp$ and $E_\|$ (the Maxwell-Faraday eqn $\nabla \times \vec{E} = -\partial\vec{B}/\partial t$) to ascertain that indeed $E_\perp \cdot J_\perp > 0$ and $E_\| \cdot J_\| > 0$ as required.

5.4.2 Evolution of the Profiles of $E_\|(x)$ and $E_\perp(x)$ as H_a is Increased

The gross feature of the sequences of B and θ profiles are fairly straight-forward to visualize and understand without mathematical analysis once it is realized that the hill of trapped flux (region 2) is being eaten and falls because it feeds some of its stored flux lines to be "decimated" or consumed by flux cutting with the invading hordes of flux lines.

The differential equations governing the profiles of $E_\|(x)$ and $E_\perp(x)$, however,

involve too many coupled terms for us to explain or justify their shapes and their evolutions. We relate the salient features to the various events taking place in the flux distribution (i.e. the sequences of B and θ profiles just examined).

Since flux migration is taking place throughout the specimen, (inwards in region 1 and outwards in region 2 while the latter exists), a depinning electric field $E_\perp$ appears everywhere from the beginning of the rise of H_a. The direction of motion of the flux lines readily emerges from inspection of the sequence of $B(x)$ profiles, since flux lines move "downhill" hence down the slope of the critical $B(x)$ profiles when they become unpinned. It can be shown that the Maxwell-Faraday equation and the equation of continuity (or conservation of the flux line number inside a superconductor) leads to,

$$E_\perp(x) = v(x)\, B(x) \tag{5.12}$$

where $v(x)$ is the velocity of the flux lines. Thus a knowledge of the direction of motion of the flux lines readily informs us on the sign of $E_\perp(x)$. Consequently, $E_\perp$ is positive in region (1) and negative in both the CT_- and T_- subzones of region 2.

Since the minimum in the valley of the $B(x)$ profile constitutes the boundary between regions 1 and 2, it follows that $E_\perp(x)$ must change sign at this frontier. Indeed, the procedure followed to solve Clem's equations consists in a computer search for the appropriate magnitude of the decrease of the $B(x)$ profile in region 2, accompanying or generated by an increment of the $B(x)$ profile in region (1) which will ensure that the cross over of $E_\perp(x)$ from + to - will coincide with the minimum

in $B(x)$. The search for a solution is made more complicated by the presence of the CT_- subzone in region 2. The flux cutting electric field $E_{\|}(x)$ in this subzone has an effect on $E_{\perp}(x)$ as can be seen from inspection of Clem's coupled equations for $E_{\|}$ and $E_{\perp}$. The physical reason for this linkage or interdependence between $E_{\perp}(x)$ and $E_{\|}(x)$ is the following.

Flux can be made to diminish in a region in two ways : via emigration (flux transport) and through flux line cutting since the latter process consumes flux. The two mechanisms operate in tandem in a CT zone where B is declining, hence in the CT_- subzone of region 2. In region 1, where there is a net increase of flux, the flux line cutting processes consume flux but it is replaced at a greater rate by immigration of flux lines through the surface.

A flux cutting electric field $E_{\|}$ is generated in the volume behind the front of the advancing critical θ profile. This electric field rises smoothly from zero and not discontinuously at the front of the disturbance in the θ profile because the gradient of θ is finite at this frontier. The flux lines to the right of the advancing critical θ profile are migrating leftwards while retaining their initial parallel orientation unchanged.

After zone 2 has been extinguished by the advance of zone 1 to the midplane as H_a has been increased, the inward migration of flux now occurring throughout the specimen generates a depinning electric field $E_{\perp}(x)$ everywhere. This electric field diminishes smoothly to zero at the midplane, since at this mathematical plane there is no motion of the flux lines although the magnetic flux density there is changing as H_a increases. Flux lines are arriving at the midplane from both surfaces in our experiment, hence $v = 0$ at the midplane where flux arriving from

the left meets with flux arriving from the right surface. We note also that by symmetry, the flux lines reaching the midplane from the left surface have the same orientation as the flux lines coming in from the right surface, hence no flux line cutting can take place at the midplane in our work. Consequently $E_{\|}$ must be zero at this plane although zone 1, a CT_+ zone, fills the entire half space. $E_\perp$ and $E_{\|}$ are now seen to rise smoothly from zero at the midplane and vary in magnitude but not in sign from that plane to the surface.

Since the slope of the B profiles and θ profiles becomes shallower as the rise of H_a progresses beyond H_* and H_{**} towards H_{c2}, it is not surprising that the maximum magnitudes of $E_\perp(x)$ and $E_{\|}(x)$ diminish correspondingly as can be seen from curves 4 and 5 in Figs 5.7 and 5.8.

5.4.3 Evolution of the $J_{\|}(x)$ and the $J_\perp(x)$ Profiles as H_a Increases

The salient features of the $J_\perp(x)$ and $J_{\|}(x)$ profiles displayed in Figs 5.9 and 5.10 emerge readily from consideration of the B and θ profiles (see Figs 5.5 and 5.6) bearing in mind that $\mu_o J_{c\perp} = -dB/dx$ and $\mu_o J_{c\|} = B\ d\theta/dx$.

Firstly we note that $J_\perp$ displays an abrupt change of sign across the bottom of the valley in the B profile. This is to be expected since the gradient of B is - on the left side and + on the right side of the valley. The magnitude of $J_\perp(x)$ is the same on both sides of the discontinuity and varies symmetrically with distance from the valley minimum since the valley itself is symmetric. Also, $J_{c\perp}$ diminishes with B increasing, as required by our choice of dependence on B. Thus as H_a/H_*

becomes large, $J_\perp$ (and $J_\parallel$) become smaller.

$J_\parallel(x) = 0$ in the pure flux transport subzone of region 2 since here the flux lines are all $\parallel$ to each other, hence $d\theta/dx = 0$. We note that $J_\parallel$ rises abruptly at the front of the advancing critical θ profile (see curves labeled 1,2 and 3 in Fig 5.10). The rise in $J_\parallel$ is discontinuous at this interface because the slope of the θ profile is finite at this frontier.

The peak in $J_\parallel(x)$ evident in curves 2 and 3 of Fig 5.10 is associated with the valley minimum in the B profile. The peaks arise from the B dependence of $d\theta/dx$ together with the symmetry of the valley with respect to its minimum.

We can readily verify that, as required by the Clem's constraints, $E_\perp$ and $J_\perp$ have the same sign everywhere and similarly for $E_\parallel$ and $J_\parallel$ by inspecting Fig 5.7 together with 5.9 and Fig 5.8 with 5.10.

5.4.4 Evolution of the $B_y(x)$ and the $B_z(x)$ Profiles

For completeness, we have included the profiles showing the evolution of $B_y(x)$ and $B_z(x)$ as H_a progresses (Figs 5.11 and 5.12). Their general form can easily be deduced from the $B(x)$ and $\theta(x)$ profiles. We remind the reader that $B_y = B\ \cos\theta$ and $B_z = B\ \sin\theta$. One striking feature observed in the $B_y(x)$ profiles are the dents in the first few profiles. These occur at the same location as the bottom of the valleys in the B profiles and are another manifestation of the valley minimum.

Now that we have thouroughly investigated the behavior of the various physical quantities as H_a was augmented, we will follow their evolutions as H_a is decreased down to zero field.

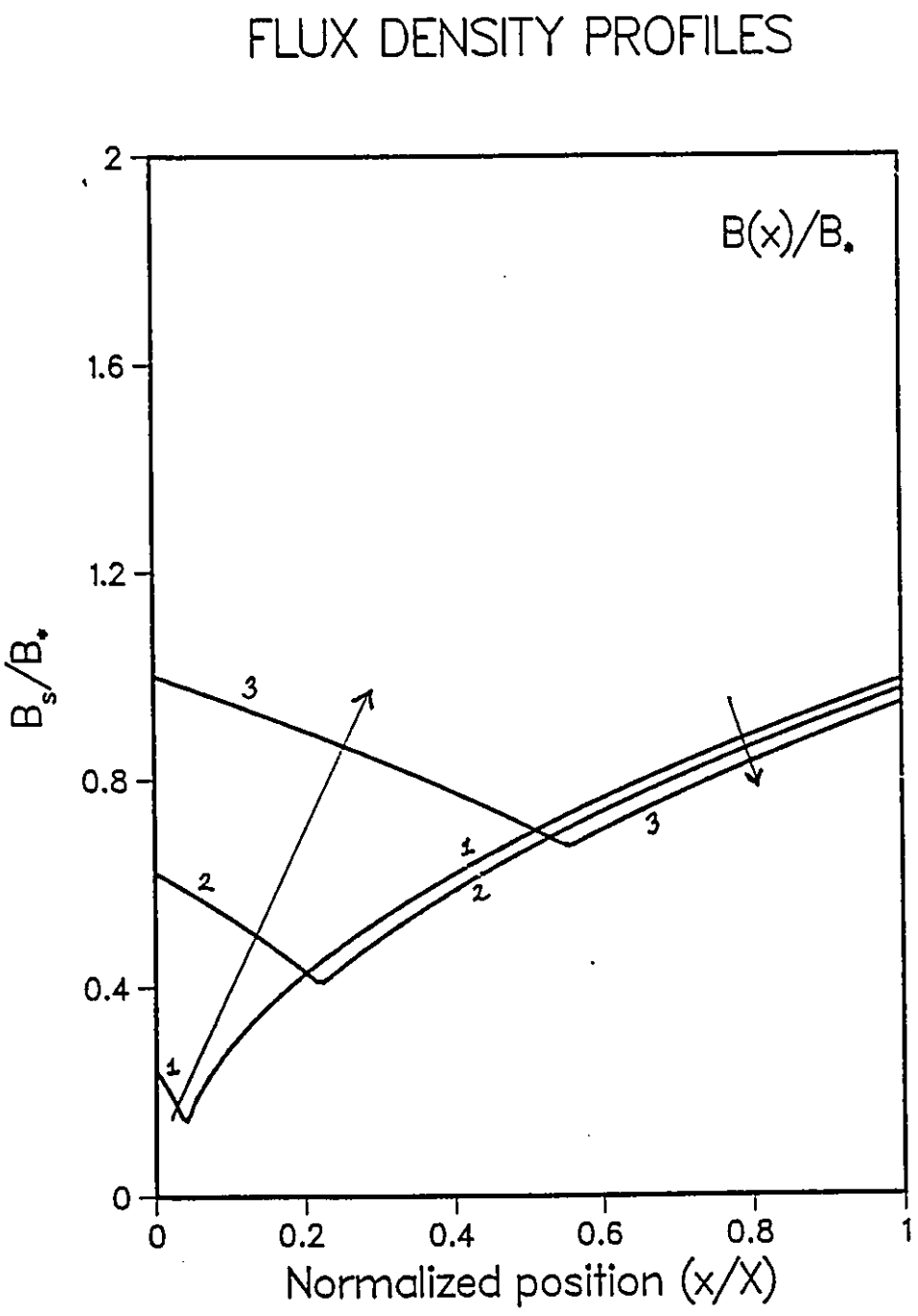

Figure 5.4: Initial sequence of $B(x)$ profiles as H_a increases.

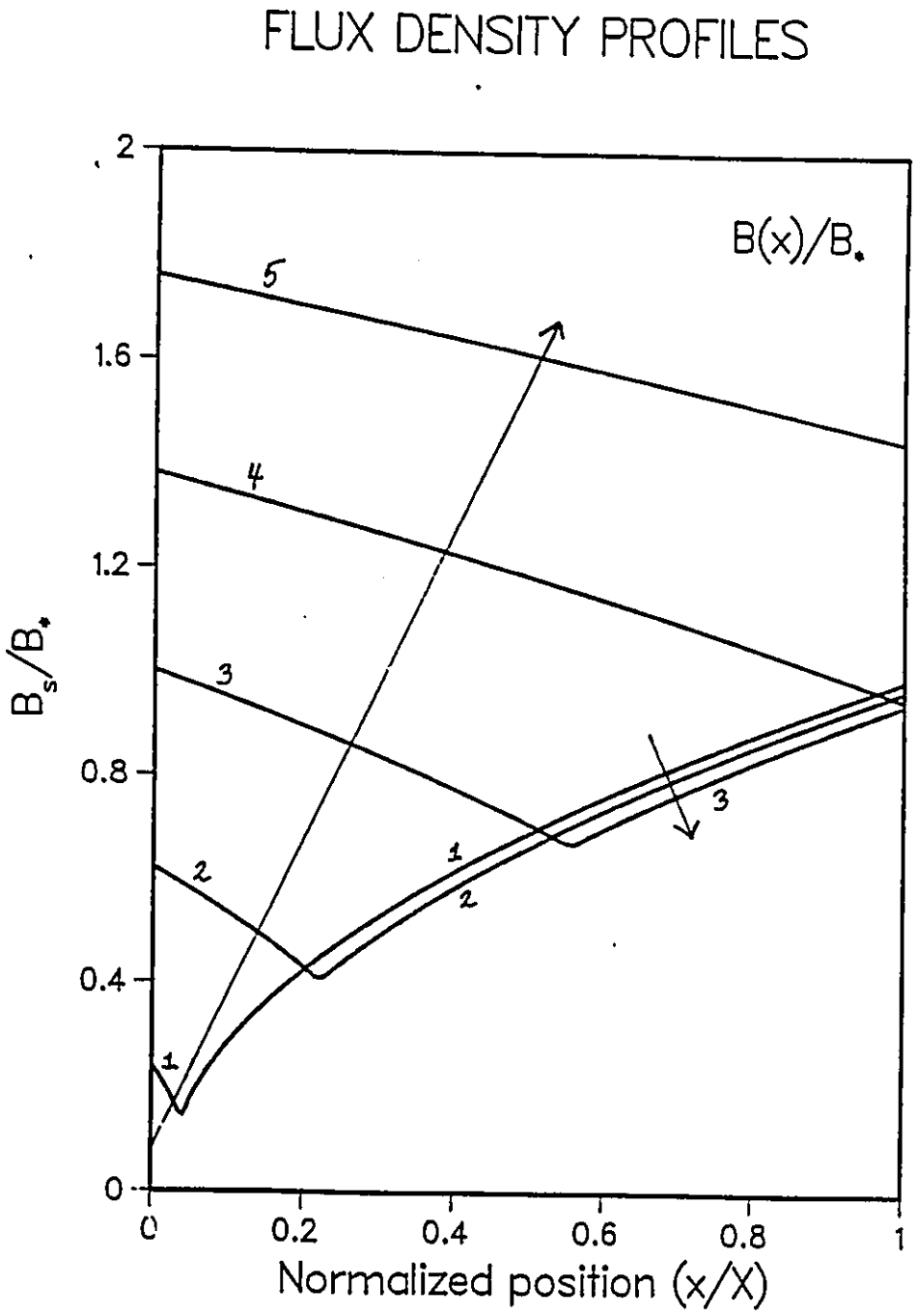

Figure 5.5: Sequence of magnetic flux density profiles as H_a increases.

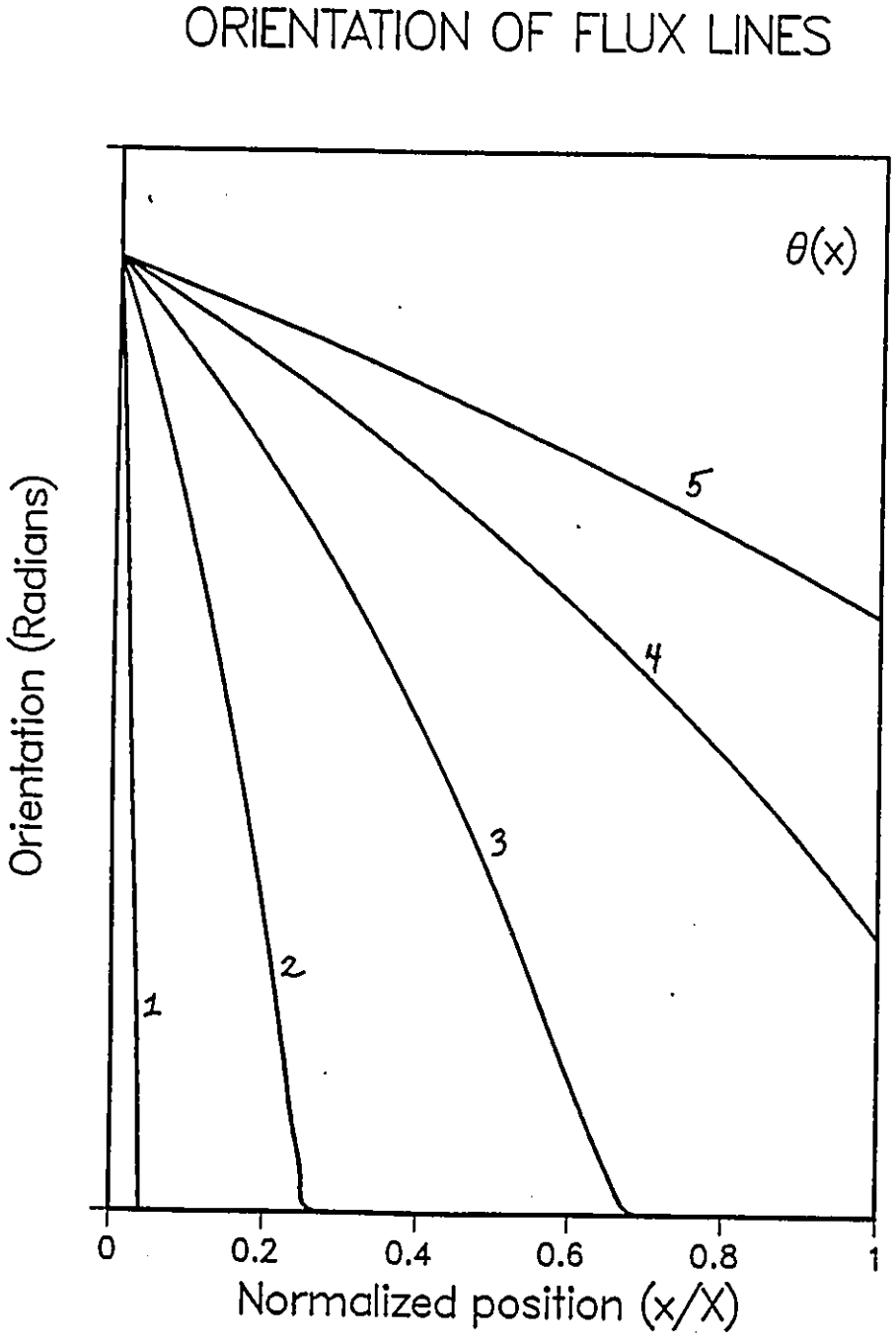

Figure 5.6: Sequence of the profiles depicting the orientation of the flux lines as H_a increases.

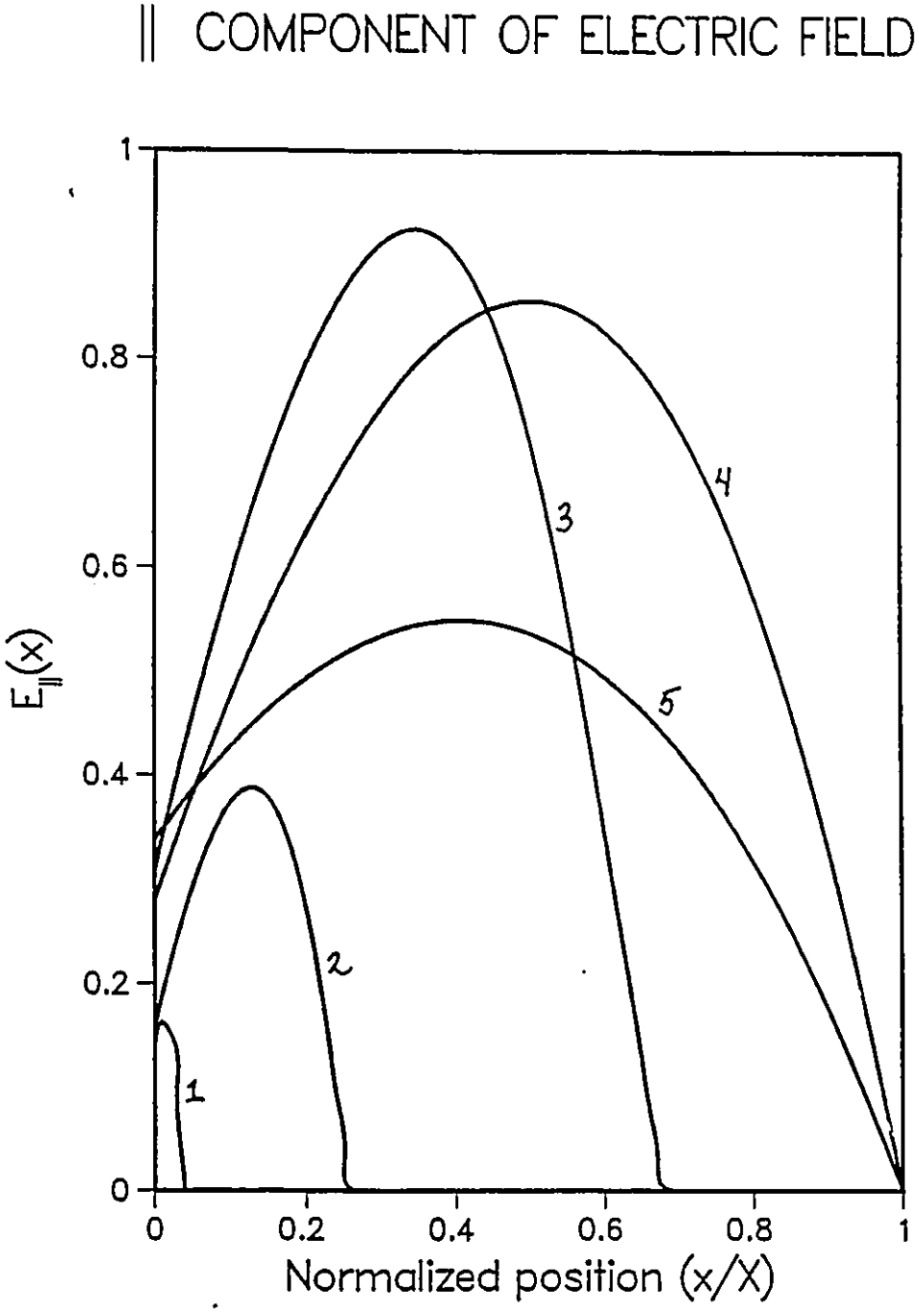

Figure 5.7: Evolution of $E_{\parallel}(x)$ as H_a increases.

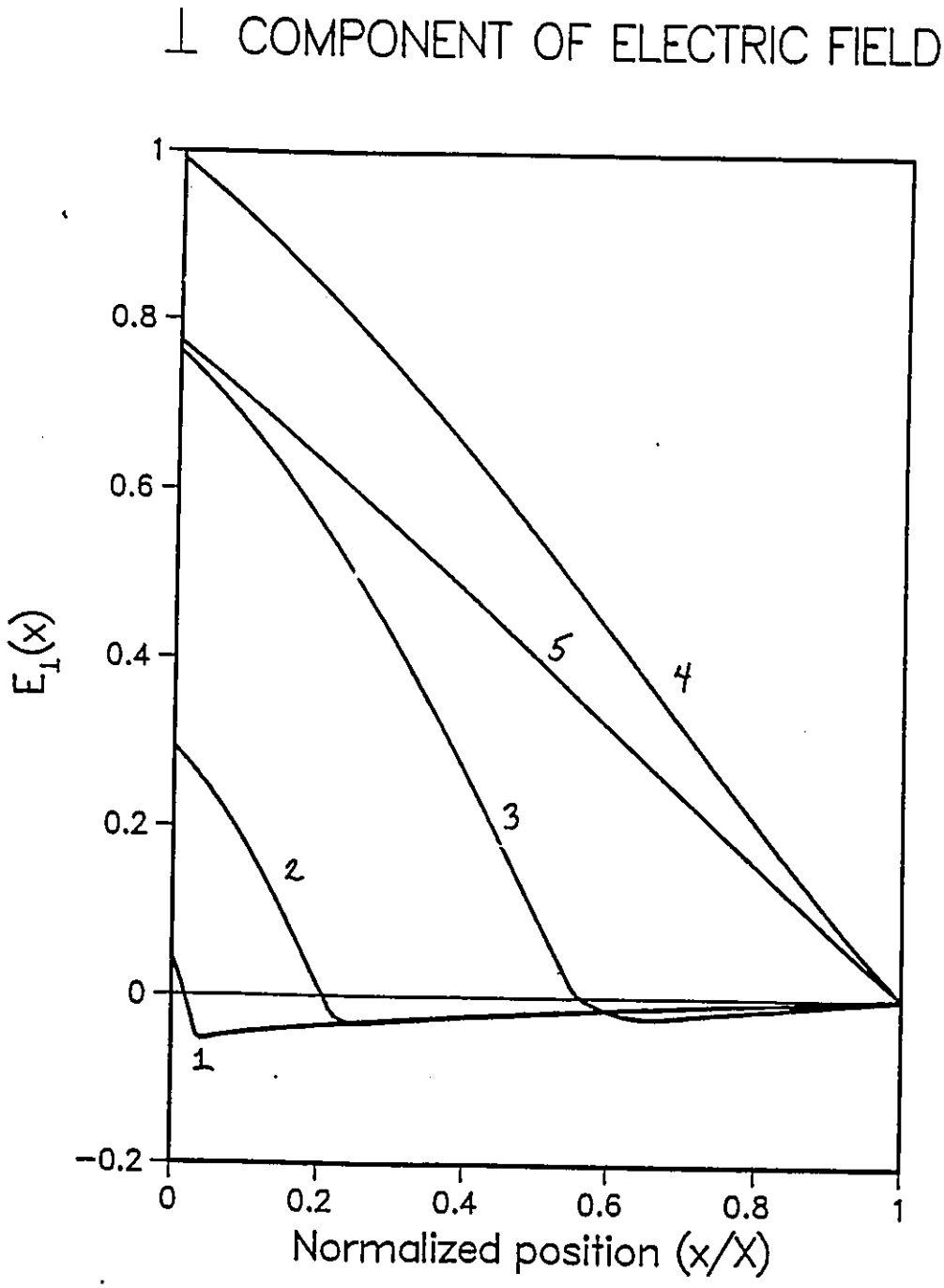

Figure 5.8: Evolution of $E_\perp(x)$ as H_a increases.

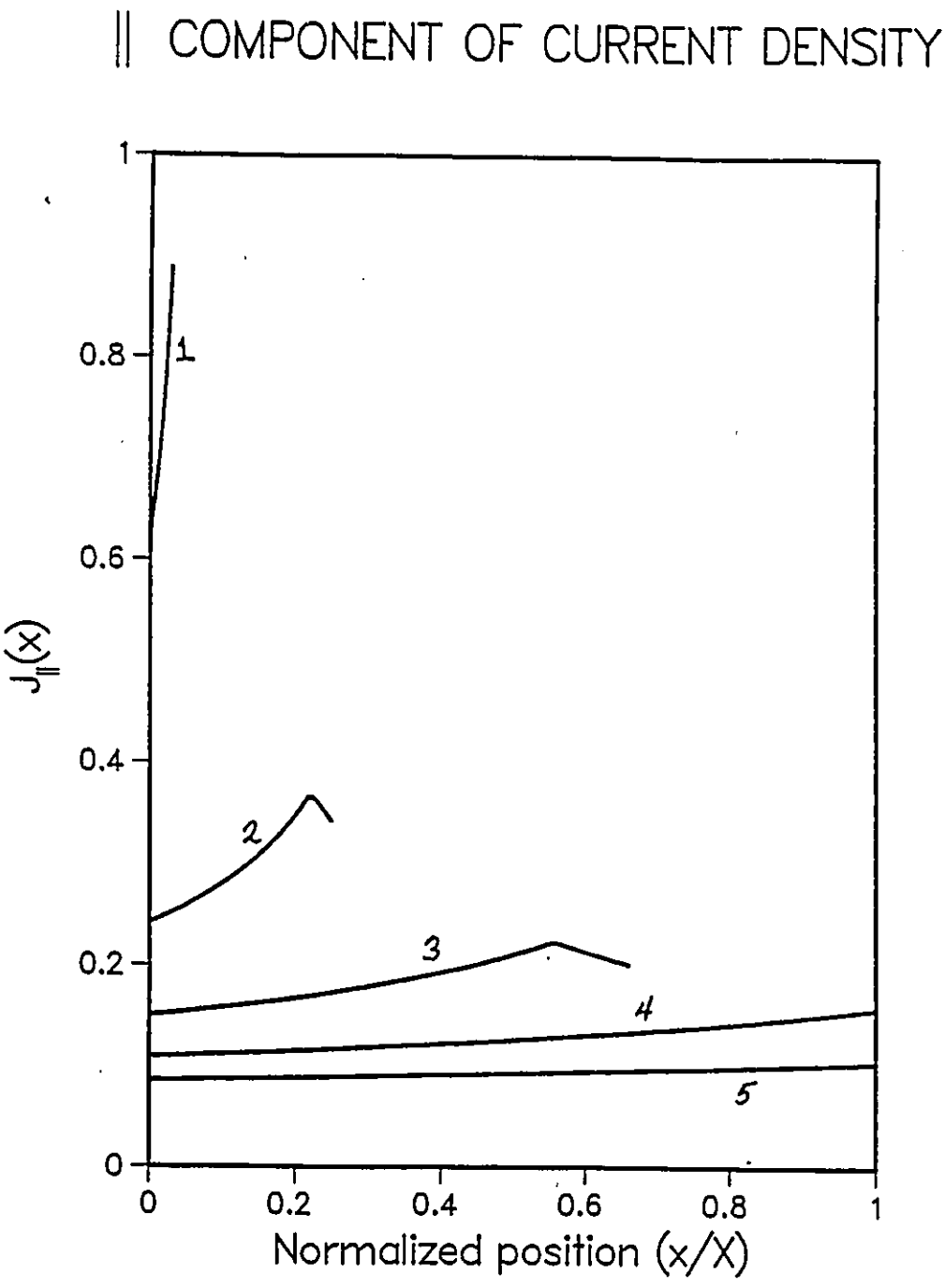

Figure 5.9: Evolution of $J_{\parallel}(x)$ as H_a increases.

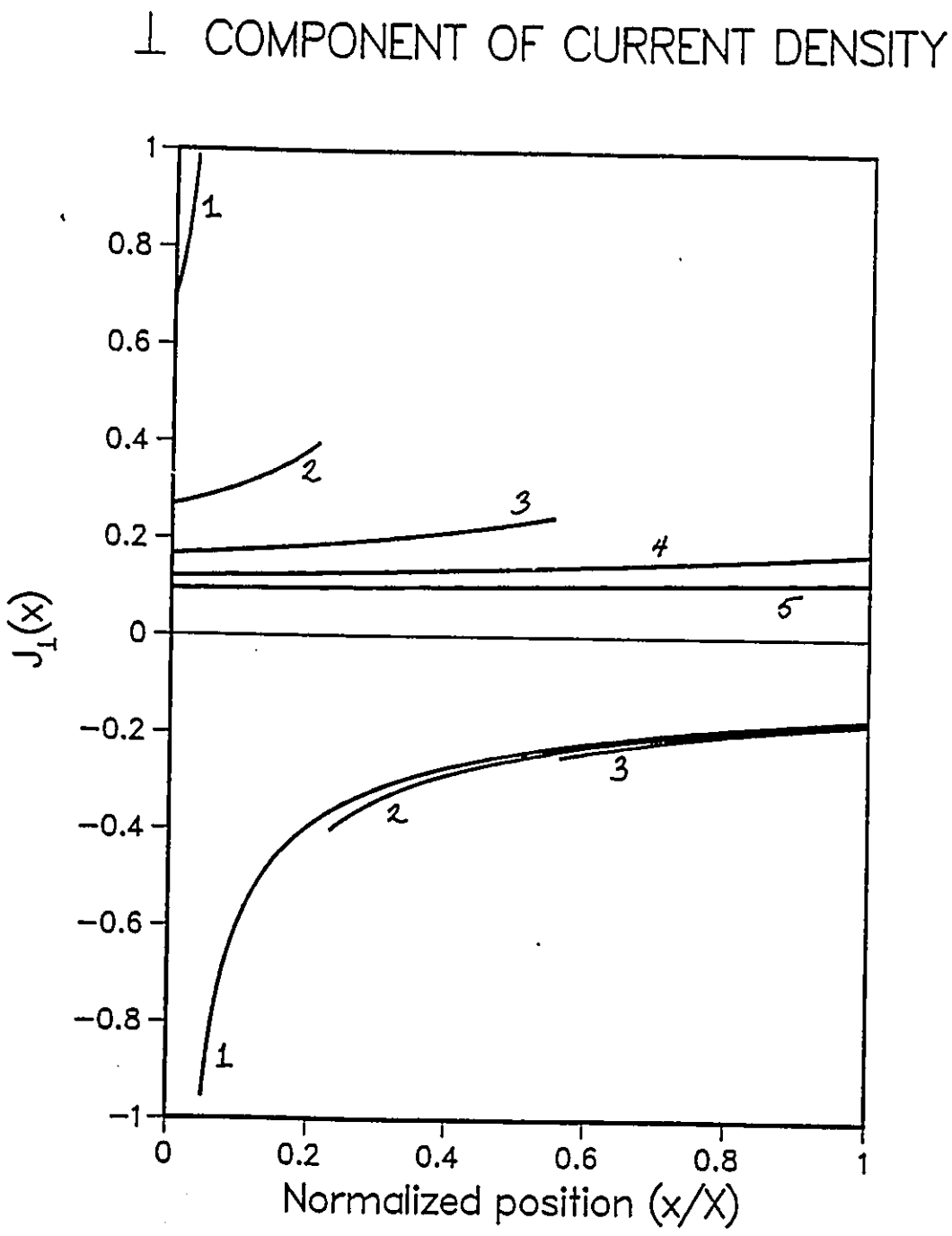

Figure 5.10: Evolution of $J_\perp(x)$ as H_a increases.

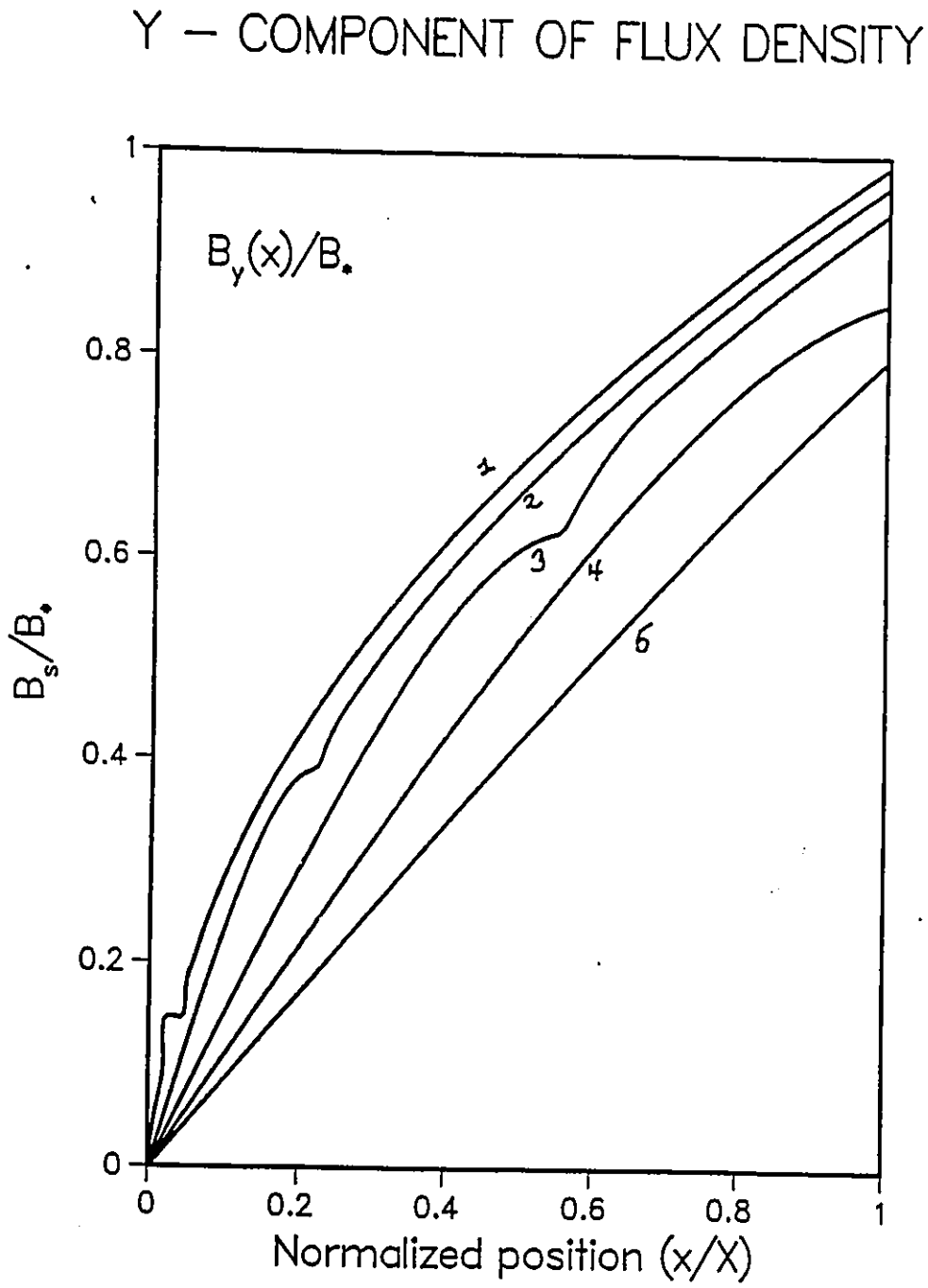

Figure 5.11: Evolution of $B_y(x)$ as H_a increases.

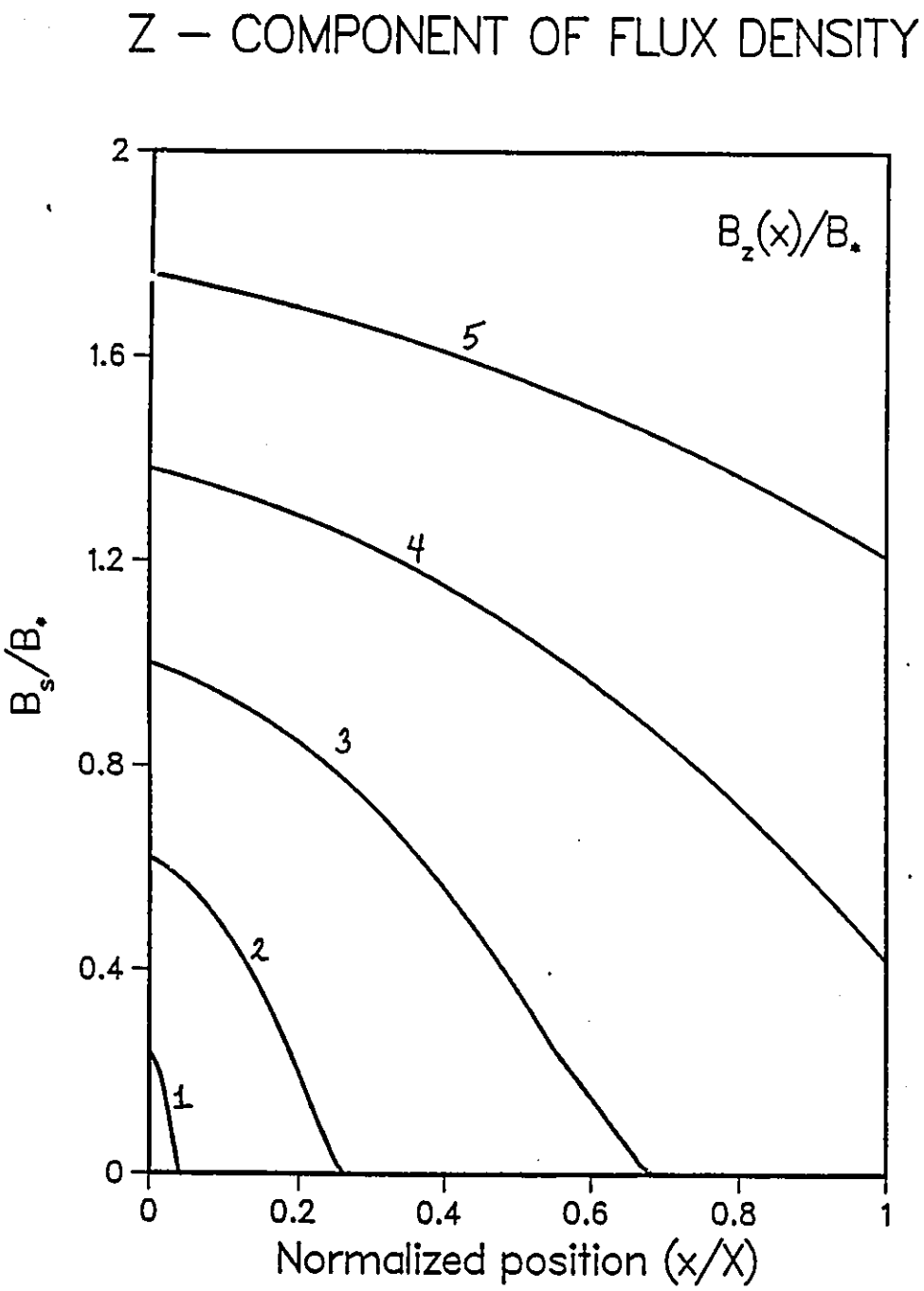

Figure 5.12: Evolution of $B_z(x)$ as H_a increases.

5.5 Evolution of $B(x)$ and $\theta(x)$ as H_a Decreases

We now turn our attention to the evolution of the $B(x)$ and $\theta(x)$ profiles as H_a is now decreased after having been raised to some selected maximum value large compared with H_* (or H_{**}) but small compared to H_{c2}. The profiles depicted in the final stage of the previous section constitute the initial profiles for this development. Again an examination of the sequence of $B(x)$ and $\theta(x)$ profiles sheds considerable light into the electromagnetic events which take place.

The initial salient feature is the peak or summit in the B profile (see curves labeled 1 and 2 in Fig 5.13). Now we encounter a peak instead of a valley since here the flux lines are flowing outwards to the left as H_a diminishes. The configuration of the "sand pile" is modified into a hill. The density and the orientation of the flux line lattice between the summit and the mid plane remains "frozen" and undergoes no alteration. The peak (as was the case previously with the valley minimum) advances towards the midplane and eventually attains this position as the decrease of H_a progresses. Once the peak has reached the midplane, the B profile for the entire specimen now displays a simple hill with its edges at the two surfaces of the disk and its summit centered on the midplane. Subsequently, as H_a is reduced, this hill descends as can be seen from the curves labeled 3,4 and 5 in Fig 5.13. We stress that these curves display only the configurations in the left side of the specimen hence only half of the hill or sand pile.

In contrast to the scenario encountered during the ascent of H_a, the flux configuration to the right of the summit is "inert" during the initial decrease of H_a, i.e. here not only does the flux line density remain fixed but its orientation also

stays stationary. Hence $E_\perp$ and $E_\parallel$ are zero in this region, denoted an O zone in the Clem nomenclature. We stress however that $J_\perp(x)$ and $J_\parallel(x)$ are not zero in this O zone but maintain their values established at the end of the preceding increase of H_a.

The phenomena occurring in the region to the left of the summit are most fascinating. First we emphasize that in our experiment, the flux lines are compelled to exit along the direction of the descending H_a which is directed at $\theta = \pi/2$ for the situation displayed in Fig 5.14. Next, we stress that $\theta(x)$ and $B(x)$ must be continuous across the surface so that $\vec{B} = \mu_o \vec{H}_a$ when the presence of surface currents is ignored.

As a consequence of these constraints, the region to the left of the peak divides into two subzones, a CT_- zone adjacent to the surface and a T_- zone sandwiched between the former and the summit. The frontier between these two zones undergoes a complicated history as H_a descends. In both zones flux becomes unpinned and migrates leftwards (outwards) down the slope of the critical B profiles. Some of the migrating flux exits across the surface and some is consumed by the flux line cutting in the CT_- zone. This flux cutting zone must arise since that is the only process whereby the flux lines which leave the specimen can change their direction from the initial orientation which they have ($\theta < \pi/2$) in the specimen, to $\theta = \pi/2$ when they emerge through the surface.

The right hand boundary of the T_- zone which coincides with the summit in the $B(x)$ profile advances to the midplane and subsequently remains fixed at that position. The left hand boundary, hence the interface between the CT_- and T_- zones initially moves to the right, then migrates leftward. The position

and migration of this boundary emerges more readily from examination of the limit of the corresponding flux cutting electric field profile, $E_{\|}(x)$, displayed on an actual scale in Fig 5.15 and on a horizontally expanded scale in Fig 5.16. Here we witness the leftward migration of this interface, hence the shrinking of the CT_- zone. The position of this interface and its leftward migration can also be observed in Fig 5.14 since it corresponds to the location where the slope in the θ profiles displays an abrupt change. Since $d\theta/dx = \mu_o J_{c\|}(B)/B$ and $J_{c\|}$ becomes very large when B is small, it is not surprising that the gradients in the θ profiles become extremely steep as H_a descends to small values and $B(x)$ in the vicinity of the surface approaches zero. Consequently, in this range, the width of the CT_- zone is minuscule, but because of its steepness it plays a major role in the sequence of θ profiles, hence in the evolution of $< B_y >$.

It is of interest to examine further the phenomena in the T_- zone which fills almost the entire specimen once the summit in the B profile has attained the midplane. Here the $\theta(x)$ profiles, hence the $J_{\|}(x)$ also, are subcritical. The flux lines decompress as some become unpinned and migrate into the CT_- zone. The drop in the sequence of θ profiles in Fig 5.14 is a consequence of this depopulation. The individual flux lines do not change orientation as they undergo displacement and become less tightly packed. This special situation where the flux lines conserve their non parallel orientation as they migrate has been investigated first by Campbell and Evetts [9] and in some detail by Lachaine and Lorrain [22]. independently of the Clem equations.

Again, for completeness, we display the sequence of $E_{\|}(x)$, $E_{\perp}(x)$, $J_{\|}(x)$, $J_{\perp}(x)$, $B_y(x)$ and $B_z(x)$ profiles in Figs. 5.15 through 5.21 corresponding to the $B(x)$ and

$\theta(x)$ profiles shown in Figs 5.13 and 5.14. In the light of our previous discussion, the reader can relate the various salient features of these families of curves, hence our comments will be brief.

The region where $E_\perp(x)$ is zero in Fig 5.17 corresponds to the inert or O zone to the right of the summit in the B profile. The subsequent diminution in the magnitude of the flux depinning electric field $E_\perp$ is a consequence of the fact that $J_{c\perp}$ increases as B decreases (also see the curves labeled 3, 4 and 5 in Fig 5.19). Thus successive decreases of H_a release smaller and smaller amounts of flux from the specimen. The discontinuities in $J_{c\perp}$ are associated with the changes in the sign of the slope on the left and right of the summit in the B profile. The discontinuities in $J_\parallel$ occur at the interface between the CT_- and T_- zones. We stress that $J_\parallel$ is subcritical in the T_- zone and decreases in magnitude in this zone as the lattice of non parallel flux lines permeating it decompresses. In the inert zone of curves 1 and 2 of Fig 5.18, $J_\parallel$ is critical and persists at the intensity established at the final stage of the previous application of H_a.

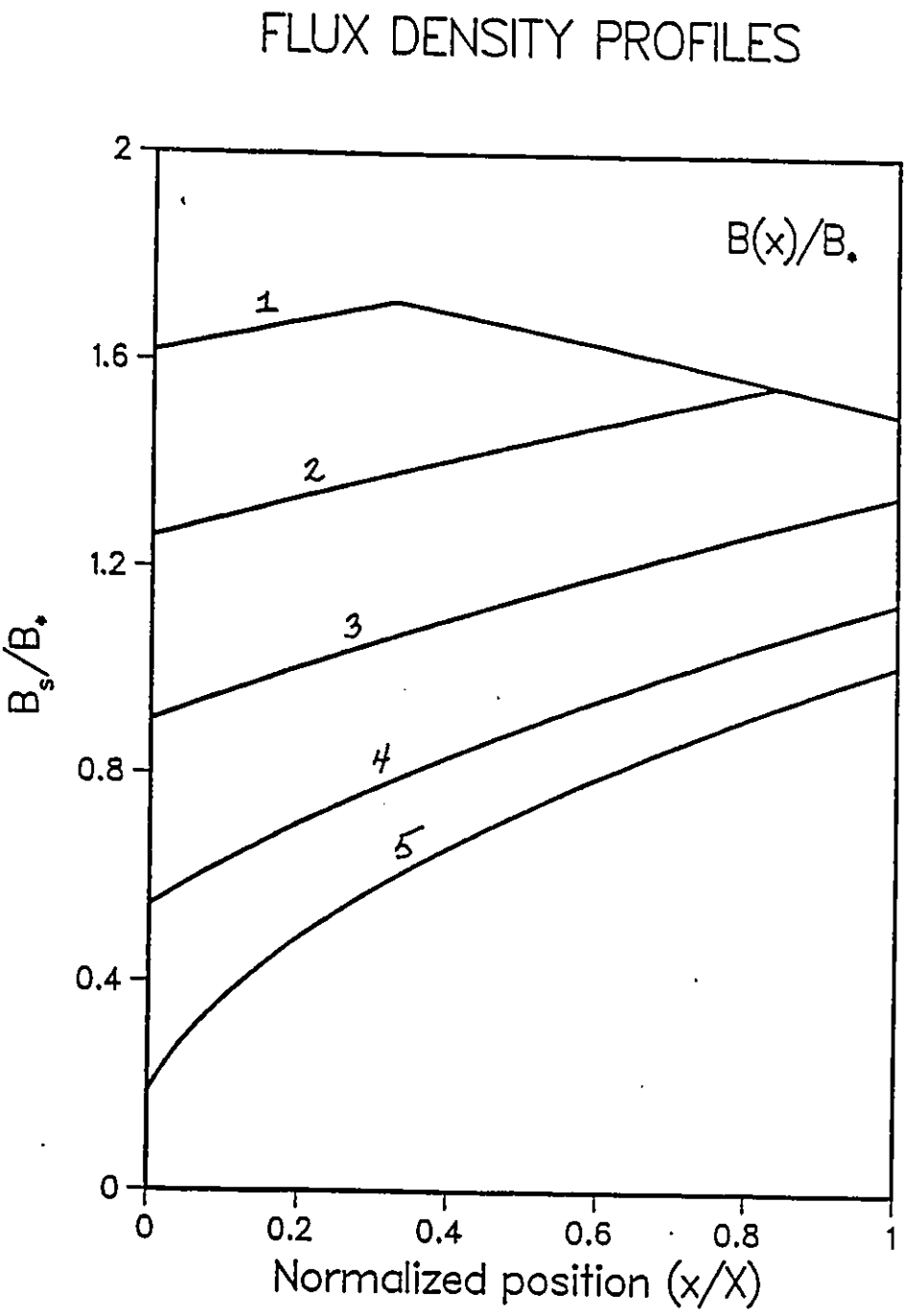

Figure 5.13: Sequence of magnetic flux density profiles as H_a decreases.

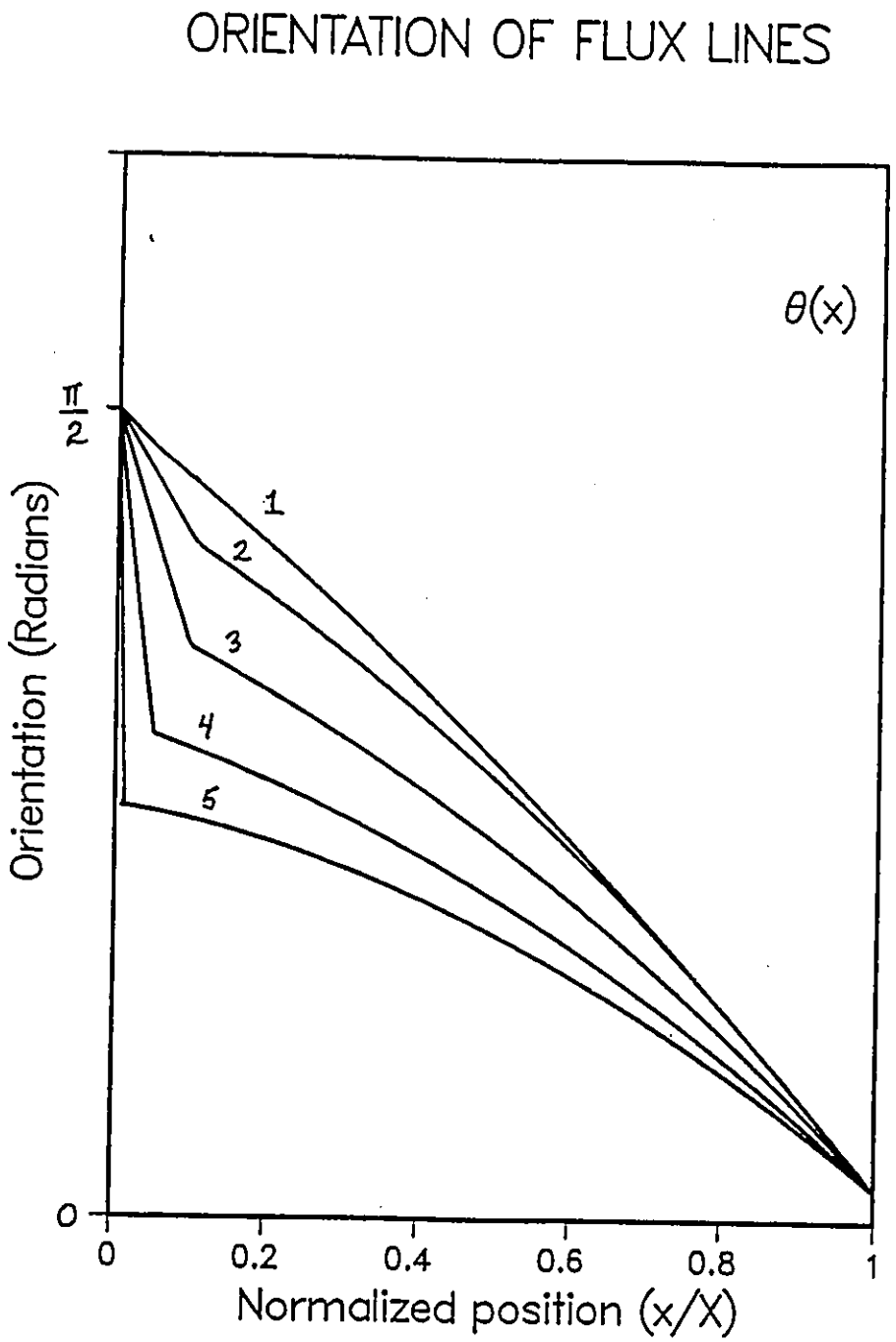

Figure 5.14: Sequence of the profiles depicting the orientation of the flux lines as H_a decreases.

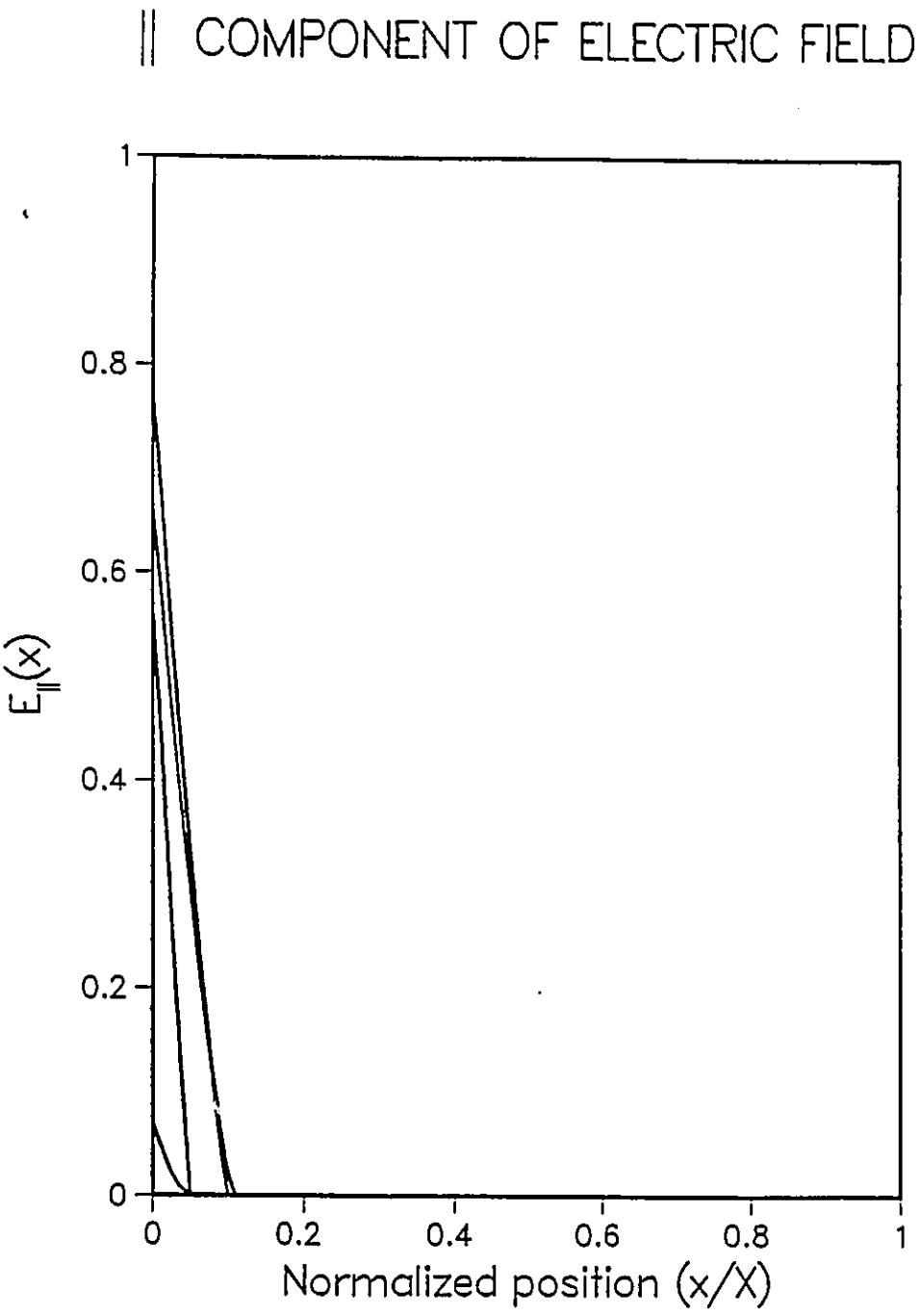

Figure 5.15: Evolution of $E_{\|}(x)$ as H_a decreases.

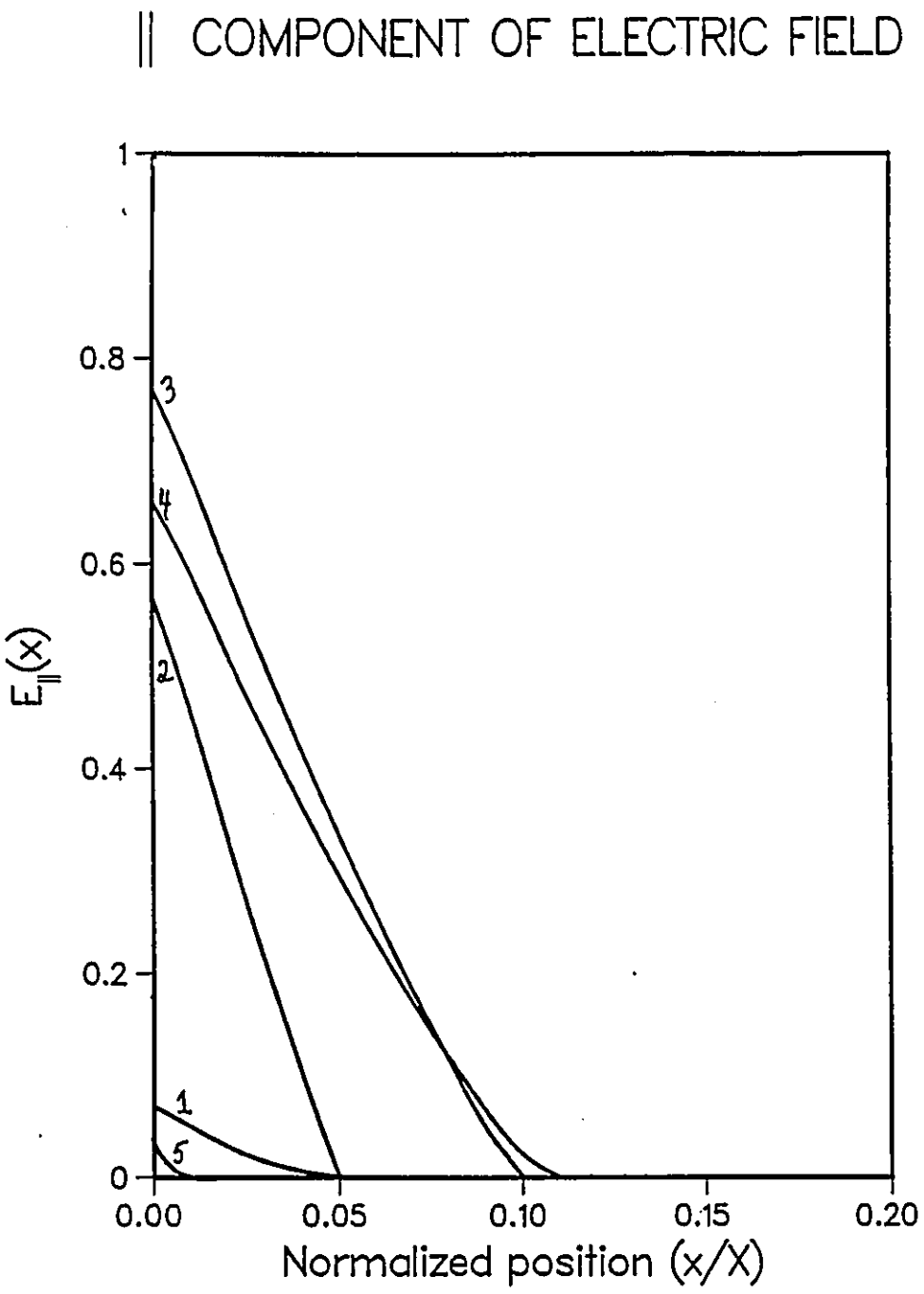

Figure 5.16: Evolution of $E_{\parallel}(x)$ as H_a decreases (horizontal scale expanded).

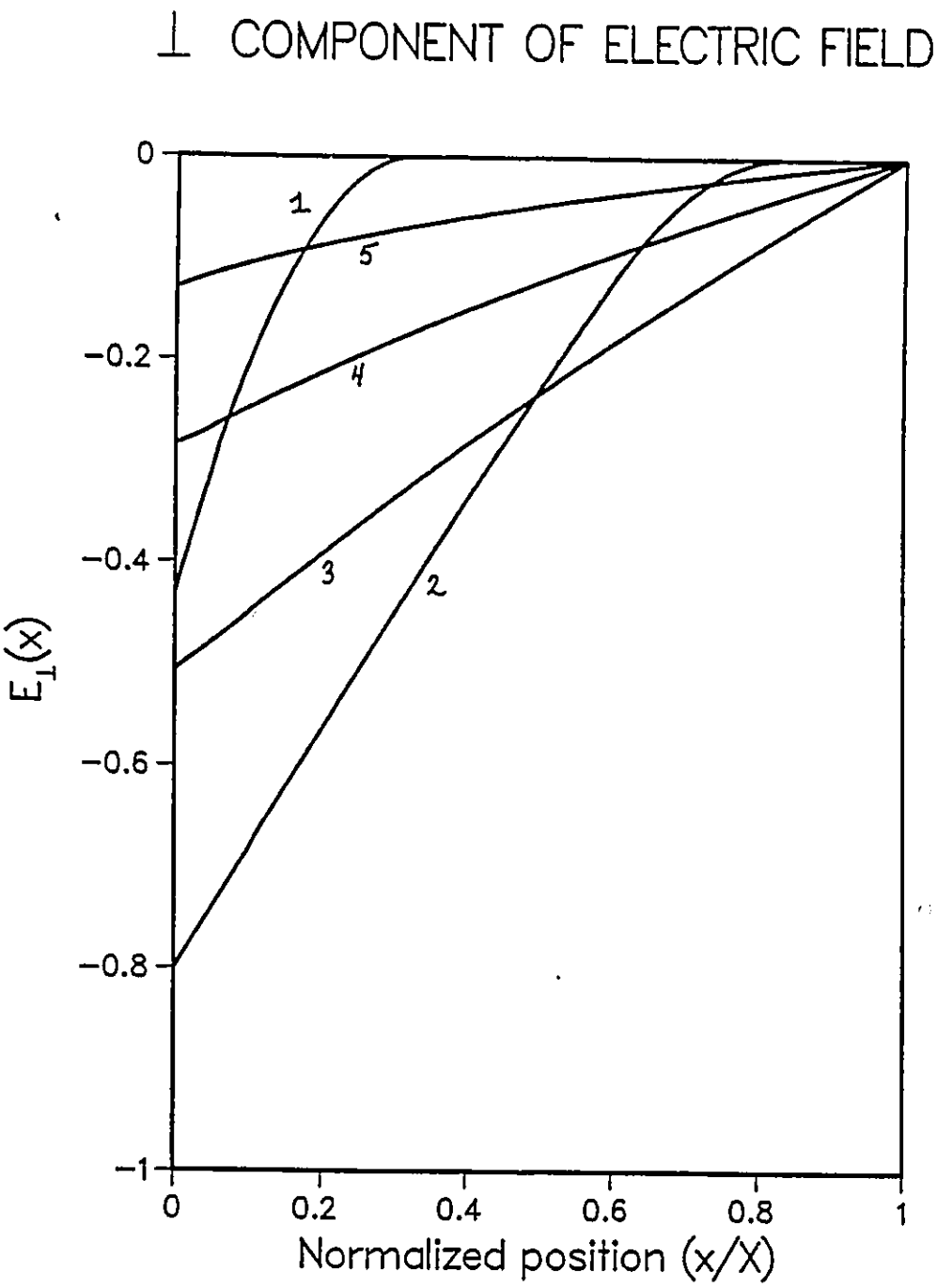

Figure 5.17: Evolution of $E_\perp(x)$ as H_a decreases.

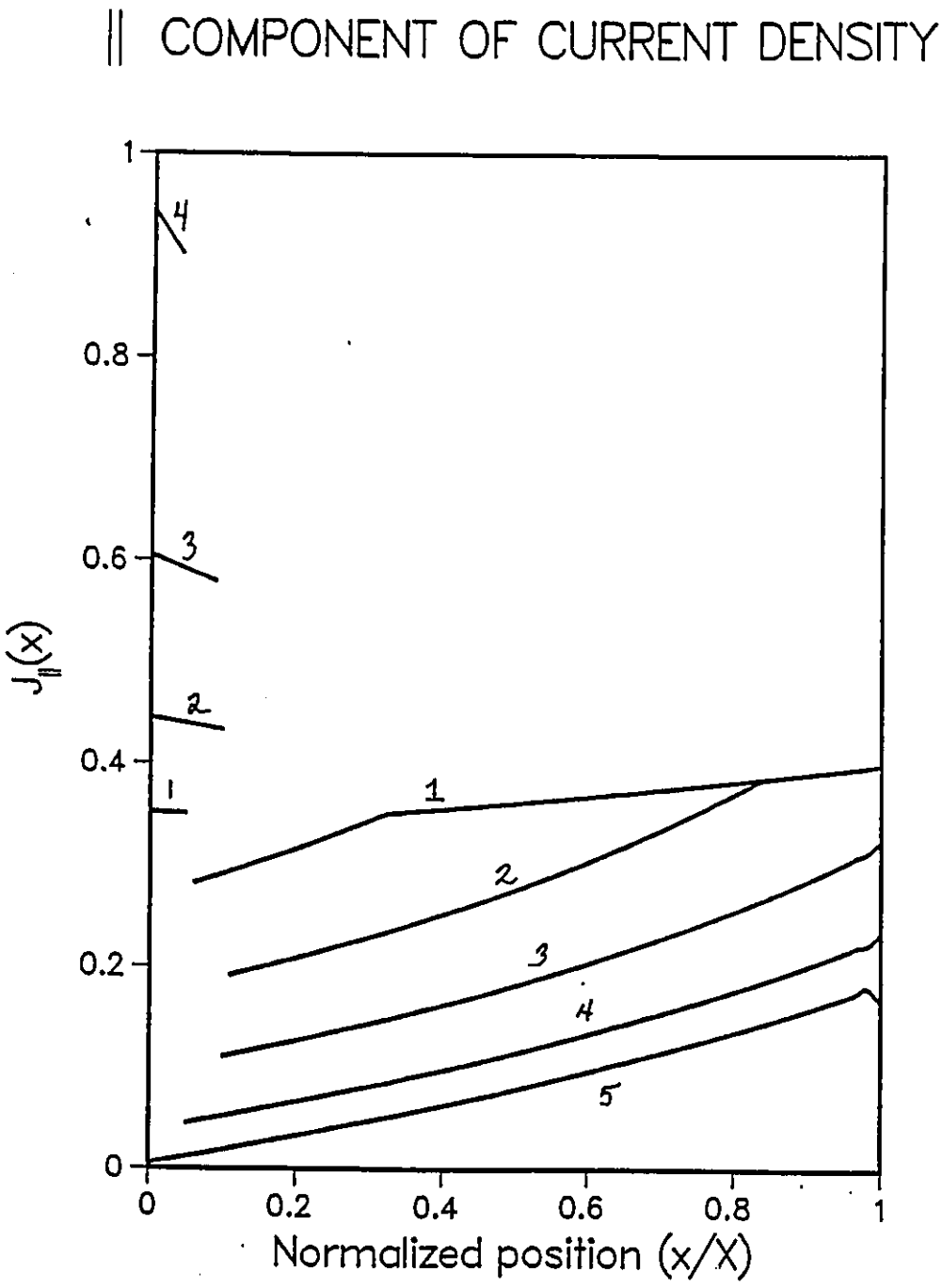

Figure 5.18: Evolution of $J_{\parallel}(x)$ as H_a decreases.

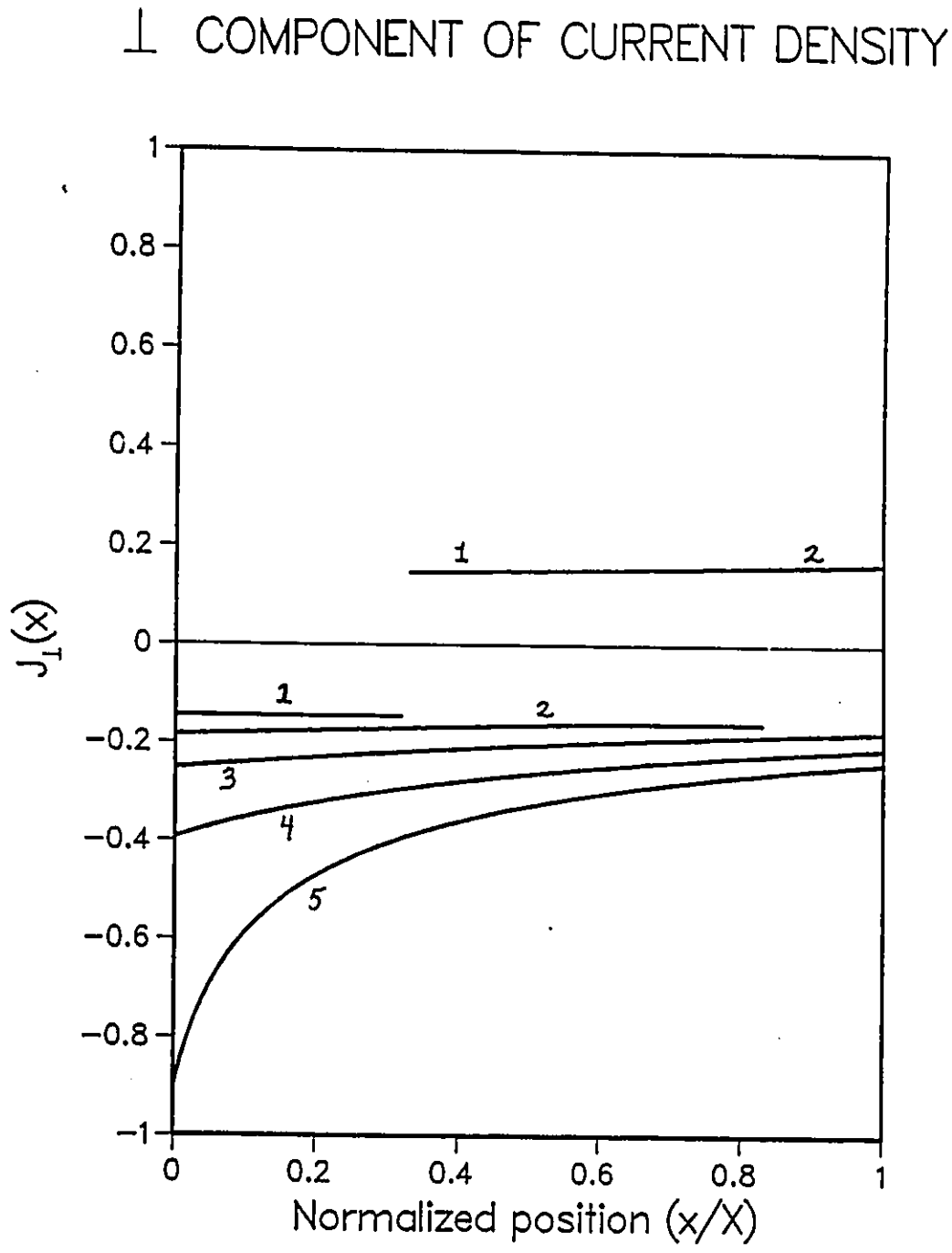

Figure 5.19: Evolution of $J_\perp(x)$ as H_a decreases.

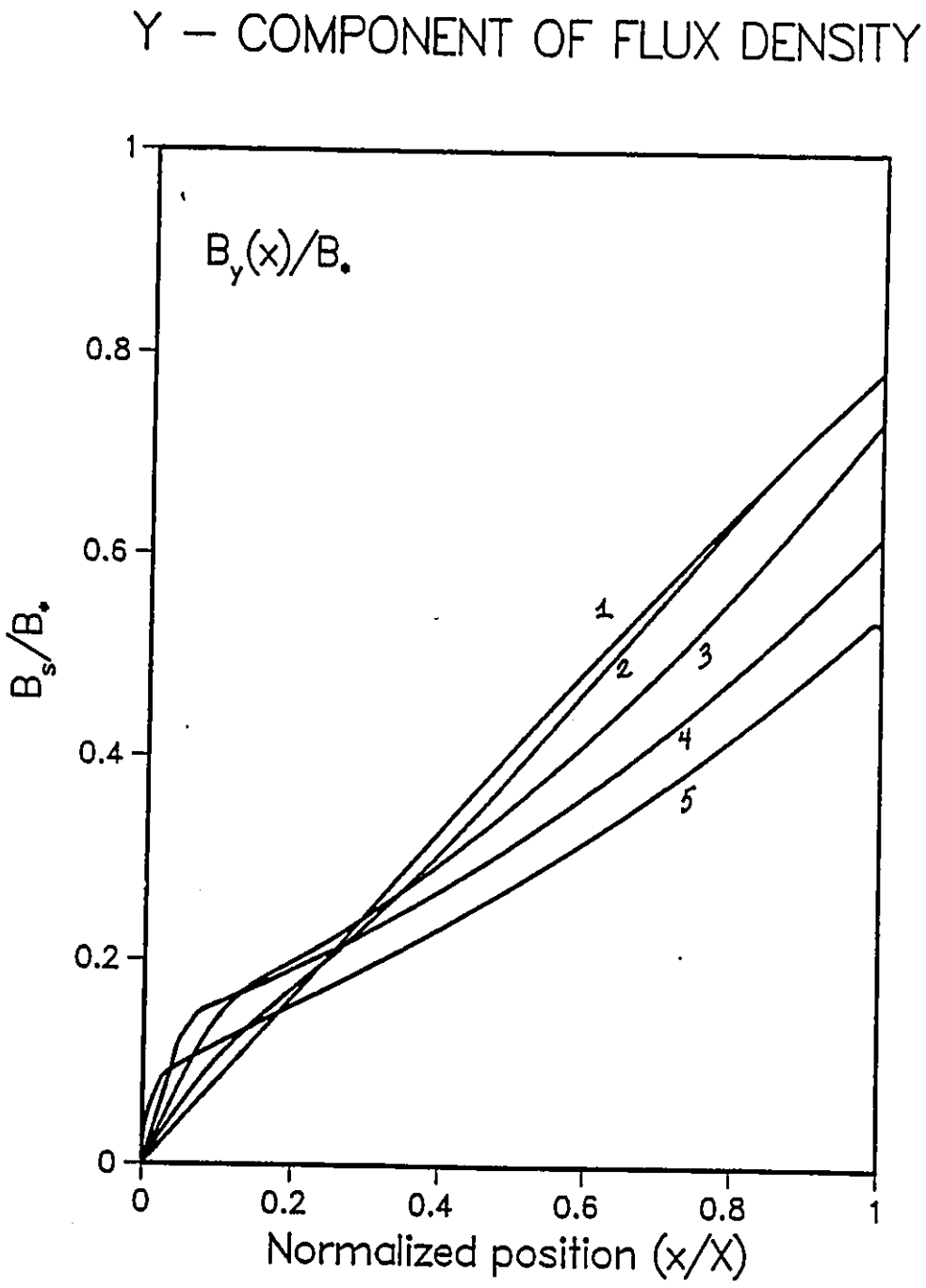

Figure 5.20: Evolution of $B_y(x)$ as H_a decreases.

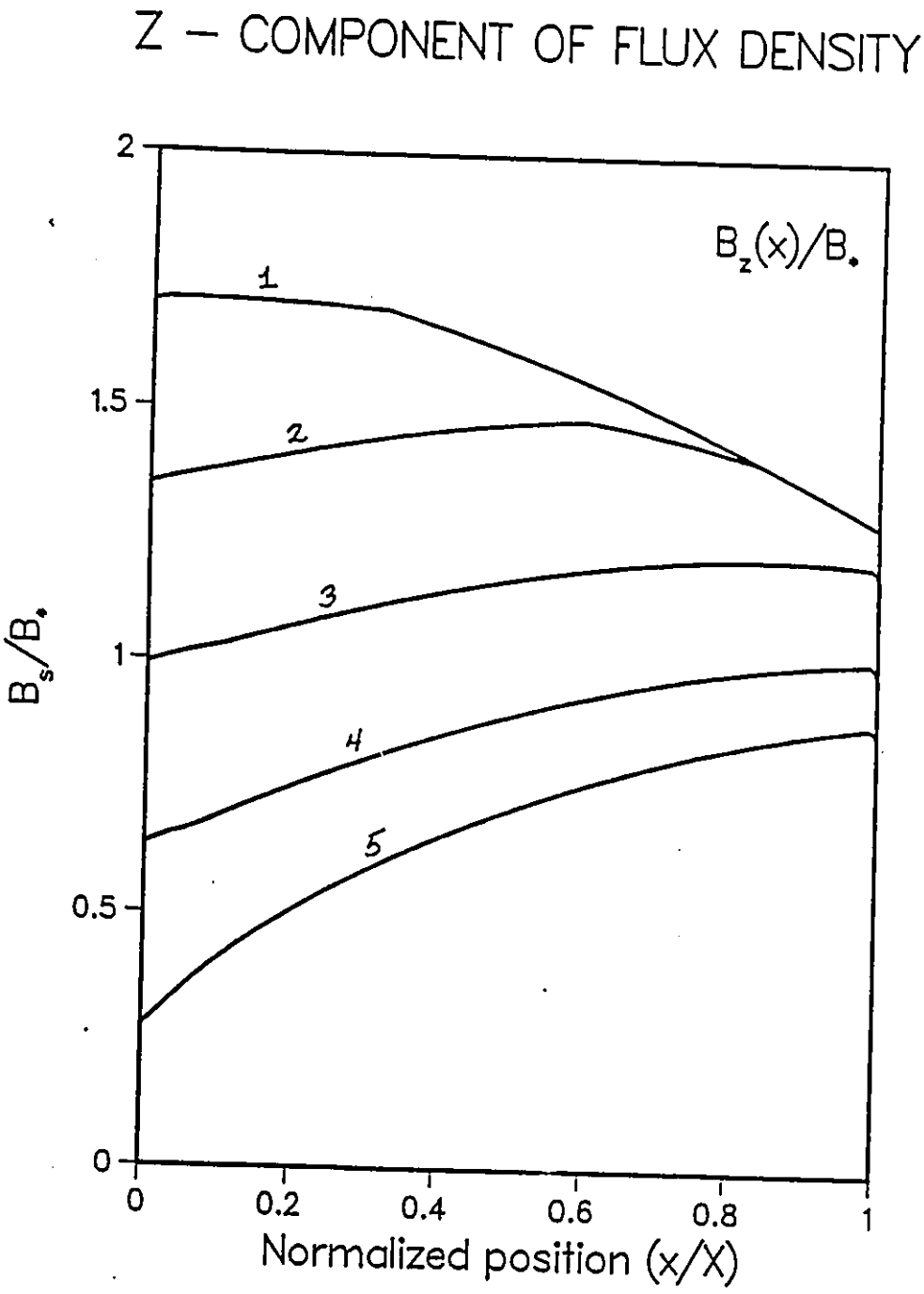

Figure 5.21: Evolution of $B_z(x)$ as H_a decreases.

5.6 Evolution of $< B_y >$ vs H_a

The fascinating sequences of configurations of magnetic flux density $\vec{B}(x)$, electric field $\vec{E}(x)$ and current density $\vec{J}(x)$ generated by the theoretical picture are unfortunately not easily amenable to direct experimental scrutiny. The macroscopic quantities which we can readily monitor are the evolution of the spatial averages of the components of the magnetic flux density along and transverse to $\vec{H}_a$, namely $< B_z >$ and $< B_y >$. As noted earlier, the locus of $< B_z >$ vs H_a is not sensitive to the orientation of the trapped flux, hence does not provide a severe test of the model. Fortunately, $< B_y >$, the component of the trapped flux orthogonal to H_a, is dramatically affected by the application and subsequent removal of H_a. Consequently, in the remainder of this chapter, we compare predictions of the model for the behaviour of this important quantity with observations.

In addressing such a comparison we are confronted by a dilemma. We have at our disposal a wealth of experimental data on three different materials, Nb, PbBi and $YBa_2Cu_3O_{7-x}$ (the PbBi data was assembled by Sekerka). In chapter 3 we displayed a small representative selection from our large catalogue. We also have available a huge compilation of corresponding theoretical curves generated by our computer program of the Clem model. In both cases we have examined, (i) the effect of the amplitude of the sweep of H_a relative to H_* (H_{**}) and H_{c2}, and (ii) the dependence on the angle of rotation of the trapped flux (45°, 90° and 135°). The effect of repeated application of H_a at various selected amplitudes has not yet been pursued theoretically. We have however investigated :

(a) the crucial role of the ratio of $J_{c\parallel}$ to $J_{c\perp}$, and,

(b) the effect of different dependences of $J_{c\perp}$ (hence $J_{c\parallel}$) on B, namely $J_{c\perp} = \pm\alpha/B^n$ where $n = 0, 1/2$ and 1 (Bean, Yasukochi and Kim approximations).

Evidently, a difficult choice needs to be made on which results to present and compare. For conceptual simplicity we have focused on the situations where the trapped flux has been rotated through 90°. On the theoretical side we confine our presentation to the curves obtained exploiting the Kim approximation, since these best reproduce the observations.

To assist the reader in pursuing this comparison we first display the pertinent experimental data on the three materials studied to date in Figs 5.22, 5.23 and 5.24. Then we present a series of corresponding theoretical curves. The latter figures comprise two distinct groups.

The first group, Figs 5.25, 5.26 and 5.27, display the effect of the ratio of $J_{c\parallel}$ to $J_{c\perp}$ on the behaviour of $< B_y >$ vs H_a when H_{c2} is extremely large (infinite) compared with H_a and H_*. This is the situation which prevails for the data on the $PbBi$ and $YBa_2Cu_3O_{7-x}$ specimens. Consequently, this group of figures should be examined together with Figs 5.22 and 5.23. This comparison shows that the choice of $J_{c\parallel}/J_{c\perp} = 1$ leads to a good reproduction of the observations on the high T_c material and the choice $J_{c\parallel}/J_{c\perp} = 3$ to a good fit for the behaviour of the $PbBi$ sample.

In the second group of theoretical results, we have taken H_{c2} into account and introduced $H_{c2} = 2H_*$. This approximate value emerges from consideration of the standard magnetization curve of the Nb specimen. Consequently the second group of theoretical curves should be compared with the data on this sample (Fig 5.24).

As noted earlier, the magnetic moment of Nb displays an abrupt decline near

H_{c2}, indicating a rapid decrease of $J_{c\perp}$ in this range. Consequently, standard approximations for the dependence of $J_{c\perp}$ on B such as,

$$J_{c\perp} = \pm\frac{\alpha}{B}\,(1 - \frac{B}{B_{c2}}) \tag{5.13}$$

are inadequate to describe the behaviour in this range although they apply remarkably well below this critical region. This feature of the standard magnetization curve has a profound effect on our observations near H_{c2}. This is evident from the sharp descent of $< B_y >$ vs H_a just below H_{c2} in Fig 5.24. It is therefore necessary that we somehow model such a sudden variation of $J_{c\perp}$, hence $J_{c\parallel}$, in this range. We have elected to do this by introducing a coefficient m in the factor containing B_{c2}, thus letting,

$$J_{c\perp} = \pm\frac{\alpha}{B}\,(1 - (\frac{B}{B_{c2}})^m) \tag{5.14}$$

$$J_{c\parallel} = \frac{k}{B}\,(1 - (\frac{B}{B_{c2}})^m) \tag{5.15}$$

in our analysis, with $m \gg 1$.

Fig 5.28 displays the effect of letting $m = 4, 10$ and 40 on the calculated locus of $< B_y >$ vs H_a increasing to $H_{c2} = 2H_*$ when $J_{c\parallel}/J_{c\perp} = 3$. This figure indicates that the closer the dependence of $J_{c\perp}$ and $J_{c\parallel}$ on B approaches to a step function, the better the correspondence with observations. Figs 5.29 and 5.30 complement Fig 5.28 by displaying the calculated behaviour when H_a is removed after a sweep to various values ranging up to H_{c2}, taking $m = 4$ and $m = 40$ respectively. Although the latter of these figures shows fair agreement with the

data on the Nb sample (Fig 5.24), it is clear from inspection that the descent of $< B_y >$ is too slow in the intermediate range of H_a both as H_a is increasing and when it is being removed. This feature suggests that the choice of $J_{c\|}/J_{c\perp}$ is a bit too small. Consequently the calculation was repeated with $J_{c\|}/J_{c\perp} = 4$ and the results are displayed in Fig 5.31. In our view these theoretical curves show excellent agreement with the observations on the Nb specimen (Fig 5.24).

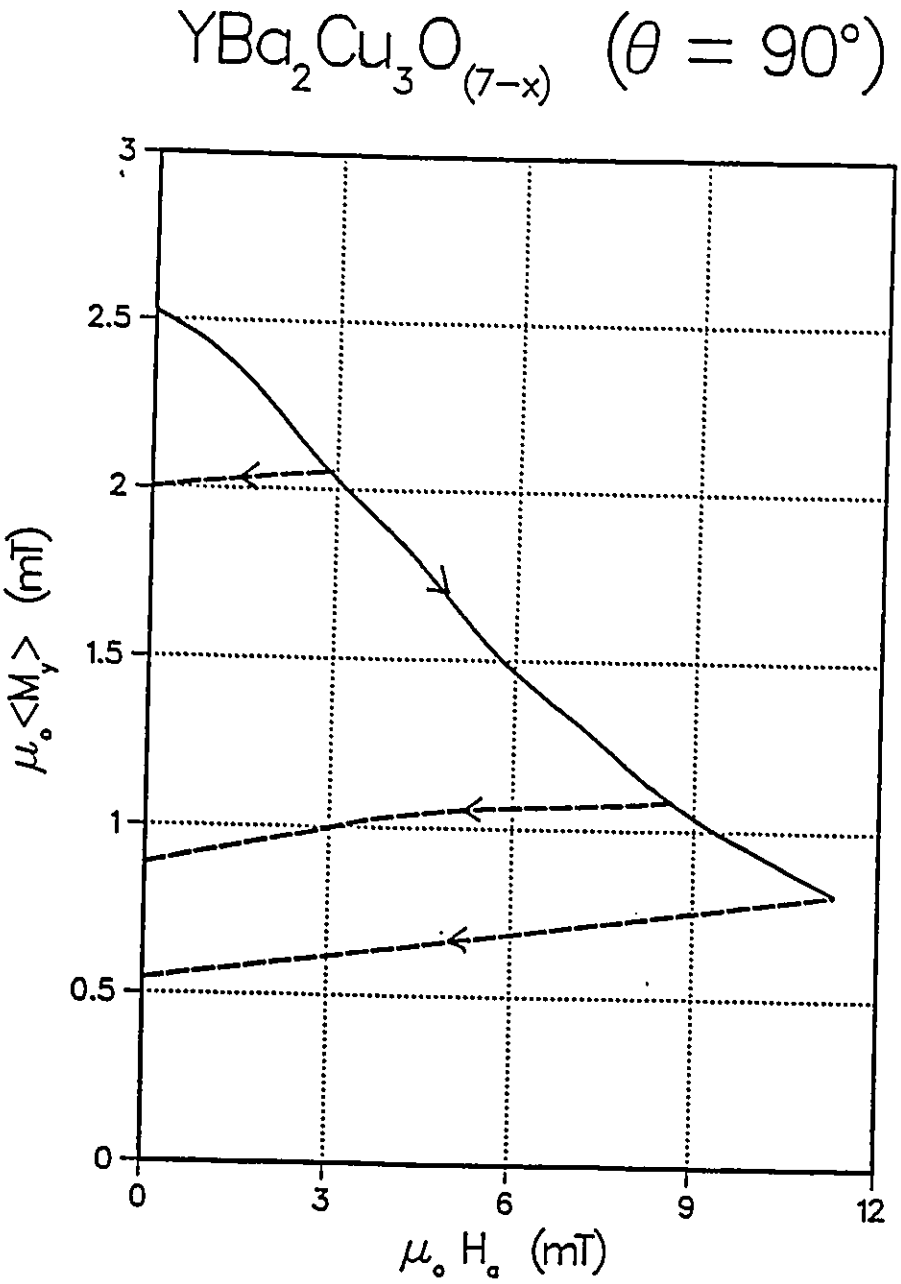

Figure 5.22: $< B_y > \equiv \mu_o < M_y >$ vs H_a for $YBa_2Cu_3O_{7-x}$.

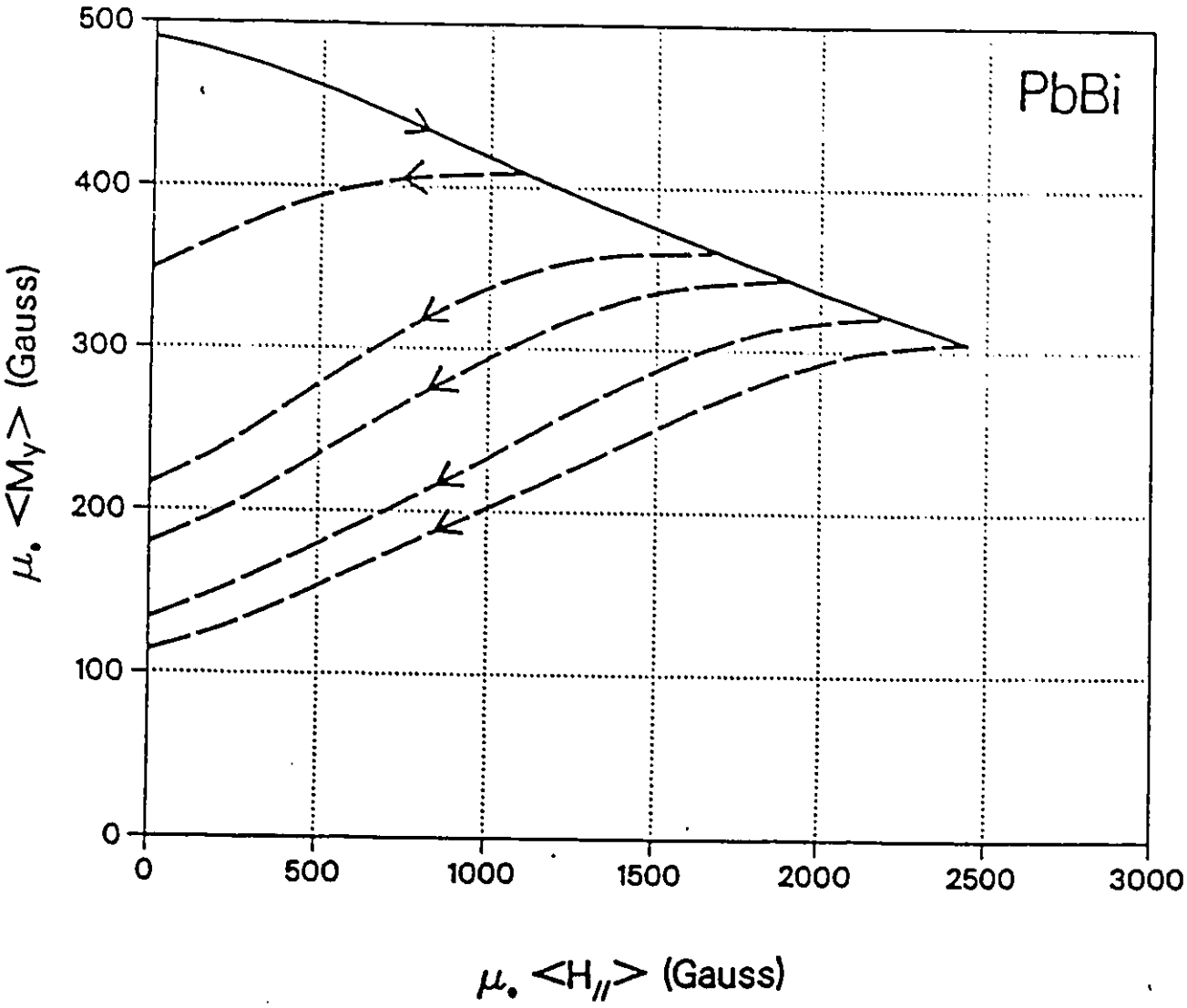

Figure 5.23: $< B_y > \equiv \mu_o < M_y >$ vs H_a for $PbBi$.

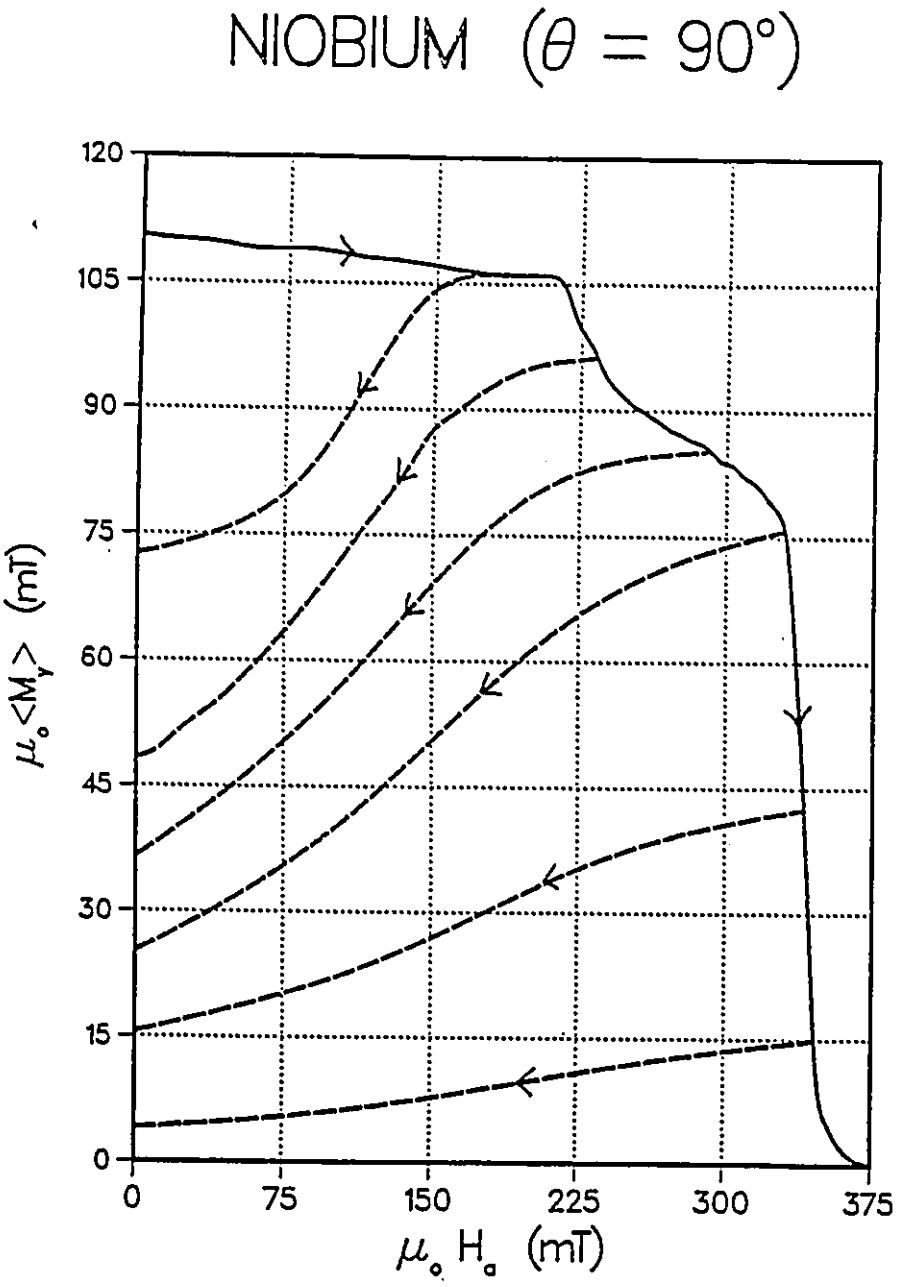

Figure 5.24: $< B_y > \equiv \mu_o < M_y >$ vs H_a for Nb.

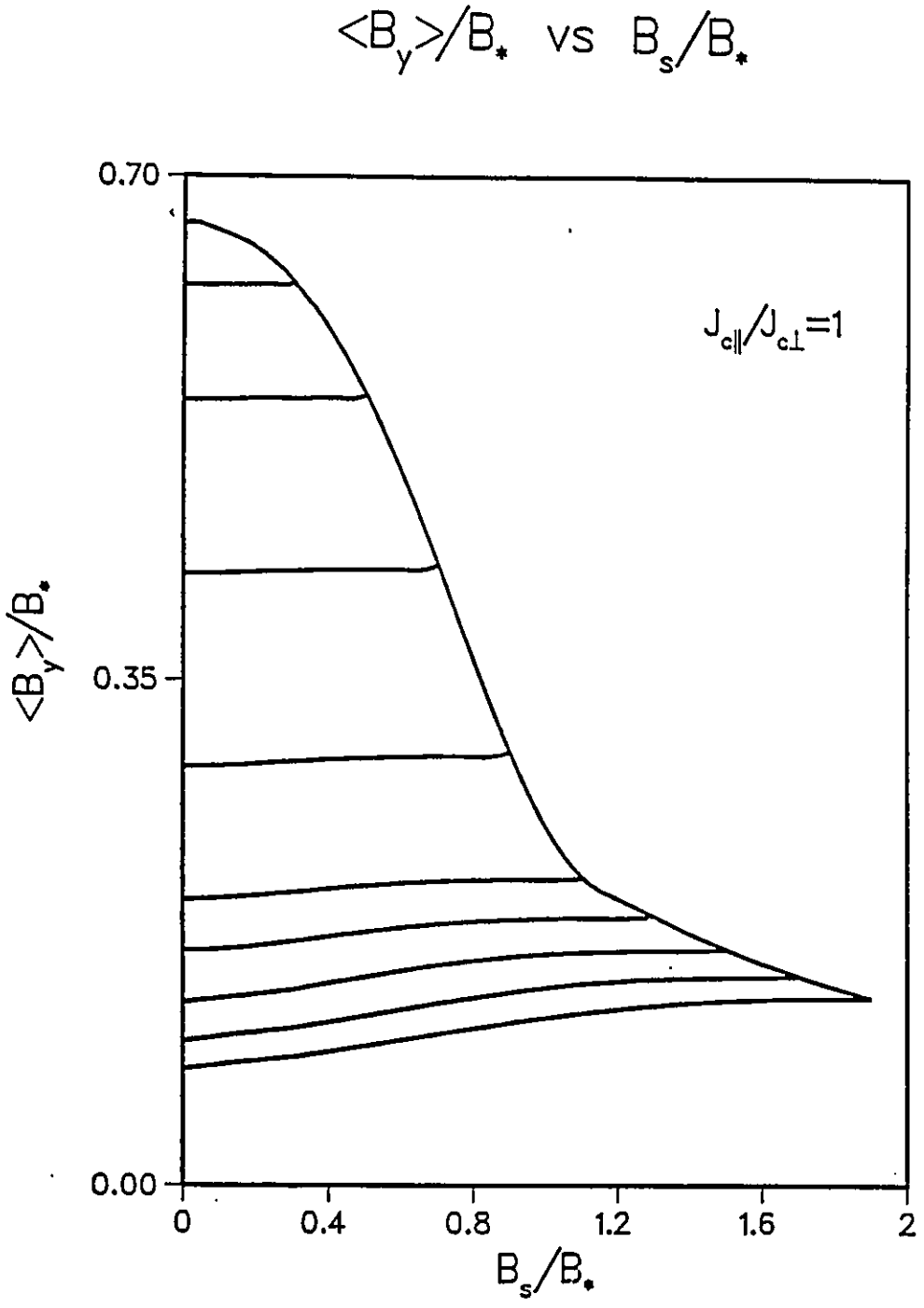

Figure 5.25: Theoretical curves of $< B_y >$ vs B_s for $\frac{J_{c\parallel}}{J_{c\perp}} = 1$ and H_{c2} infinite.

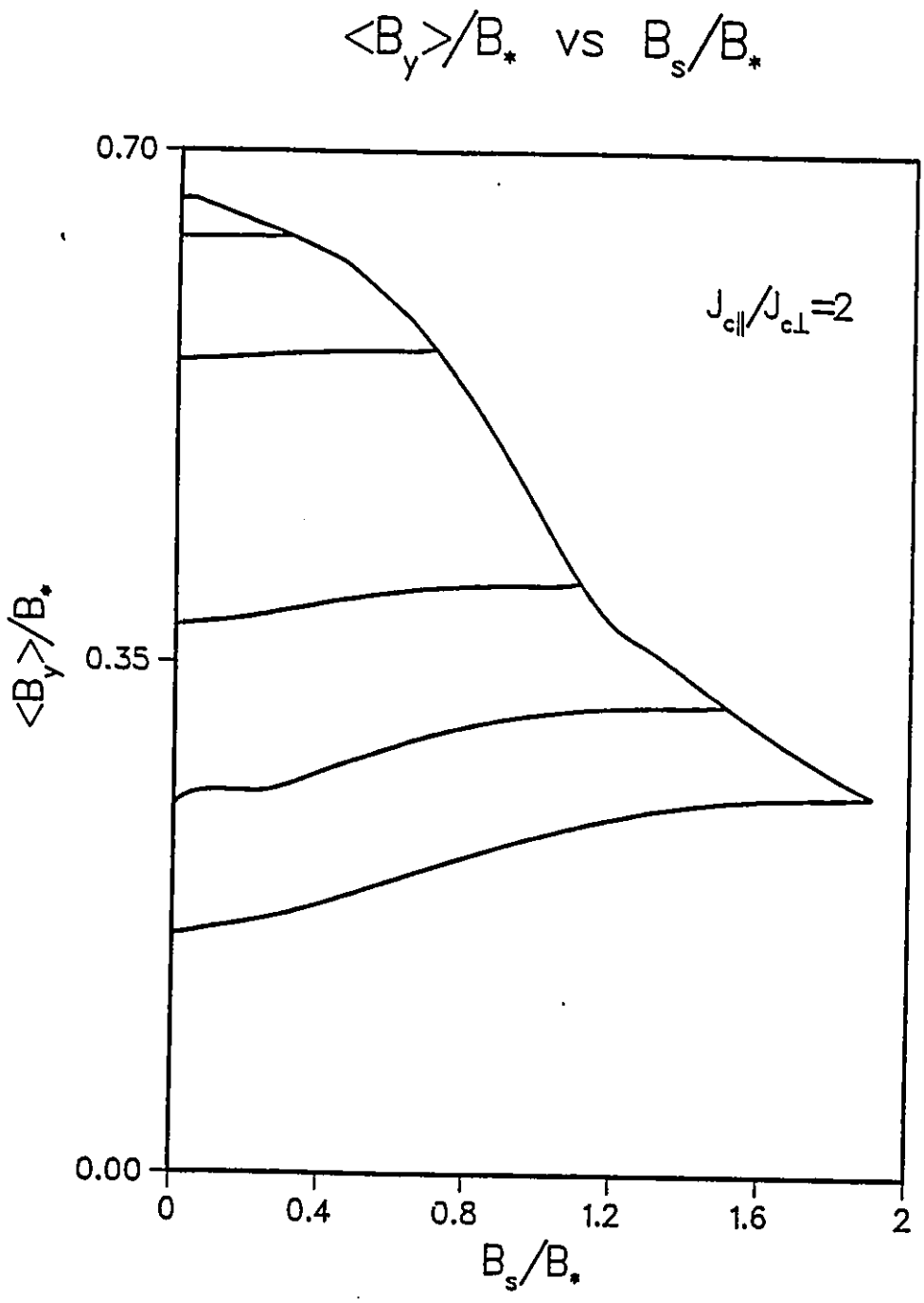

Figure 5.26: Theoretical curves of $< B_y >$ vs B_s for $\frac{J_{c\|}}{J_{c\perp}} = 2$ and H_{c2} infinite.

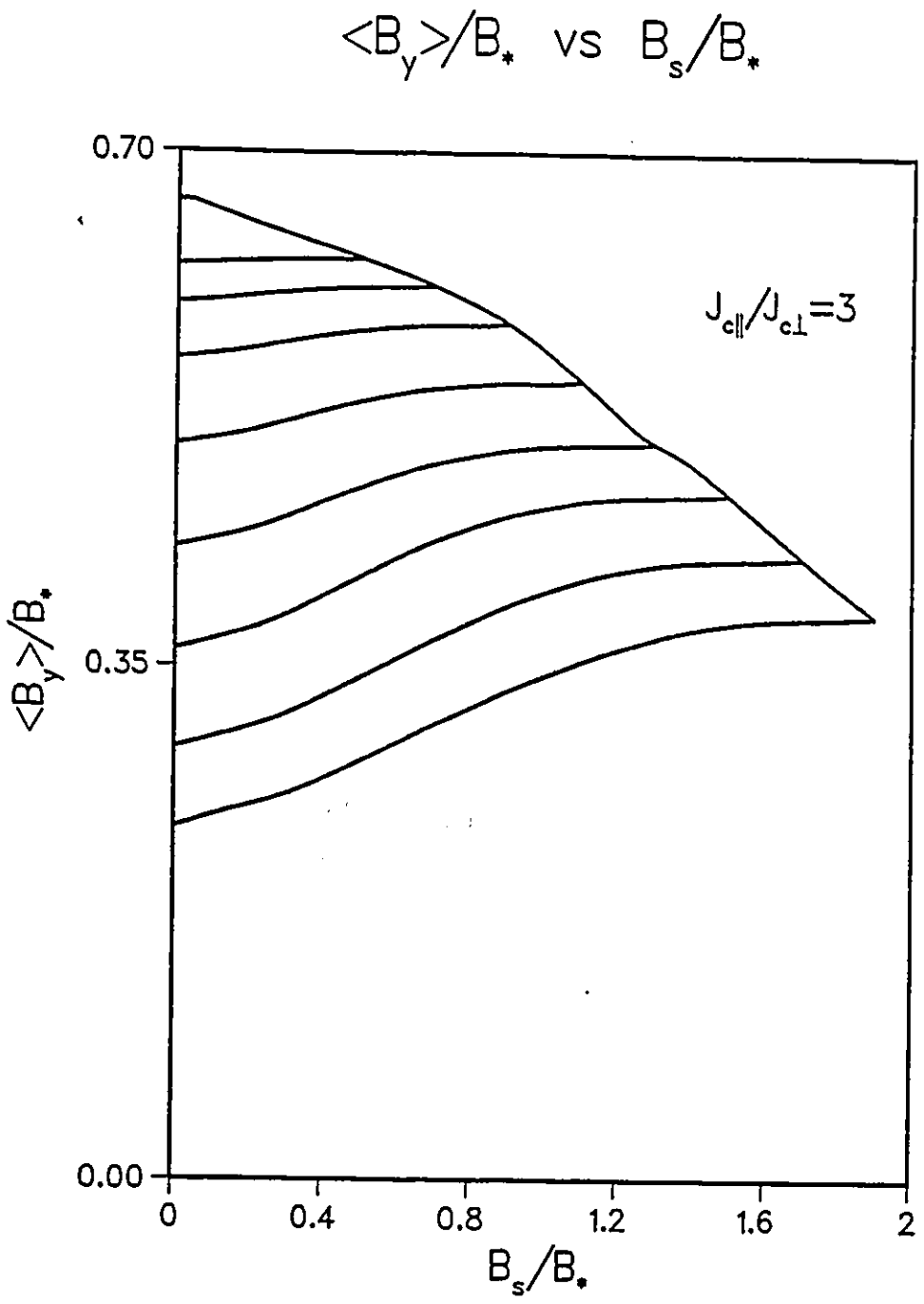

Figure 5.27: Theoretical curves of $< B_y >$ vs B_s for $\frac{J_{c\|}}{J_{c\perp}} = 3$ and H_{c2} infinite.

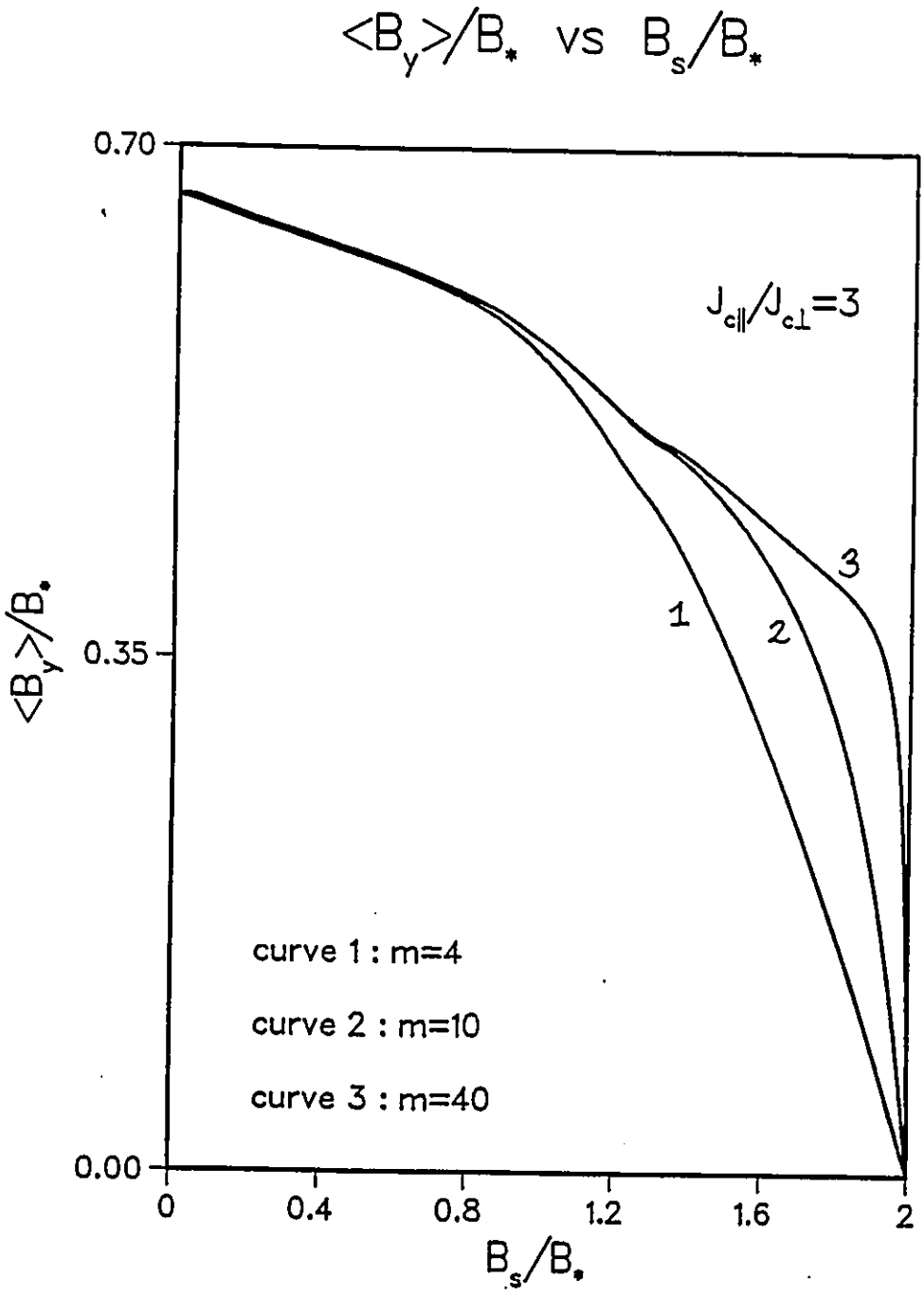

Figure 5.28: Theoretical curves of $< B_y >$ vs B_s as H_a is increased from zero to $H_{c2} = 2H_*$ ($\frac{J_{c\|}}{J_{c\perp}} = 3$).

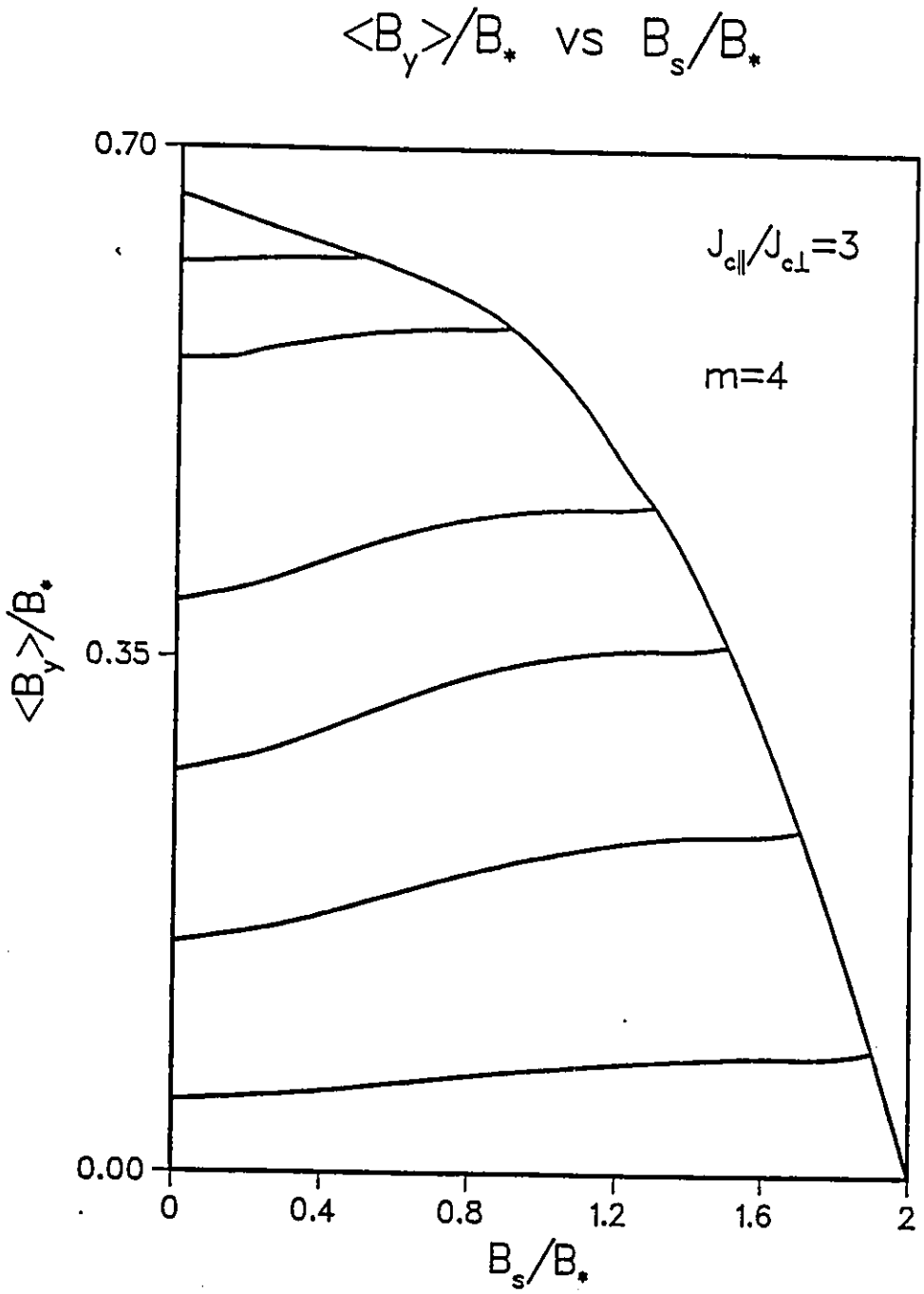

Figure 5.29: Theoretical curves of $< B_y >$ vs B_s as H_a is cycled once between zero and an arbitrary field $H_a < H_{c2}$ (m=4 and $\frac{J_{c\parallel}}{J_{c\perp}} = 3$).

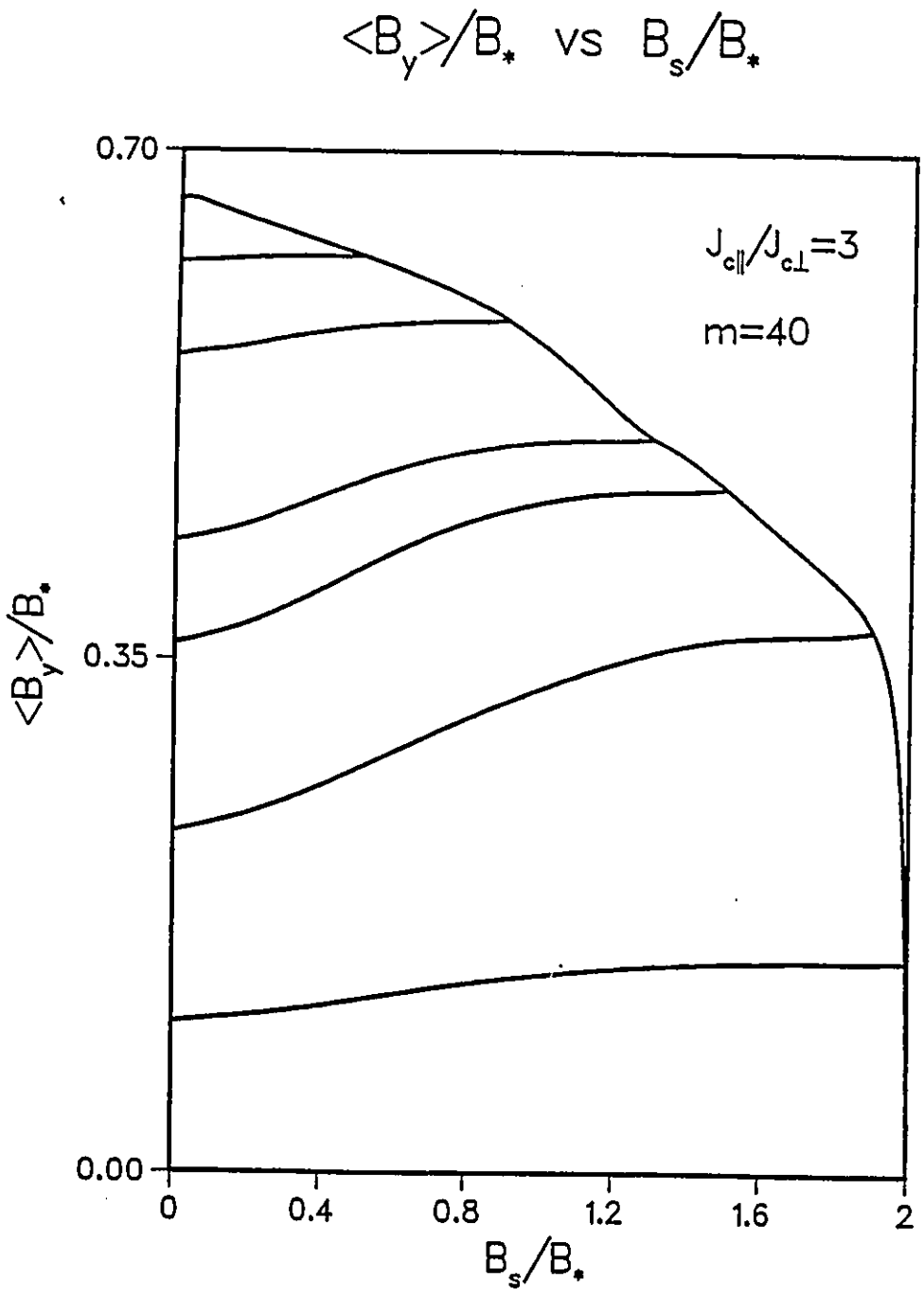

Figure 5.30: Theoretical curves of $< B_y >$ vs B_s as H_a is cycled once between zero and an arbitrary field $H_a < H_{c2}$ (m=40 and $\frac{J_{c\parallel}}{J_{c\perp}} = 3$).

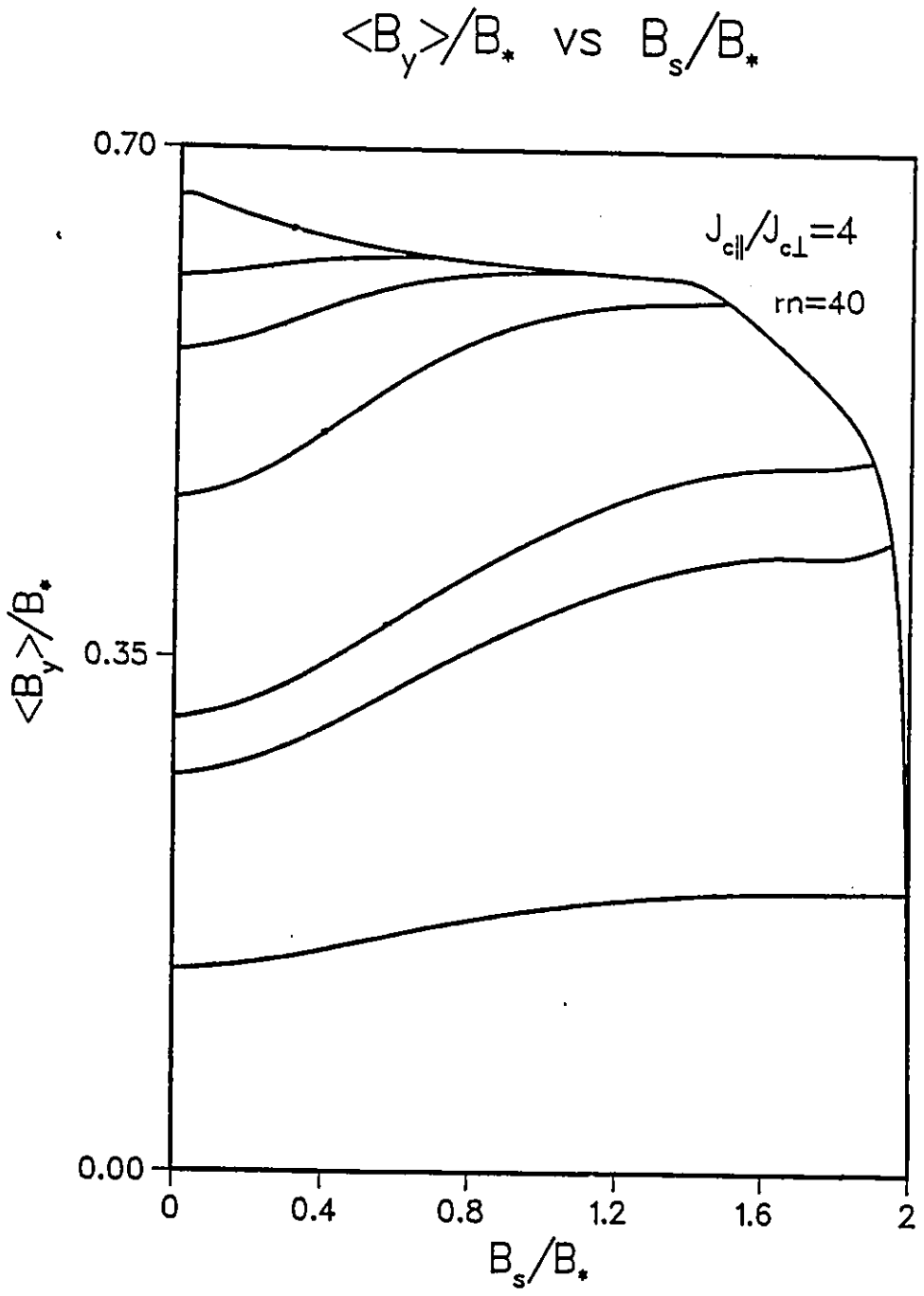

Figure 5.31: Theoretical curves of $< B_y >$ vs B_s as H_a is cycled once between zero and an arbitrary field $H_a < H_{c2}$ (m=40 and $\frac{J_{c\parallel}}{J_{c\perp}} = 4$).

5.7 Conclusion

The interaction of lattices of non parallel (tilted) flux lines has been investigated using a novel approach. Flux lines oriented along a fixed direction ($\vec{H}_a$ along the z axis) are injected into a specimen containing a lattice of parallel trapped flux lines tilted at some angle θ (eg $\theta = 90°$) with respect to $\vec{H}_a$. The ensuing evolution of the magnetic moment of the sample as H_a is increased, up to H_{c2} in some cases, is monitored. The change in the magnetic moment is also observed when flux lines are made to exit from the specimen along the direction of $\vec{H}_a$ as the latter is reduced to zero.

The phenomena encountered in these circumstances have been analyzed in the framework of the Clem phenomenological generalized critical state model. This model takes into account both flux line cutting and flux line depinning processes. These two mechanisms operate in the situation we have explored experimentally.

A comparison of a large variety of experimental and theoretical curves show that the model reproduces all of the salient features of the several observations on three different materials ($YBa_2Cu_3O_{7-x}$, $PbBi$ and Nb).

In the analysis, we stipulated that $J_{c\|}$ and $J_{c\perp}$, the flux line cutting and flux line depinning critical current densities obey the same dependence on B. The agreement between the theoretical predictions and the data appear to confirm this crucial assumption. An excellent correspondence between calculated and measured curves was achieved by taking $J_{c\|}/J_{c\perp} = 1$ for the high T_c material, $J_{c\|}/J_{c\perp} = 3$ for the $PbBi$ and $J_{c\|}/J_{c\perp} = 4$ for the Nb sample. We stress that our measurements on the Nb sample covered the entire range of H_a up to H_{c2}.

Chapter 6. MAGNETIC FLUX IN ROTATING DISKS

6.1 Introduction

The $YBa_2Cu_3O_{(7-x)}$ sample previously employed for measurements described in chapter 2 was used to further investigate the flux interaction phenomena.

In this work, the disk is rotated in a static externally applied field H_a. The rotation dramatically alters the configuration of the magnetic flux and induces persistent currents to circulate in the disk. These persistent currents flow with a component both along the direction of the applied field, $J_{\|}$, and perpendicular to it, $J_{\perp}$. The evolution of the components of the magnetization as the disk is rotated through selected angles is continuously monitored.

The experimental arrangement presented in chapter 2 and the one employed in the present work are similar in all aspects but one. Here the X axes of the X—Y recorders were driven by a signal proportional to the angle of rotation instead of the applied field. This signal was generated by a constant voltage across a potentiometer. The experimental procedure is now described.

6.2 Experimental Procedure

The disk, initially in the normal state, is allowed to cool from its critical temperature in a selected static magnetic field. Some of the flux initially permeating the specimen is expelled as the state changes from normal to superconducting (Meissner effect). The initial magnetization acquired by the disk through this process is registered. The specimen is then slowly rotated and the magnetization, both along (z-axis) and perpendicular (y-axis) to the applied field, are continuously monitored. The rotating process is continued until a peak is observed in the magnetization curve. Once the rotation is completed, the sample is driven in the normal state, thereby erasing the magnetic history acquired by the disk as it rotated. The resultant magnetization is also registered. This entire procedure is then repeated for various selected fields in the range $0\ mT < H_a < 60\ mT$. Sketches of typical magnetization curves obtained in the experiments and their salient features are displayed in figure 6.1.

The calibration of both components of the magnetization was performed as described in chapter 2. The calibration of the signal along the x axis, corresponding to the angle of rotation, was performed as follows.

Magnetic flux was trapped in the disk by either, (i) subjecting it in the superconducting state to a sweep of magnetic field H_a of magnitude well above H_{c1} or, (ii) letting the sample become superconducting in a static field H_a by cooling it below its critical temperature. The components of the magnetization along z and y are monitored as the disk was then subjected to continuous rotation. The $< M_z >$ signal maps out a cosine curve while the $< M_y >$ signal generates a sine

curve as the rotation of the trapped magnetic moment proceeds from the z-axis through the y-axis, then toward the negative z direction and so on. For each curve, the horizontal distance (along the x axis of the recorder) separating the maxima corresponds to one full revolution. A relationship between the angle of rotation, the potentiometer signal and the horizontal travel of the recorder is thus established.

6.3 General Background

We now present a brief qualitative description of the behaviour of the flux lines in the rotating disk. The reader is referred to Sekerka's thesis [26] for a more detailed discussion. The results presented in this chapter are a continuation of the investigations reported by Boyer [5],[6], [7], Cave [10], Fillion [17] and Sekerka [26] exploiting the same experimental technique. Careful consideration of the experimental results led Boyer et al to put forward a specific picture of the evolution of the flux density in the specimen as it is rotated in a static magnetic field. He suggested that as the rotation of the sample proceeds, a valley develops and grows adjacent to each surface, in the profile of the magnetic flux density. At the time, this was considered quite revolutionary since magnetic flux must disappear or be removed from the sample in order that the valley develops. This removal seemed to require that the flux lines migrate out of the specimen against a flux density gradient and in opposition to the Lorentz force. Subsequently, Clem et al [11], [24], [15],[25], showed that the flux line cutting process generated such a valley in the configuration of the flux lines as the disk rotates.

For simplicity, let us first assume that the flux lines inside the disk rotate rigidly in unison with the specimen. As the rotation begins, new vortices parallel to H_a nucleate at the surface. The angle between these and the flux lines already present in the disk correspond to the angle of rotation, θ_R. We have seen previously (§4.4) that flux cutting between adjacent planes of vortices occurs if the angle formed between them exceeds a critical angle, θ_c. Thus, when $\theta_R = \theta_c$, flux cutting takes place between the planes of fluxons adjacent to the surface. The net result of this interaction is a reduction in the local flux density and a change in the orientation of the flux lines in the planes of vortices involved.

Now, as the rotation of the disk proceeds, more vortices nucleate at the surface and more cutting occurs. As seen in §4.4, the frontier of the zone where flux cutting processes take place between adjacent planes of fluxons will gradually migrate from the surface toward the midplane.

6.4 Experimental Results

Several salient features emerge from inspection of the curves displaying the evolution of $< M_z >$ and $< M_y >$ as the disk is rotated in various static magnetic fields. The maxima in the components of the magnetization acquired by the disk as it revolved are of special interest. This feature is determined for each magnetization curve ($< M_z >$ and $< M_y >$ vs θ) for different static applied fields H_a. The magnitude of $< M_y >$ and $< M_z >$ at these maxima (denoted $< M_z >_{max}$ and $< M_y >_{max}$) are then catalogued and graphed as a function of H_a. Also of interest is the angle of rotation at which each component of the magnetization reaches its

peak. These are denoted θ_z and θ_y respectively. These are also measured, catalogued and graphed as a function of H_a. The results are presented in figures 6.2 through 6.5.

6.5 Comments on the Observations

Inspection of the dependence of $< M_z >_{max}$ and $< M_y >_{max}$ on H_a reveals the following salient features.

- The magnitudes of $< M_z >_{max}$ and $< M_y >_{max}$ vs H_a both display a pronounced peak.
- The peak in the $< M_z >_{max}$ curve is found at a slightly lower field than the peak in the $< M_y >_{max}$ curve.
- The applied field at which these maxima are found correspond to approximately 6 mT or $H_s/2$.
- The ratio of the peak values of $< M_z >_{max}$ to $< M_y >_{max}$ is found to be approximately 1.7.
- The ratio $|< M_z >_{max}|$ / $< M_y >_{max}$ diminishes with H_a, and varies from greater than one to below unity.

A detailed theoretical analysis of these rotating disk phenomena is presented in Sekerka's thesis. Amongst his accomplishments, he successfully related the evolution of the ratio of $< M_z >_{max}$ to $< M_y >_{max}$ as a function of H_a to the

ratio of $J_{c\|}$ to $J_{c\perp}$. Comparing our results with his calculated curves for these quantities yields a ratio of $J_{c\|}$ to $J_{c\perp}$ for $YBa_2Cu_3O_{7-x}$ slightly larger than one. This is in agreement with the results obtained and presented in chapters 3 and 5. Both methods (rotating disk in a static magnetic field and rotating trapped flux in zero field followed by the application of an external field) can be exploited to determine the ratio of $J_{c\|}$ to $J_{c\perp}$ with satisfactory accuracy for various materials. One advantage of the first method employed in this thesis is the small number of measurements required to determine this ratio compared to the rotating disk technique.

To complement the observations presented in figures 6.2 and 6.3, the angle of rotation at which the maxima in the components of the magnetization curves occur are displayed in figures 6.4 and 6.5. It is evident that in both cases the required angle of rotation of the disk becomes less as the static applied fields are larger.

The shape of these curves and the evolution of the ratio θ_z/θ_y with H_a also yield information on the ratio $J_{c\|}/J_{c\perp}$. Sekerka has also calculated the dependence of these quantities on H_a for different $J_{c\|}/J_{c\perp}$. Although these data provide a less sensitive measure of $J_{c\|}/J_{c\perp}$ than the evolution of $< M_z >_{max} / < M_y >_{max}$, a comparison with the theoretical curves of Sekerka confirm that $J_{c\|}/J_{c\perp} \approx 1$ for the $YBa_2Cu_3O_{7-x}$ sample.

Further, the agreement between the calculations and observations indicates that $J_{c\|}$ and $J_{c\perp}$ exhibit the same dependence on B.

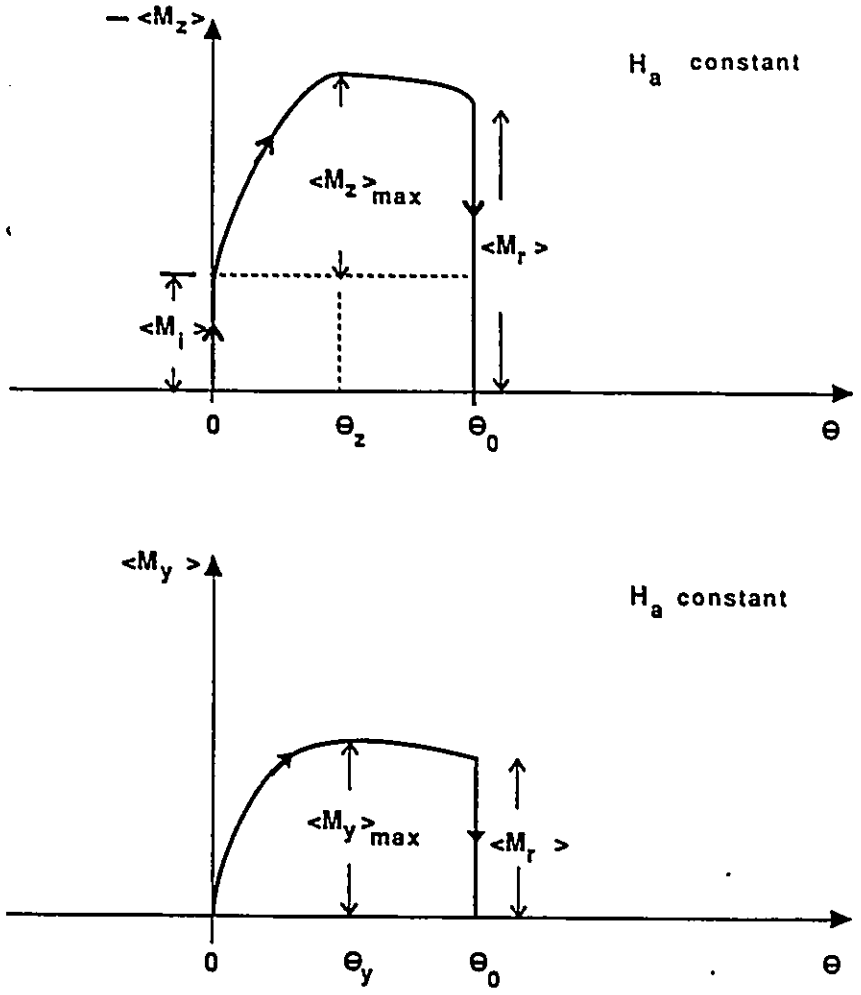

<Mi> : magnetization acquired by the disk during cooling process (Meissner effect).

<Mr> : resultant magnetization after disk is rotated through an angle Θ_0.

<My>max and <Mz>max : maximum in the components of the magnetization acquired by the specimen during rotation process.

Θ_y, Θ_z : angle of rotation corresponding to a maximum magnetization.

Figure 6.1: Sketches of the evolution of $< M_z >$ and $< M_y >$ as the disk is rotated through an arbitrary angle θ_o.

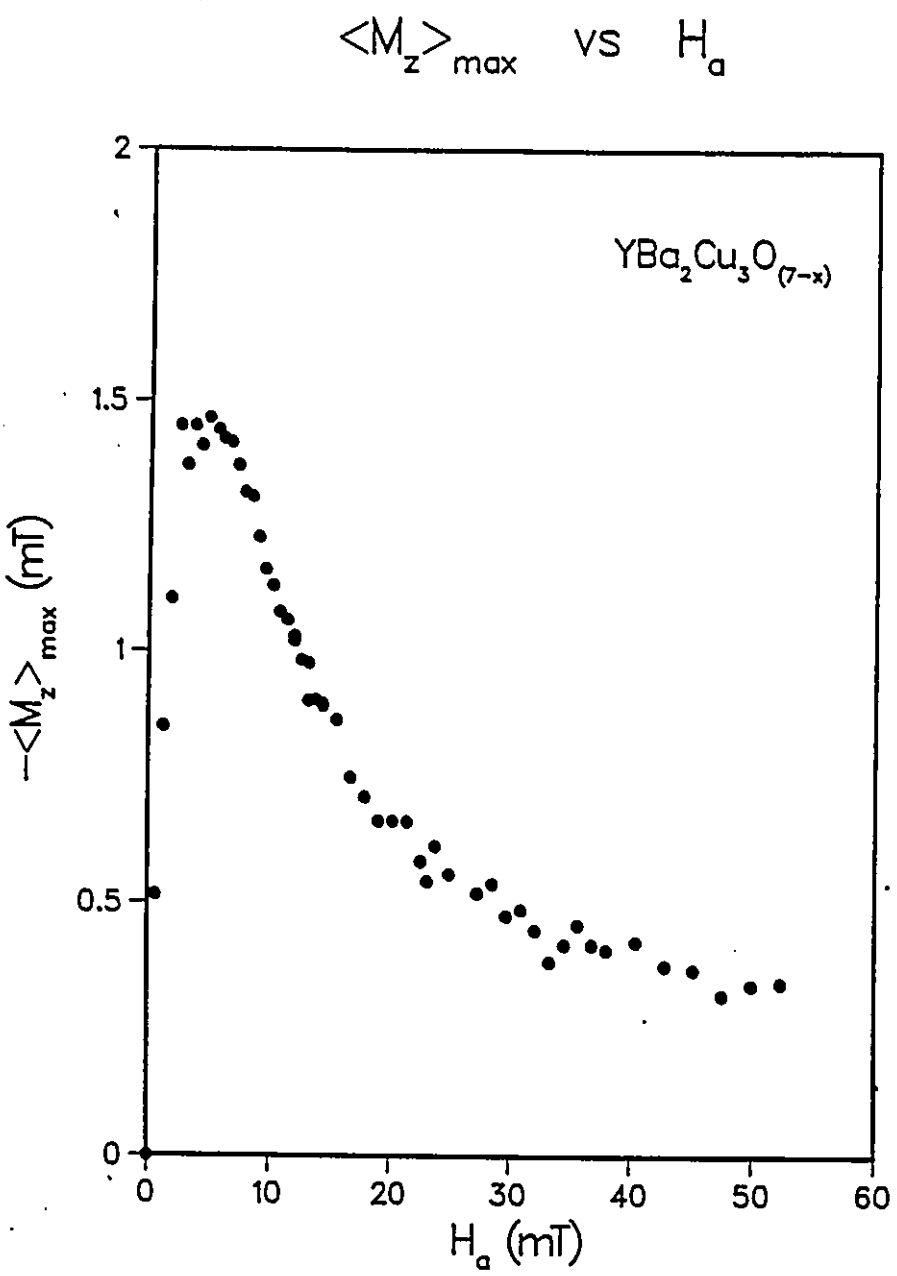

Figure 6.2: Maximum magnetization $\|$ to the applied field arising as the disk rotates in a static field H_a. The Meissner flux expulsion has been subtracted from the signal since it arises before rotation.

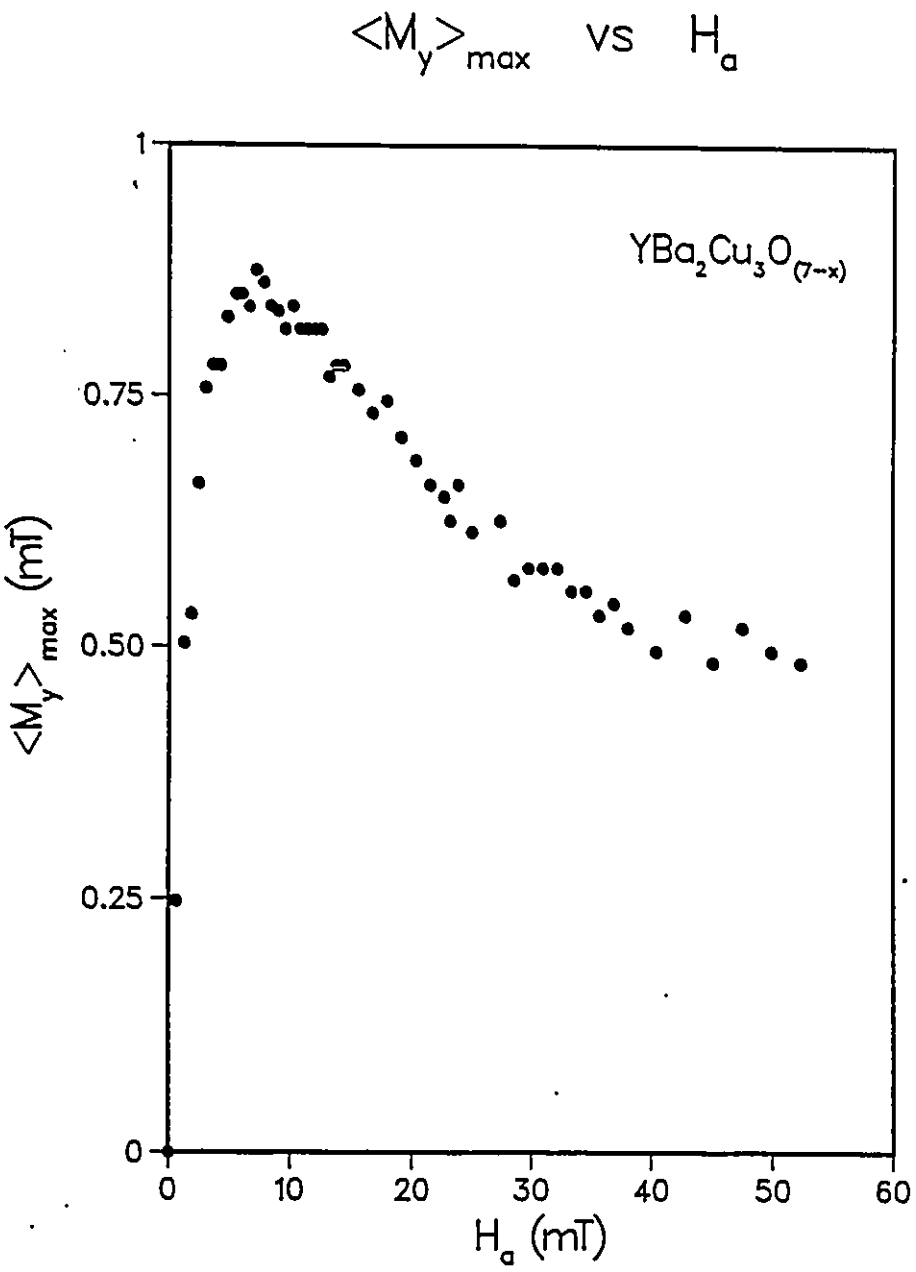

Figure 6.3: Maximum magnetization $\perp$ to the applied field acquired by the disk as it rotates in a static field H_a.

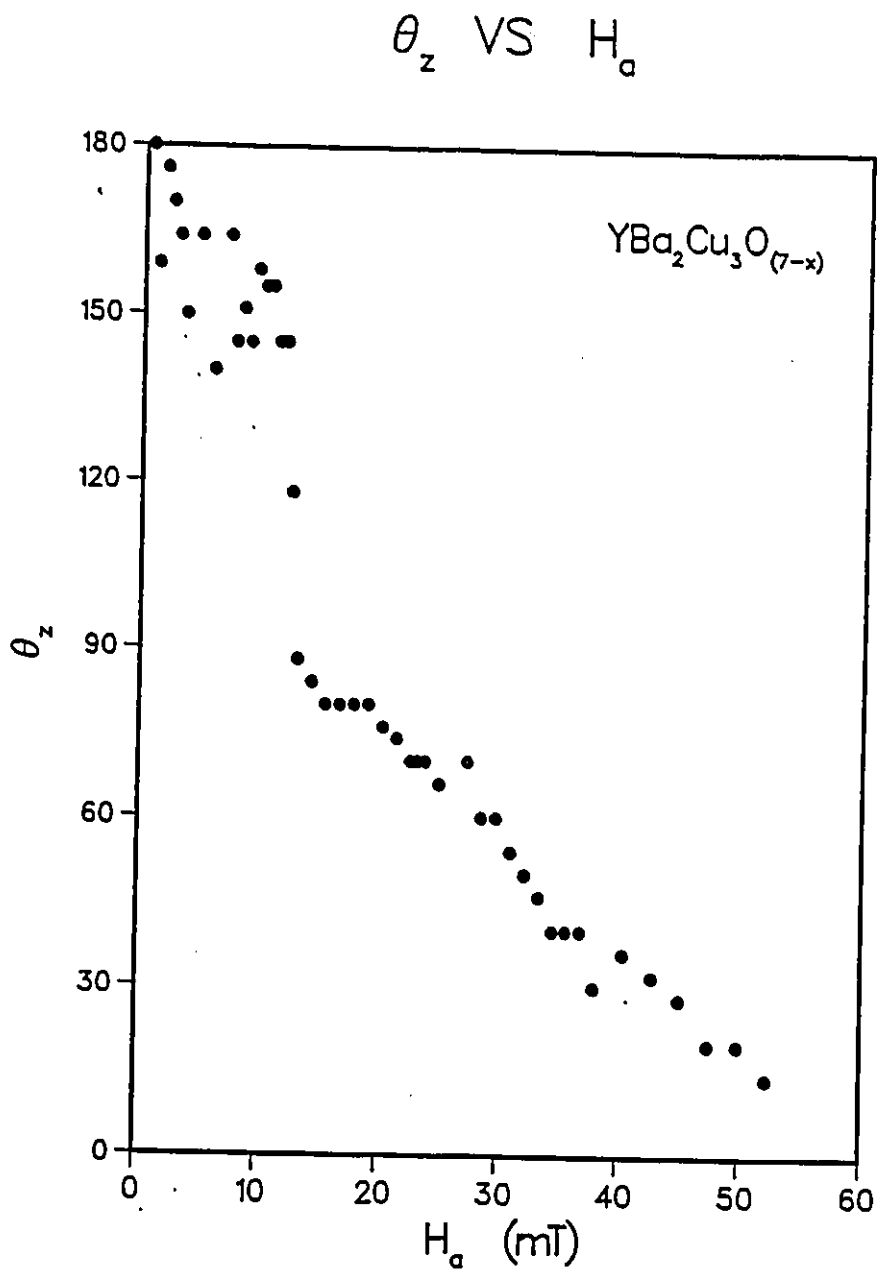

Figure 6.4: Angle of rotation at which the component of the magnetization $\parallel$ to H_a reaches its maximum value.

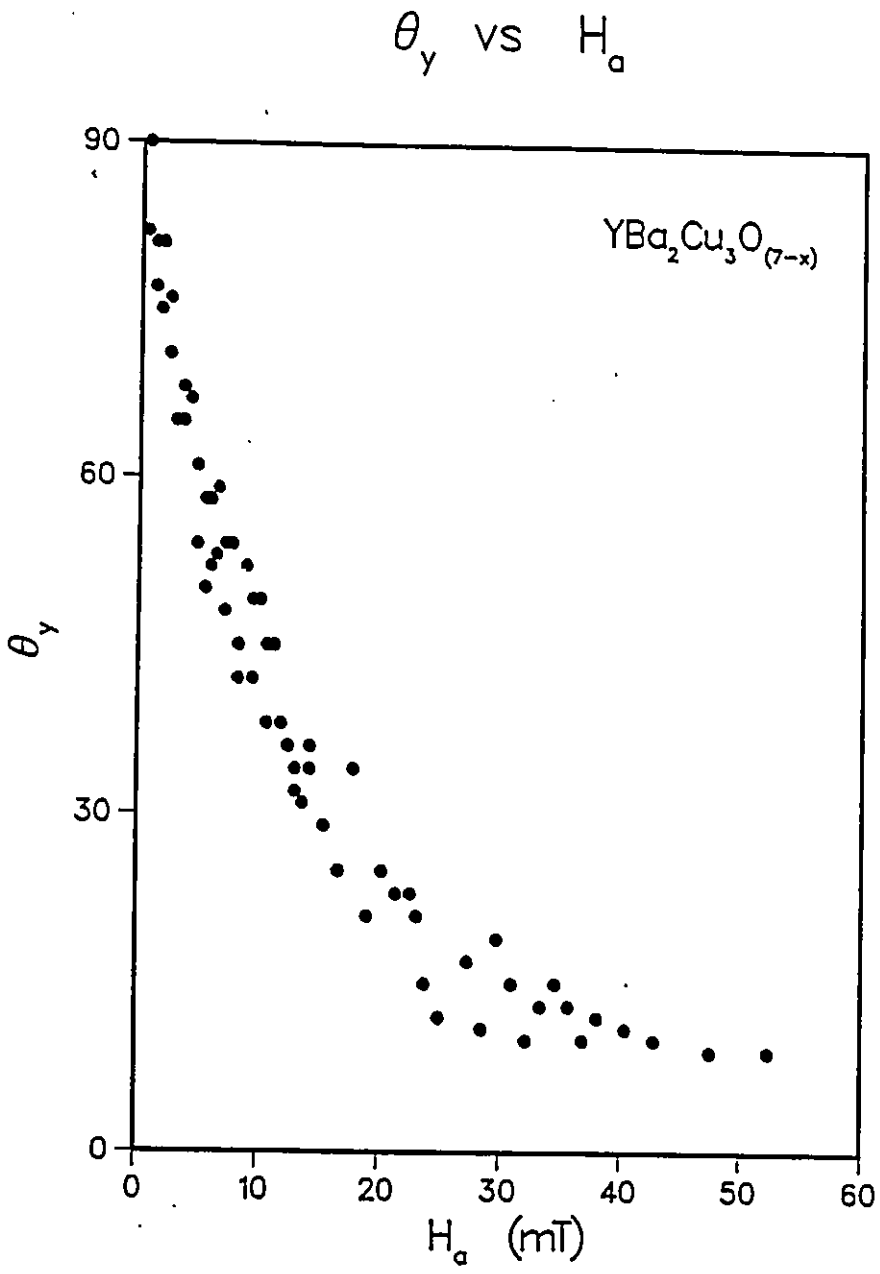

Figure 6.5: Angle of rotation at which the component of the magnetization $\perp$ to H_a reaches its maximum value.

Bibliography

[1] **A. A. Abrikosov.** Soviet Phys. J.E.T.P. 5:1174, (1957).

[2] **P. W. Anderson.** Phys. Rev. Lett., 9:309, (1962).

[3] **C. P. Bean.** Phys. Rev. Lett., 8:250, (1962).

[4] **C. P. Bean.** Rev. Mod. Phys., 36:31, (1964).

[5] **R. Boyer.** PhD thesis, Physics Department, University of Ottawa, (1977).

[6] **R. Boyer and M.A.R. LeBlanc.** Sol. State Comm., 24:261, (1977).

[7] **R. Boyer, G.Fillion, and M.A.R. LeBlanc.** J. Appl. Phys., 51:1692, (1980).

[8] **E. H. Brandt, J. R. Clem and D. J. Walmsley.** Jour. Low Temp. Phys., 37:43, (1979).

[9] **A. M. Campbell and J. E. Evetts.** Adv. Phys., 21:199, (1968).

[10] **J.R. Cave and M.A.R. LeBlanc.** J. Appl. Phys., 53:1631, (1982).

[11] **J. R. Clem and Antonio Perez-Gonzalez.** Phys. Rev., B(30):5041, (1984).

[12] **J. R. Clem and S. Yeh.** Jour. Low Temp. Phys., 39:173, (1980).

[13] **J. R. Clem.** Phys. Rev., **B(26)**:2463, (1982).

[14] **J. R. Clem.** Jour. Low Temp. Phys., **38**:353, (1980).

[15] **J. R. Clem and A. Perez-Gonzalez.** Proceedings of the International Symposium on Flux Pinning and Electromagnetic Properties of Superconductors, 196-200, (1985).

[16] **P. G. de Gennes.** Sol. St. Comm., **3**:127, (1965).

[17] **G. Fillion.** PhD thesis, Physics Department, University of Ottawa, (1986).

[18] **Y. B. Kim, C. F. Hempstead and A. R. Strnad.** Phys. Rev. Lett., 9:306, (1962).

[19] **Y. B. Kim, C. F. Hempstead and A. R. Strnad.** Phys. Rev., **129**:528, (1962).

[20] **Y. B. Kim, C. F. Hempstead and A. R. Strnad.** Phys. Rev., **131**:2486, (1963).

[21] **M. A. R. LeBlanc and C. T. M. Chang.** Sol. State Comm., 6:679, (1968).

[22] **J. P. Lorrain, M. A. R. LeBlanc and A. Lachaine.** Can. J. Phys., 57:1458, (1979).

[23] **K. A. Muller, M. Takashige and J. G. Bednorz.** Phys. Rev. Lett.58:1143, (1987).

[24] **A. Perez-Gonzalez and J. R. Clem.** Phys. Rev., **B(31)**:7048, (1985).

[25] **A. Perez-Gonzalez and J. R. Clem.** J. Appl. Phys., 58:4326, (1985).

[26] **J. Sekerka.** MSc thesis, Physics Department, University of Ottawa, (1989).

[27] **D. Shi, M. Xu, A. Umezawa and R. F. Fox.** Phys. Rev. B(42):2062, (1990).

[28] **Y. Yeshurun and A. P. Malozemoff.** Phys. Rev. Lett.60:2202, (1988).